Kinetic pathways of crystallization at the nanoscale

Zihao Ou [1,10], Ziwei Wang [2,10], Binbin Luo[1], Erik Luijten [3,4,5,6]* and Qian Chen [1,7,8,9]*

[1]Department of Materials Science and Engineering, University of Illinois, Urbana, IL, USA. [2]Graduate Program in Applied Physics, Northwestern University, Evanston, IL, USA. [3]Department of Materials Science and Engineering, Northwestern University, Evanston, IL, USA. [4]Department of Engineering Sciences and Applied Mathematics, Northwestern University, Evanston, IL, USA. [5]Department of Chemistry, Northwestern University, Evanston, IL, USA. [6]Department of Physics and Astronomy, Northwestern University, Evanston, IL, USA. [7]Department of Chemistry, University of Illinois, Urbana, IL, USA. [8]Materials Research Laboratory, University of Illinois, Urbana, IL, USA. [9]Beckman Institute for Advanced Science and Technology, University of Illinois, Urbana, IL, USA. [10]These authors contributed equally: Zihao Ou, Ziwei Wang. *e-mail: luijten@northwestern.edu; qchen20@illinois.edu

Supplementary Video 1. Synchronised Liquid-Phase TEM Video Showing the Lattice Vibration inside a Large-Scale Hexagonal Superlattice Formed by Triangular Nanoprisms.

On the left, the automatically tracked centre positions of the columns (green dots) are overlaid onto the original video and the Voronoi cell is constructed from the central positions. The Voronoi cell is coloured by its number of edges: white for six, blue for less than six, and red for more than six. The original liquid-phase video is captured at 1.3 fps and only one frame of each two successive frames is shown. The video is played at 6.5 fps, 10 times faster than real time. The electron dose rate was 8.9 e$^-$·Å^{-2}·s^{-1}. Scale bar: 200 nm.

Supplementary Video 2. Liquid-phase TEM Video of Individual Prisms Moving on the SiN$_x$ Substrate and the Stacking Process of a Pair of Prisms.

Two individual prisms are highlighted by the red and blue arrow before they stack together. The original liquid-phase TEM video is captured at 1.3 fps and every successive 5 frames are averaged to enhance the contrast of the nanoparticles. The video is played at 5.2 fps, 20 times faster than real time. The electron dose rate was 3.7 e$^-$·Å^{-2}·s^{-1}. Scale bar: 100 nm.

Supplementary Video 3. MC Simulation of Hexagonal Superlattice Formation from 1472 Triangular Prisms.

The simulation starts from an initial configuration of 64 columns ($M = 23$ prisms per column) organised on a 2D square lattice inside a rectangular simulation box with $L_z = 25t_0$ and reaches the equilibrium state where the columns are packed on a hexagonal lattice after $\sim10^7$ MC cycles. The 2D column packing fraction ϕ_{2D} is 0.386, and the ionic strength I is 0.5 M. The video (100 frames) is produced from 2×10^7 MC cycles (10^7 equilibration cycles followed by 10^7 production cycles). The prisms are coloured according to the squared modulus of the local bond orientational order parameter $\left|\psi_{6j}\right|^2$.

Supplementary Video 4. "On-and-off" Liquid-Phase TEM Video Showing the Disassembly and Reassembly of the Lattice when the Electron Beam is Turned off or on.

The imaging region is near the corner of the liquid cell holder, where the silicon part of the window can be seen as the black blocks at the upper left and lower left. The stationary boundary is highlighted by the red dotted line to show the same region was continuously monitored. The original liquid-phase video is captured at 1.3 fps and only one frame of each two successive frames is shown. The video is played at 6.5 fps, 10 times faster than real time. The electron dose rate was 7.0 e$^-$·Å^{-2}·s^{-1}. Scale bar: 200 nm.

Supplementary Video 5. Single-Column MC Simulation Showing the Fluctuation of Prism Orientations Inside a Column.

The column consists of $M = 23$ prisms with equal spacing confined by $L_z = 25t_0$, at an ionic strength $I = 0.5$ M. The video (101 frames) is produced from 1.01×10^7 MC cycles including 10^5

equilibration cycles (the system reaches equilibrium very quickly) followed by 10^7 production cycles, and a frame is obtained every 10^5 MC cycles.

Supplementary Video 6. Synchronised Liquid-Phase TEM Video Showing the Formation of a Large-Scale Superlattice.

On the left, the automatic tracked particles positions are overlaid onto the TEM image coloured following the same colour coding as used in Figure 2g–i (main text). On the right, we show the synchronised 2D structure-density histogram $(|\bar{\psi}_{6j}|^2, \rho_j)$ for all the columns inside one TEM image. The original liquid-phase video is captured at 1.3 fps and only one frame of every two successive frames is shown. The video is played at 6.5 fps, 10 times real time. The electron dose rate was 7.0 e$^-\cdot$Å$^{-2}\cdot$s^{-1}. Scale bar: 200 nm.

Supplementary Video 7. MC Simulation of the Formation of Side-by-Side Aggregates from 576 Triangular Prisms.

The simulation starts from an initial configuration of 64 columns ($M = 9$ prisms per column) organised on a 2D square lattice inside a rectangular simulation box with $L_z = 10t_0$. The system slowly evolves to the state with side-by-side aggregations being formed due to the strong side-by-side attraction between columns. The 2D packing fraction ϕ_{2D} is 0.386, and the ionic strength I is 3.0 M. The video (100 frames) is produced from 2×10^7 MC cycles, and a frame is obtained every 2×10^5 MC cycles.

Supplementary Video 8. Liquid-Phase TEM Video Showing the Crystallisation of Gold Concave Nanocubes into Simple Cubic Superlattices.

The liquid-phase TEM video is captured at 10 fps and only one of every 4 successive frames is used. The video is played at 5 fps, 2 times real time. The electron dose rate is 27.1 e$^-\cdot$Å$^{-2}\cdot$s^{-1}. Scale bar: 300 nm.

Supplementary Video 9. Liquid-phase TEM Video Showing the Crystallisation of Nanospheres into Face-Centred Cubic Superlattices.

The liquid-phase TEM video is captured at 8 fps and played at 8 fps in real time. The electron dose rate is 11.9 e$^-\cdot$Å$^{-2}\cdot$s^{-1}. Scale bar: 300 nm.

Supplementary Notes

Supplementary Note 1. Synthesis and preparation of gold nanoparticles for liquid-phase transmission electron microscopy (TEM) imaging

1.1. Synthesis of gold nanoparticles

1.1.1. Triangular nanoprism synthesis

The gold triangular nanoprisms used in our experiments are synthesised via a seeded growth method according to the literature[1-3]. First, a gold nanoparticle seed solution is prepared by rapidly mixing an aqueous solution of $HAuCl_4$ (250 µL, 10 mM), sodium citrate (500 µL, 10 mM) and ice cold $NaBH_4$ (300 µL, 10 mM) sequentially with 18.95 mL of water in a 50 mL Erlenmeyer flask and stirred at 1150 rpm for 1 min. The addition of the $NaBH_4$ solution should be quick to obtain small and monodisperse gold seeds. The seed solution is incubated at 40–45 °C for 15 min before use for the growth of gold triangular nanoprisms and then cooled down to room temperature. Note that the gold seed formation requires thoroughly washed glassware and stir bars to avoid the formation of large seeds as black sediments.

Gold triangular nanoprisms are then grown from the gold seeds (usually good within two hours after preparation). Aqueous solutions of $HAuCl_4$ (250 µL, 10 mM), NaOH (50 µL, 100 mM), ascorbic acid (50 µL, 100 mM) and the as-synthesised gold seed solution (22 µL) are sequentially added into 9 mL of 50 mM CTAB solution containing 50 µM of NaI in a 20 mL scintillation vial. The solution is hand-shaken for 1 s after each addition and the mixture is left undisturbed for 30 min. The colour of the solution gradually changes from clear to purple, indicating the formation of triangular nanoprisms along with spherical impurities. Purification of the product solution to get rid of the spherical particle impurities is performed according to the literature[2-5]. The purple solution is transferred to a 15 mL centrifuge tube and 0.9 mL of 2 M NaCl is added. After the solution is mixed well, it is left undisturbed for 2 h to induce face-to-face stacking of triangular nanoprisms due to screening of electrostatic repulsion. This solution is centrifuged twice (1st round: 4900 rpm for 30 s; 2nd round: 1350 rpm for 5 s). Immediately after each centrifugation, the supernatant containing unassembled spherical impurities is removed as much as possible using a micropipette, because even a tiny amount of supernatant would increase the amount of spherical impurities in the final product solution. After the 2nd round of centrifugation, several drops of water are first added to the sediments to redisperse the product in solution and 9 mL of 50 mM CTAB is added to keep the prisms stable. Successful purification yields gold triangular nanoprisms with minimal spherical impurities (Supplementary Figure 1).

1.1.2. Concave nanocube synthesis

The gold concave nanocubes are synthesised following a modified universal seeded growth[6]. This synthesis includes (i) preparation of gold nanorods, (ii) etching the nanorods into spherical seeds and (iii) growth of spherical seeds into concave nanocubes.

The gold nanorods are synthesised following literature procedures[6,7]. First, a gold nanorod seed solution is prepared by rapidly mixing an aqueous solution of $HAuCl_4$ (125 μL, 10 mM), CTAB (5 mL, 100 mM) and ice-cold $NaBH_4$ (300 μL, 10 mM) sequentially in a 20 mL vial and stirred at 1150 rpm for 1 min. The nanorod seed solution is incubated at 30 °C for 30 min before use. Next, to grow gold nanorods from seeds, aqueous solutions of $HAuCl_4$ (10 mM, 20 mL), $AgNO_3$ (10 mM, 3.6 mL), L-ascorbic acid (100 mM, 2.28 mL) and 480 μL seed are added in sequence to 400 mL CTAB solution (100 mM in water) in a 1 L Erlenmeyer flask at 30 °C. This growth solution is left undisturbed for 2 h at 30 °C, and then centrifuged twice (8000 rpm for 15 min each round). The resultant sediment is redispersed using 50 mM CTAB and a UV-Vis extinction spectrum is collected using a Scinco S-4100 PDA spectrophotometer. The desired gold nanorod dimension and concentration (tuned by the CTAB solution volume) are evaluated based on the presence of a surface plasmon resonance band at 704 nm with an extinction of 2.

Next, spherical seeds are obtained by etching of the gold nanorods following reductive growth and oxidative etching. Aqueous $HAuCl_4$ solution (10 mM, 928 μL) is added to 103.1 mL gold nanorod solution in a 250 mL Erlenmeyer flask and stirred at 200 rpm at 40 °C for 4 h to induce the etching. The solution is then centrifuged twice (1st round: 11000 rpm for 45 min; 2nd round: 11000 rpm for 30 min). The sediment is redispersed using 100 mM CPC to achieve the desired seed concentration with an extinction of 1 at 524 nm in the UV-Vis extinction spectrum. To improve monodispersity of the spherical seeds, aqueous solutions of CPC (10 mM, 56.67 mL), $HAuCl_4$ (10 mM, 992 μL), L-ascorbic acid (100 mM, 12.75 mL) and 17 mL spherical seed solution are added in sequence to a 125 mL Erlenmeyer flask under 300 rpm stirring at 40 °C. This reductive growth reaction is continued for 15 min without stirring and then the solution is centrifuged twice (10000 rpm for 10 min each). The sediment of reductive grown nanoparticles is redispersed using 50 mM CTAB to achieve the desired concentration with an extinction of 1 at 539 nm in the UV-Vis extinction spectrum. The next round of oxidative etching to spherical seeds is done by adding aqueous $HAuCl_4$ solution (10 mM, 426 μL) to 71.04 mL of the grown nanoparticle solution in a 125 mL Erlenmeyer flask and is stirred at 200 rpm at 40 °C for 4 h. The improved spherical seeds are obtained by centrifuging the reaction solution twice (11000 rpm for 30 min each) and dispersing the sediment in 100 mM CPC to achieve the desired spherical seed concentration with an extinction of 1 at 524 nm in the UV-Vis extinction spectrum.

Finally, concave gold nanocubes are grown from the spherical seeds prepared above[6]. Aqueous solutions of CPC (100 mM, 5 mL), HCl (1 M, 250 μL), $HAuCl_4$ (10 mM, 250 μL), $AgNO_3$ (10 mM, 62.5 μL), L-ascorbic acid (100 mM, 47.5 μL) and 620 μL of the spherical seed solution are added in sequence to a 20 mL vial at room temperature. The reaction is left undisturbed for 2 hours and then the solution is centrifuged twice (3000 rpm for 5 min each). The gold concave nanocubes are obtained by redispersing the sediment in 50 mM CTAB with an extinction of ~0.8 at 637 nm in the UV-Vis extinction spectrum. TEM imaging shows high monodispersity (Supplementary Figure 2a).

1.1.3. Nanosphere synthesis

The gold nanosphere synthesis follows the same universal seed method as described in Supplementary Note 1.1.2. The improved spherical seeds described in Supplementary Note 1.1.2 undergo one more reductive growth and oxidative etching cycle to achieve even higher monodispersity. After this step, the seed solution obtained is diluted using 100 mM CPC to achieve the desired concentration with an extinction of 1 at 524 nm in the UV-Vis spectrum. In the next growth and etching round, aqueous solutions of CPC (10 mM, 80 mL), $HAuCl_4$ (10 mM, 1.4 mL), L-ascorbic acid (100 mM, 18 mL) and 4.3 mL of this diluted seed solution are added in sequence to a 125 mL Erlenmeyer flask under 300 rpm stirring at 40 °C. The growth is continued for 15 min without stirring and then the solution is centrifuged twice (4500 rpm for 10 min each). The sediment is redispersed using 50 mM CTAB to achieve the desired concentration of with an extinction of 2 at 574 nm in the UV-Vis spectrum. Next, 46.29 mL of this solution is mixed with $HAuCl_4$ (10 mM, 138.86 µL) in a 125 mL Erlenmeyer flask and stirred at 200 rpm at 40 °C for 4 h. The nanospheres used for liquid-phase TEM are obtained by centrifuging the solution twice (4500 rpm for 8 min each) and redispersing the sediment in 100 mM CPC. The solution has a final nanosphere concentration with an extinction of ~1 at 541 nm in UV-Vis extinction spectrum. TEM imaging shows high uniformity (Supplementary Figure 2b).

1.2. Thiol modification and sample solution preparation for liquid-phase TEM imaging

The gold nanoparticles synthesised (gold nanoprisms, concave cubes and spheres) undergo ligand exchange with carboxylate-terminated thiols ($HS(CH_2)_{11}(OC_2H_4)_6OCH_2COOH$) following a literature method[1,8]. The thiol ligands stabilise the nanoparticle suspension in the absence of free ligands in solution. In addition, the ligand exchange helps achieve good resolution for the liquid-phase TEM imaging, whereas stabilisation of the nanoparticles via highly concentrated free CTAB ligands could lower the contrast when imaging nanoparticles in liquid[9].

Specifically, for the nanoprisms, the purified solution in 50 mM CTAB is centrifuged twice to decrease the concentration of free CTAB molecules (1st round: 8800 rpm for 8 min; 2nd round: 6600 rpm for 8 min). After the 1st round of centrifugation, supernatant is removed and the remaining liquid with sediments (~50 µL) is mixed with 8.95 mL of water. After the 2nd round of centrifugation, supernatant is removed and remaining liquid with sediments (~50 µL) is mixed with 3.00 mL of water. An aqueous solution of thiol molecules (44.26 µL, 7.93 mM) is added to the prism solution and incubated for 30 min. After that, the solution is sonicated for 5 s and 0.538 mL of 1 M pH = 8 phosphate buffer solution (PBS, composed of 0.07 M sodium phosphate monobasic monohydrate and 0.93 M sodium phosphate dibasic anhydrous) is gently added to the solution and left undisturbed overnight. The final solution contains 100 µM of thiol molecules and 0.15 M of pH = 8 PBS, where the PBS solution is present to screen the electrostatic repulsion of deprotonated thiol ligands and to facilitate efficient coating of the gold prism surface. During ~15 h of incubation, the prisms not only are fully covered by thiols but also begin to assemble face-to-face stacked and form into black sediments. Just prior to use for liquid-phase TEM, we dilute this solution to a PBS concentration of 0.0345 M, so that the prisms remain individual prisms.

For the gold concave nanocubes, 7.5 mL concave nanocube solution obtained in Supplementary Note 1.1.2 is centrifuged twice at 3000 rpm for 8 min each time. The sediment is redispersed in 3 mL water, added with 44.26 μL of 7.93 mM aqueous thiol solution and incubated for 30 min to start the ligand exchange. Next the solution is sonicated for 5 s, added with 0.344 mL 1 M PBS and left undisturbed overnight to complete the ligand exchange. In this process, the concave nanocubes concentrate to sediments at the bottom. The sediment is then diluted by water as the stock solution for liquid-phase TEM imaging (24 μL of the sediment diluted in 200 μL water).

For the gold nanospheres, a 7.5 mL nanosphere solution is centrifuged twice at 4400 rpm for 8 min each time. The sediment is redispersed in 3 mL water, 44.26 μL of 7.93 mM aqueous thiol solution is added and the sample is incubated for 30 min to start the ligand exchange. Next, the solution is sonicated for 5 s, 0.344 mL 1 M PBS is added and the sample is left undisturbed overnight to complete the ligand exchange. In this process, the nanospheres sediment to the bottom. The sediment is then diluted by water as the stock solution for liquid-phase TEM imaging (28 μL of the sediment diluted in 400 μL water).

1.3. Nanoparticle characterisation

A JEOL 2100 Cryo TEM with a LaB_6 emitter at 200 kV is used to characterise the morphology of the purified gold nanoprisms, concave nanocubes and nanospheres obtained in Supplementary Note 1.1. Using the prism system as an example, an aliquot of the prism solution (1 mL) is centrifuged at 7600 rpm twice for 2 min. A drop of the concentrated solution (10 μL) is placed on a TEM grid and dried before imaging. Supplementary Figure 1a shows a typical TEM image of the nanoprisms and their size distribution. The prism side length is found to be (100.5 ± 9.5) nm, based on the measurements of 118 triangular prisms. Similarly, from TEM images (Supplementary Figure 2), the gold concave nanocubes are measured to be 62.0 ± 4.6 nm in edge length and the gold nanospheres are 76.0 ± 2.2 nm in diameter.

Supplementary Note 2. Liquid-phase TEM imaging

For the gold triangular nanoprisms, the liquid-phase TEM imaging is carried out on a JEOL 2100 Cryo TEM with a LaB_6 emitter at 200 kV using the Protochips Poseidon 210 liquid flow holder. The TEM movies are captured by a Gatan Ultrascan charge-coupled device (CCD) camera with a 0.1 s exposure time per frame at a rate of 1.3 frames per seconds (fps). In a typical experiment, an aliquot of prepared nanoprism solution (see Supplementary Note 1.2, in 0.0345 M pH = 8 PBS) is micropipetted onto a SiN_x chip pretreated with oxygen plasma (window: 550 μm × 20 μm, 150 nm spacer flow echip, Protochips), which is then assembled with another SiN_x chip (window: 550 μm × 20 μm) in a Protochips Poseidon 210 liquid flow TEM holder. The SiN_x chips are pretreated at a medium RF level for 45 s using a Harrick PDC-23G basic plasma cleaner to render them clean and hydrophilic. We only use the quiescent state of the holder, not the flow state. For most of the imaging, we look at the corner of the window area, where we expect the smallest SiN_x membrane bowing induced by the high vacuum inside the TEM[10].

During the liquid-phase TEM imaging of a nanoprism sample, the electron dose rates are kept ultra-low (3.7–8.9 $e^-\cdot\text{Å}^{-2}\cdot s^{-1}$), which we verified in our previous work to be low enough to avoid beam-induced ligand stripping or reactions of the nanoparticles (more details in Supplementary Note 5)[1,4]. At this range, we expect the electron beam to increase the ionic strength of the solution through radiolysis reactions. In contrast, a dose rate of 14.8 $e^-\cdot\text{Å}^{-2}\cdot s^{-1}$ or higher is shown to induce a too high ionic strength and drive the formation of kinetically trapped disordered aggregates, as shown in a typical TEM image (Supplementary Figure 4a). Specifically, the dose rates are controlled by electron beam size, magnification and spot size (3 on JEOL 2100 Cryo TEM). Dose rates are calculated using the total pixel intensity of an acquired TEM image at the same beam conditions as those in liquid-phase TEM imaging, but without samples via: Dose rate ($e^-\cdot\text{Å}^{-2}\cdot s^{-1}$) = Total pixel intensity/(Acquired area × Exposure time × conversion factor). Each electron hitting the detector gives rise to a pixel intensity of 3.472, based on our Faraday cup calibration of the TEM at beam dose rates below 20 $e^-\cdot\text{Å}^{-2}\cdot s^{-1}$, matching the dose rate range of our experiments.

For the gold concave cubes and nanospheres, liquid-phase TEM imaging is performed on a Hitachi 9500 TEM with a LaB_6 emitter at 200 kV and a liquid flow TEM holder (Hummingbird Scientific, model number: 1400-057). The liquid-phase TEM movies are captured by a Gatan Orius fiber-optically coupled CCD camera with an exposure time of 0.1 s at a rate of 10 or 8 fps. In a typical experiment of concave nanocubes, 5 μL concave cube solution prepared as described in Supplementary Note 1.2 is mixed with 1.36 μL of PBS (0.15 M) to achieve a final PBS concentration of 0.04 M. Then 0.1 μL of this solution is placed on the bottom chip (window: 50 μm × 200 μm × 50 nm, 250 nm spacer, Hummingbird Scientific) and assembled with another top chip (window: 30 μm × 650 μm × 50 nm, Hummingbird Scientific), both pretreated by oxygen plasma. After the chip assembly, we flow the same concentration of PBS (0.04 M) through the liquid flow holder for 2 hours at 5 μL/min to ensure that the whole liquid chamber reaches this PBS concentration, followed by flowing water at 5 μL/min for 10 to 35 min until dispersed concave nanocubes are observed. The crystallisation of dispersed concave nanocubes into simple cubic superlattices is triggered by flowing 0.04 M PBS solution at 5 μL/min for ~10 min and imaged at the quiescent stage at a dose rate of 27.1 $e^-\cdot\text{Å}^{-2}\cdot s^{-1}$. In a typical experiment on nanospheres, 1.8 μL nanosphere solution prepared in Supplementary Note 1.2 is mixed with 0.19 μL of PBS (1 M) to achieve a PBS concentration of 0.1 M. Then 0.1 μL of this solution is placed on the bottom chip and assembled with another top chip (the same chips as used for the concave cubes). After the chip assembly, we flow the same concentration of PBS (0.1 M) through the liquid flow holder for 2 hours at 5 μL/min to ensure that the entire liquid chamber reaches this PBS concentration. Next, we flow water into the system at 5 μL/min for about 15 min and image the system at the quiescent stage for a dose rate of 11.9 $e^-\cdot\text{Å}^{-2}\cdot s^{-1}$. During this process, the effective ionic strength increase induced by the beam triggers the dispersed nanosphere crystallisation into closely packed superlattices. Note that the dose rates for both systems are still within the regime that does not involve complications due to ligand stripping or nanoparticle reaction.

Supplementary Note 3. TEM image processing procedure to identify the projected contour of stacked prisms

The original TEM movies are saved in .dm3 format (the format in Digital Micrograph, the movie capturing software of our TEM camera). The open-source software ImageJ is used to open the .dm3 files[55]. For this contour analysis, we first used the built-in "Enhance Contrast" tool in ImageJ (0.3%, normalised) to enhance the movie contrast. The processed movie is then converted to image series in .tif format for further analysis using our customised Matlab image processing codes. Specifically, for prisms with added projected contours (main text Figure 1e,g), we follow the processing method shown below. For two prisms stacked in a misaligned manner, the image contrast is further enhanced by averaging over neighbouring frames in the same movie (Supplementary Figure 5a). To do that, the central positions of the two stacked prisms are first measured using a circumscribed circle to fit the three tips of the darker prism; the orientations of the same prism are measured from the direction of one edge during movement. We repeat the same procedure for 22 frames of a span of 47 frames in a continuous TEM movie (Supplementary Video 2). We show 5 typical frames in Supplementary Figure 5a. Second, these images are repositioned by setting the measured centre of the prism as the centre of the image and rotated to keep the sides of the prism aligned in all frames. Finally, the images after repositioning and rotation are averaged to enhance contrast and decrease noise (see final image III, Supplementary Figure 5a). The image of the short column (main text Figure 1f) is averaged over 5 selected frames in a different TEM movie, with alignment and rotation of the images according to the position and orientation of the columns. These final averaged images are used as the inputs for contour finding and labelling.

The contour-finding and labelling process is shown in Supplementary Figure 5b,c, and the parameters for contour finding are listed in Supplementary Table 3. The image of two stacked prisms is enlarged in Supplementary Figure 5b to show their shape more clearly. The image background is first calculated using the Matlab built-in function imopen.m, using disks with sizes listed in Supplementary Table 3. This background is then subtracted from the input image. A 2D Fourier transformation of the image is calculated using the Matlab built-in functions fft2.m and fftshift.m. A circular low-pass filter is then applied to the Fourier transform by only keeping the information below the spatial threshold frequency listed in Supplementary Table 3. After filtering, the image is binarised using a single-intensity threshold. In the binarised image, the intensity values are reversed to render the originally dark prisms white, to facilitate contour finding. The Matlab built-in function imfill.m is then applied to fill in holes in the white regions of the binarised image. The projection contour of the prisms is calculated from the binarised images based on the strong intensity change at shape contours using the built-in Matlab function bwtraceboundary.m. Contour smoothing is achieved by averaging neighbouring points on the rough contour. A smoothing factor, which is the number of neighbouring points used in averaging, is used to control the level of smoothing. The smoothed contour is used as the final output contour shown in Figure 1e (main text). The same process is applied for the contour finding and labelling in Figure 1g (main text) as shown in Supplementary Figure 5c.

Supplementary Note 4. Literature summary of the sluggish nanoparticle motions in previous liquid-phase TEM work

Maintaining the fast motion of nanoparticles under the liquid-phase TEM is a key experimental advancement which enables the crystallisation of individual nanoparticles into superlattices instead of the irregular aggregates observed previously. In our work, the nanoparticles can dynamically arrange and rearrange their positions during crystallisation. Such fast motions are crucial to annealing defects and the formation of a crystal (main text Figure 1h), avoiding kinetic trapping into irregular aggregates. We track the trajectories of 18 liquid-like columns (Supplementary Figure 3a) and compute the diffusivity (247 nm^2/s) based on the mean squared displacement (MSD) versus time (Supplementary Figure 3b). Because of the high area fraction (~0.8) of the liquid-like columns, their diffusivity is lowered to less than 10% of that of a free column in solution[11,12]. Therefore, the diffusivity of a single column is estimated to be about 2470 nm^2/s, two orders of magnitude smaller than the predicted diffusivity based on Brownian motion. In contrast, in previous liquid-phase TEM work (Supplementary Table 1), nanoparticle motions have been found to be 5 to 9 orders of magnitude slower than the predicted diffusivity over a wide range of nanoparticle composition and size. In Supplementary Table 1 we survey earlier liquid-phase TEM (not scanning transmission electron microscopy (STEM)) work in which nanoparticle diffusivity is measured experimentally.

Supplementary Note 5. Evaluation of beam-induced effects on the nanoparticle system

Here, we evaluate in detail electron-beam effects on the crystallisation behaviour of nanoparticles in the systems studied.

5.1. Evaluation of beam-induced pH effects on the surface charge density of nanoprisms

The surface charge density of the prisms arises from deprotonated –COO$^-$ ligands on the prism surface (main text Figure 1a). The ratio of negatively charged (–COO$^-$) and neutral (–COOH) ligands on the prisms is calculated for different pH conditions using the Henderson–Hasselbalch equation, $pH = pK_a + \log\left(\frac{[A^-]}{[HA]}\right)$, where $[A^-]$ and $[HA]$ are the molar concentrations of –COO$^-$ and –COOH ligands on the prism surface at equilibrium, respectively. The –COOH ligand has an acid dissociation constant (pK_a) around 3.5–3.7, as specified by the manufacturer, and we use 3.5 in the calculation. At the initial pH = 8, we perform zeta-potential measurements of the nanoprisms using a Malvern Zetasizer and obtain a surface charge density $\sigma = -0.048$ C/m^2, calculated from the measured prism mobility μ following $\sigma = \mu\nu\kappa$, where ν is the dynamic viscosity of the solution and κ^{-1} the electrostatic screening length of the solution[1,22]. As shown in Supplementary Figure 4b, the prism surface charge density stays constant when the pH is larger than 5 (97–100% of the –COOH functional groups are deprotonated). Note that the initial PBS solution (0.0345 M, pH = 8) has a buffering capability that can keep the final pH above 5 for up to 0.0325 M of additional H$^+$ possibly generated during the TEM imaging (Supplementary Figure 4c). There is a monotonic relationship between H$^+$ generated in liquid-phase TEM via

radiolysis of water and electron-beam dose rates[23]. Even at a dose rate of $\sim 10^9$ Gy/s $= 224$ e$^-\cdot$Å$^{-2}\cdot$s^{-1}, higher than the dose rates we used, the H$^+$ generated by radiolysis is still three orders of magnitude lower than 0.0325 M[23]. Therefore, we expect the carboxylic acid functional group of ligands on the prism surface to remain completely deprotonated and the prism surface charge density to remain constant during liquid-phase TEM imaging, consistent with our previous work[1,4].

5.2. Beam-induced ionic strength increase at low dose rates

Under electron beam irradiation, radiolysis of pure water gives rise to radiolysis products, including charged species (e.g., e$^-$, H$^+$, OH$^-$, HO$_2^-$, O$^-$, O$_2^-$, and O$_3^-$)[23], which increase the ionic strength. In our previous work[1], we showed using the calibration between liquid-phase TEM and small-angle X-ray scattering that at low dose rates the effective ionic strength increases monotonically with beam dose rate, for PBS buffer solution of the same composition. We use those results as a working curve and derive the final ionic strength to be about 0.45–0.75 M at our imaging conditions. These final ionic strengths are consistent with the parameters used in our simulation, which reproduce our experimental results (see main text and Supplementary Note 11). This agreement shows that the illumination beam, at low dose rate conditions, does not alter the fundamental nature of nanoparticle interactions. For example, ligands are shown to stay intact on the prism surfaces because the gap of two ligand layer thickness is still maintained between adjacent prisms even when the net attraction pushes them into physical contact, as shown in our previous work on nanoparticle self-assembly studies at low dose rates[1,4]. Note that when the dose rates are higher than 300 e$^-\cdot$Å$^{-2}\cdot$s^{-1}, the prisms are observed to coalesce[1] and alter their shape fundamentally, possibly due to desorption of passivating ligands.

5.3. Literature survey on beam dose rate dependent electron-beam effects in liquid-phase TEM

Here, we survey and compile previously observed radiation effects in liquid-phase TEM work at different dose rates and show that the beam effects in our work detailed in Supplementary Notes 5.1 and 5.2 are consistent with these observations (Supplementary Table 2, updated from Table S1 of Ref. 1). The literature survey is summarised in Supplementary Figure 4d in the form of a scatter plot that illustrates the appearance of three distinct dose rate regimes. We focus on studies performed in a SiN$_x$-based liquid-phase TEM and do not consider STEM or graphene-based liquid cell TEM studies because of possible differences in beam radiation and energy dissipation[16,24-26]. Studies that did not report dose rate values are not included. The precise boundary of the low-dose regime can shift given different solvents, ligands and nanoparticles, although the general trend of electron-beam effects that increase with dose rate is consistent with what has been shown below in our literature survey.

In the first regime (green area, Supplementary Figure 4d, $< \sim 1$ e$^-\cdot$Å$^{-2}\cdot$s^{-1}), Kelly et al.[27,28] and Evans et al.[29] primarily performed biological imaging with minimal beam effects. This is also the regime where we did not detect a change in the nanoprism system (the leftmost data point in Figure 5 of Ref. 1). The second regime (red area, Supplementary Figure 4d, 1–90 e$^-\cdot$Å$^{-2}\cdot$s^{-1})

matches with our discussion that visible nanoparticle reactions do not occur (with one exception discussed below) but the liquid environment affects nanoparticle interactions. Within this regime, Keskin et al.[30] reported beam-induced electrostatic screening that allows nanoparticles to approach each other closely and assemble due to DNA base pairing. In electrochemistry studies, a simple redox event at a Pt electrode was examined at a dose rate of ~1 $e^-\cdot\text{Å}^{-2}\cdot s^{-1}$ in a SiN_x cell patterned with electrodes[31]. Although there was no visible change of the electrode, a shift in the redox potentials occurred in the presence of the electron beam. There are two references[32,33] where nanoparticle growth was observed at 42 $e^-\cdot\text{Å}^{-2}\cdot s^{-1}$ and 46 $e^-\cdot\text{Å}^{-2}\cdot s^{-1}$. Yet even in the first work, no nanoparticle reaction was observed at dose rates below 30 $e^-\cdot\text{Å}^{-2}\cdot s^{-1}$, which is the range of electron beam dose rates used in our experiments (prisms: 3.7–14.8 $e^-\cdot\text{Å}^{-2}\cdot s^{-1}$; concave cubes: 27.1 $e^-\cdot\text{Å}^{-2}\cdot s^{-1}$; spheres: 11.9 $e^-\cdot\text{Å}^{-2}\cdot s^{-1}$). The third regime (yellow area, Supplementary Figure 4d, > 100 $e^-\cdot\text{Å}^{-2}\cdot s^{-1}$) is the dose rate used in most previous liquid phase TEM work, where chemical reactions triggered by the electron beam have been consistently observed. In this regime, the accumulated radiolysis products change the redox environment of the liquid and induce the growth, coalescence and sometimes etching (depending on solution composition) of nanoparticles in the presence of metallic precursors. Notably, at dose rates higher than 1000 $e^-\cdot\text{Å}^{-2}\cdot s^{-1}$, where we observed fusing of prisms due to the possible beam-induced removal of surface ligands (Figure 5 of Ref. 1 at 3400 $e^-\cdot\text{Å}^{-2}\cdot s^{-1}$), previous experiments also showed abrupt changes of the structure and dynamics of nanoparticles. For example, Wu et al.[34] reported the deposition of gold onto Pt seed nanoparticles at 300 $e^-\cdot\text{Å}^{-2}\cdot s^{-1}$ and fractal growth of gold dendrites at 1500 $e^-\cdot\text{Å}^{-2}\cdot s^{-1}$. Tang et al.[35] reported the electron-beam-induced growth of Au nanocrystals as well as coalescence at 1675–1836 $e^-\cdot\text{Å}^{-2}\cdot s^{-1}$. Wu et al.[36] reported the growth of Au nanocrystals and formation of multi-twinned decahedral nanostructures at 6250 $e^-\cdot\text{Å}^{-2}\cdot s^{-1}$. It is speculated in these studies[34-36] that electron-beam effects can go beyond changing the liquid redox environment and also have the potential to induce surface ligand damage or even rearrange the atoms inside nanoparticles.

In all liquid-phase TEM work listed in Supplementary Table 2, electron-beam-induced plasmonic force were not observed, not even in several direct quantitative force mapping experiments[9,18,37]. Although plasmonic forces have been shown to displace metallic nanoparticles in previous STEM work[38-40], this effect was reportedly observed as not playing a role in TEM systems even when- an electron dose rate of ~1000 $e^-\cdot\text{Å}^{-2}\cdot s^{-1}$, two orders of magnitude higher than our experimental conditions, was used[41]. This is ascribed due the fact that in TEM the electron beam uniformly illuminates a large sample area instead of the focused beam used in STEM, and that generally smaller dose rates are used than in STEM work where plasmonic force effects were observed[18,41,42]. In addition, even in STEM it has been reported, based upon comparison of experimental observations before and after the liquid inside a liquid cell was dried, that plasmonic force effects are only important when particles reside in vacuum and not when they reside in a liquid[43].

Supplementary Note 6. TEM movie analysis to identify the nonclassical crystallisation pathways

6.1. Vertical growth of columns

The vertical growth of columns is observed and captured at two levels. As shown in Figure 1d–g (main text), we capture and analyse the step-wise stacking and rounding of the projection contour on the single-column level. In addition, we capture the large-scale stacking process from prisms sitting on the SiN_x substrate to fully grown columns (Supplementary Figure 6). Over time, the projections of prisms continue to decrease in intensity, an indication of more prisms stacking onto the bottom ones. According to the Beer's absorption law often used for TEM image-contrast analysis[56,57], the contrast is given by

$$C_{\text{TEM}} = \ln\left(\frac{I_{\text{water}}}{I_{\text{NP}}}\right) = n_{\text{atom}}\sigma_{\text{cross}}t , \tag{S1}$$

where C_{TEM} is the normalised TEM contrast, I_{water} is the intensity measured from the areas where the electron beam only passes through water and the SiN_x window, I_{NP} is the intensity measured from the nearby areas of the same liquid chamber with nanoparticles, n_{atom} is the number of atoms (gold for our system) per unit volume, which remains the same for the TEM movie captured without changing experimental conditions (e.g., same exposure time, magnification, etc.), σ_{cross} is the absorption cross-section and t is the thickness of the materials. Under the assumption that there is no additional contribution from the nanoprisms being in a strong diffraction condition, the measured image intensity of a single column under TEM is thus

$$I_{\text{NP}} = I_{\text{water}}\text{e}^{-n_{\text{atom}}\sigma_{\text{cross}}t} , \tag{S2}$$

which depends monotonically on the thickness t. The gradual shift of intensities towards a lower value shows that the thickness of stacked columns (i.e., number of prisms inside the columns) increases over time (Supplementary Figure 6b,c). This relation also implies that the two neighbouring columns tracked in Supplementary Figure 6c, although they started from different intensity values, i.e., different numbers of stacked prisms, stabilised at equal column heights, consistent with the manner in which we designed the simulation. The evened-out column heights are likely due to the fact that the self-assembly occurs in a sealed chamber with limited thickness.

6.2. Tracking of single columns in the crystallisation movies

A customised Matlab code is used to de-noise the raw TEM images and identify the single-column positions in each frame of the liquid-phase TEM movies. The detailed column-tracking procedure is shown in Supplementary Figure 7 using one image of Supplementary Video 4 as an example; we perform the same analysis for other crystallisation movies (Supplementary Videos 4 and 6) and the large-scale hexagonal lattice (Supplementary Video 1) using the same parameters, as they have the same magnification. In these movies, 1 pixel corresponds to 2.6 nm. First, we de-noise the TEM image using an algorithm established previously in single-particle tracking for optical microscopy movies (bpass.m function in the codes provided in Ref. 13), which sharpens the

column contours. We use 1 pixel and 30 pixels as the spatial wavelength cutoffs, which are the input parameters for this function. Next, using the built-in Matlab circle-finding function (imfindcircles.m, with threshold and sensitivity set to 0.01 and 0.95, respectively), as columns have circular projections, we identify the columns from the processed images and track the position of each column from the centroids of the fitted circles. The columns identified via the circle fitting have a range of 12 to 20 pixels in diameter. A correction to the tracked column positions is applied when the centroid positions of two columns are closer than 22.84 pixels (59.4 nm), as this is not physically possible given the dimension of columns. These identifications occur due to the fast motion of columns within single exposure time, which results in elongated columnar projections that are identified as two separate columns. For these cases, the intensity values at the centroid of the two columns are compared and the column with the lower centroid intensity on the filtered image is deleted. The column-tracking error was less than 4.0 pixels.

6.3. Structural characterisation of an ordered hexagonal lattice

We calculate the centre-to-centre distances r of all pairs of neighbouring columns from positions of columns tracked in an ordered lattice (Supplementary Figure 8a) based on the method detailed in Supplementary Note 6.2, obtaining (115 ± 6) nm (full distribution in Supplementary Figure 8b). This centre-to-centre distance is consistent with the value (115.5 nm) predicted for a hexagonal lattice from columns in physical contact (assuming 100 nm for the prism side length and the circumscribed circle of stacked prisms as the column diameter, see Supplementary Figure 8c). In contrast, if the same-sized prisms pack into aligned columns and further crystallise into a honeycomb lattice via side-by-side arrangements, the expected centre-to-centre distance of neighbouring columns is calculated to be much smaller, only 57.7 nm (Supplementary Figure 8d).

6.4. Identification of column phases

The determination of the different states of columns during the crystallisation to the final hexagonal lattice is performed on the liquid-phase TEM movies covering the assembly process from dilute, individual prisms to large-scale ordered crystals. The analysis workflow is summarised in Supplementary Figure 9a. For each TEM frame in one TEM movie, the positions of individual columns are first tracked following the methods described in Supplementary Note 6.2 (Supplementary Figure 9b). Next, based on the tracked column positions, we perform the Voronoi cell analysis and compute the local density of individual columns ρ_j, defined as the inverse of the Voronoi cell area containing column j (Supplementary Figure 9c).

Independently, we also characterise the local hexagonal positional order at the single-column level in each frame of a movie. We first compute the radial distribution function $g(r)$ based on all the column positions (Supplementary Figure 9d), employing a standard method to account for the limited viewing area size by applying a periodic boundary correction[58]. From the first minimum after the first peak of $g(r)$ we define the threshold r_c as the nearest-neighbour bond length. Supplementary Figure 9e shows the corresponding bond network for a typical liquid-phase TEM image. Based on this bond network, we compute the six-fold local bond orientational order

parameter for each column, $\psi_{6j} = \frac{1}{Z_j}\sum_{k=1}^{Z_j}\exp(6i\beta_{jk})$, where Z_j is the number of nearest neighbours of column j, the summation runs over all nearest neighbours and β_{jk} is the angle between the bond that links column j and its kth neighbour and an arbitrarily chosen reference axis. The squared modulus $|\psi_{6j}|^2$ (Supplementary Figure 9f) is used to characterise the local positional order of an individual column at a given time, eliminating the dependence on the choice of reference axis[59,60].

We use these order parameters to classify individual columns. From the local density distribution, we determine a threshold local density $\rho_c = 0.5\rho_0$, where $\rho_0 = 8.66\times10^{-5}$ nm^{-2} is the density of a perfect hexagonal lattice with centre-to-centre distance 115.5 nm (cf. Supplementary Note 6.3, Supplementary Figure 8). We define a column as "gas-like" when $\rho_j < \rho_c$. "Liquid-like" and "solid-like" columns, which have comparable local density, are distinguished by their local structure order. Since $|\psi_{6j}|^2$ only considers the structural order within the first neighbour shell of column j, it is insufficient for this purpose[59]. To differentiate solid and liquid phases we employ the solid bond number ξ_j,[61-63] which characterises how many neighbours belong to a similar solid-like structure. To obtain ξ_j we define $S_{jk} = \text{Re}(\psi_{6j}\psi_{6k}^*)$, following 2D colloidal studies[64]. We compute S_{jk} for each bond for each frame of Supplementary Video 6 (Supplementary Figure 9g). The distribution of S_{jk} shows two distinct peaks (Supplementary Figure 9h), which we use to define a threshold $S_{jk,c} = 0.5$ to determine whether two connected neighbours belong to a similar structure. The solid bond number ξ_j then follows as $\xi_j = \sum_{k=1}^{Z_j} \text{H}(S_{jk} - S_{jk,c})$, where H is the Heaviside function (Supplementary Figure 9i). Following previous studies on colloidal phase transitions[63,65], a threshold value $\xi_c = 4$ is adopted. If a column has $\xi_j \geq \xi_c$, it is defined as a "solid-like" column; if $\xi_j < \xi_c$, the column is defined as "liquid-like" (Supplementary Figure 9j). We confirmed that the precise choice of ξ_c does not change the growth kinetics determined (described in detail in Supplementary Note 6.6). The radial distribution functions presented in main text Figure 3b,c are calculated based on the positions of columns belonging to solid or liquid states during the entire crystallisation process. The criteria we use to distinguish solid and liquid states follows previous literature on phase transitions[63].

6.5. 2D density–structural order histogram and coarse-grained order parameter

The 2D histogram of $(|\psi_{6j}|^2, \rho_j)$ shows two domains (Supplementary Figure 10a). Following Refs. 63,65,66, we replot this histogram employing the coarse-grained order parameter $|\overline{\psi}_{6j}|^2 = |(\sum_{k=0}^{Z^*}\psi_{6k})/(Z^* + 1)|^2$, where Z^* is the number of nearest-neighbour columns in the same state as column j (gas, liquid or solid). The histogram of $(|\overline{\psi}_{6j}|^2, \rho_j)$ shows more well-defined domains (Supplementary Figure 10b). The 2D histogram of only those columns identified as solid-like (Supplementary Note 6.4) shows a region of high structural order (Supplementary Figure 10c) overlapping with the corresponding domain in Supplementary Figure 10b, reconfirming the correct assignment of solid-like columns. Note, the time-varying histogram shown in Figure 2j (main text) was computed based on the accumulated counts of neighbouring 11 frames with the time labelled

according to the central frame, and the total histogram map in Figure 3a (main text) accumulated all the statistics through the whole video (Supplementary Video 6). From both the total histogram map and the time-varying ones, we can see two distinctly populated states, one of high local order and high local density, the "solid" state, and the other of low local order and high local density, the "liquid" as we defined in Supplementary Note 6.4.

6.6. Characterisation of the multi-step crystallisation process

The column state identification of Supplementary Note 6.4 makes it possible to track the temporal evolution of the number of columns in different states (Supplementary Figure 11a) and to display their distribution in colour-labelled time-lapse TEM images (Supplementary Figure 11b). Initially, dilute columns concentrate locally into amorphous domains with high local density and the number of liquid-like columns grows steadily (Supplementary Figure 11, stage I, II). Subsequently, solid-like columns start to emerge, first fluctuating (Supplementary Figure 11, stage III), then growing steadily and rapidly (Supplementary Figure 11, stage IV). At this time, the number of liquid-like columns begins to drop, indicating a conversion of liquid-like columns to solid-like ones.

To compare the crystallisation behaviour in different batches at the same experimental condition, we monitor the growth of clusters of columns connected by nearest -neighbour bonds (cf. bond-network calculation in Supplementary Note 6.4). Figure 3d (main text) shows that the numbers of liquid-like and solid-like columns, respectively, versus cluster size N for different batches are described by a master curve. No normalisation of the column numbers is applied, except that we counted the columns within the views of the same size. Figure 3d illustrates that there is a characteristic cluster size N_c, below which clusters are composed of liquid-like columns (the data have slope 1, indicating that all columns form into the liquid state). Beyond this critical cluster size, solid-like columns start to grow and ultimately dominate the entire cluster. The observation of a single characteristic cluster size N_c in multiple experiments suggests that a thermodynamic driving force governs the multi-step crystallisation process, as discussed in Supplementary Note 6.7 below.

The intermediate liquid region can remain spatially stable for more than 70 s. We monitor a typical spatial region inside the high-density cluster (boxed in Supplementary Figure 11b). The zoomed-in time-lapse TEM images (Supplementary Figure 11c) show that most columns in the region remain liquid-like (blue) before stable solid crystallites emerge from the cluster. The total number of columns inside the selected region stabilizes at around 16 ± 2 during this time, with the fraction of liquid-like columns being 100% most of the time, and that of the solid-like columns close to zero (Supplementary Figure 11d).

Summary of the signatures of two-step crystallisation in the observed pathway

We summarise three experimentally observed signatures supporting that the high-density liquid phase is a metastable intermediate characteristic of two-step crystallisation, instead of an unstable transient state occurring in a one-step process.

The first signature of two-step crystallisation is based on the numbers of solid (N_{solid}) and liquid columns (N_{liquid}) in a high-density cluster composed of N columns (Figure 3d). During crystallisation, both local density and structural order increase. To distinguish a two-step process from the classical one-step process, prior literature has used the variation of N_{solid} *vs.* N (e.g., Figure 2 in Ref. 67; Figure 4 in Ref. 68; Figure 3 in Ref. 60). In those studies, one-step crystallisation was characterised by a proportional increase of N_{solid} with N, resulting from simultaneous fluctuations in density and structure, whereas two-step crystallisation consistently showed a delayed increase in N_{solid}. Initially, the high-density cluster (N) grows to a characteristic size, after which crystalline structure begins to emerge inside the high-density cluster. Our Figure 3d measured from the liquid-phase TEM movies indeed matches the pathway for two-step crystallisation: N_{solid} remains almost zero until the high-density cluster N reaches a characteristic size N_c, corresponding to the definition of two-step crystallisation that structural fluctuations follow density fluctuations[67,69]. Another aspect of Figure 3d is that N_{solid} increases with a *decrease* in N_{liquid}, indicating that solid forms from the liquid phase by consuming the liquid-like columns and confirming that liquid is not merely coexisting with solid[70]. This kinetic feature is further supported by the TEM imaging, where solid nucleates spatially within the liquid (Figure 3d, inset) and by the temporal evolutions of N_{solid} and N_{liquid} (Supplementary Figure 11a), which show that liquid appears first and grows for more than 50 s before being converted into solid.

The second signature of the intermediate liquid phase is the liquid phase peak in the order–density ($|\overline{\psi}_{6j}|^2, \rho_j$) histograms (Figure 2j and Figure 3a). One standard method for detecting precursors or intermediates in phase transition studies is to graph the probability map of building blocks exhibiting certain values of local order parameters, wherein the high-probability phases (peaks in the histogram) are considered either metastable or stable phases (see Figure 3 in Ref. 66; Figures 1b and 2f in Ref. 63). This method relies on a Boltzmann distribution argument: the more populated regions reflect a lower free energy, i.e., more stable states. The ($|\overline{\psi}_{6j}|^2, \rho_j$) histogram (Figure 3a) clearly shows a highly populated region with high local density and low structural order, i.e., a sustained, metastable liquid intermediate. In comparison, transient phases are too short-lived to exhibit such a well-defined, low-energy region in the order parameter space. Moreover, consistent with the evolution of the number of liquid and solid columns described above, Figure 2j shows that the liquid region appears first in the ($|\overline{\psi}_{6j}|^2, \rho_j$) histogram, remains stable, and only becomes less populated after the appearance of solid, consistent with the liquid phase acting as an intermediate in the crystallisation pathway.

The third signature of the liquid phase as an intermediate is the direct imaging of a long-lasting, spatially stable liquid phase before the emergence of solid (Figure 2j and Supplementary Figure 11). Prior studies on two-step crystallisation utilised either real-space images[66] or spectroscopic features (X-ray scattering in Ref. 70) to show the existence of a liquid state prior to the formation of crystals. In accordance with this approach, the top panels in Figure 2j corroborate the evidence from the number of columns in the different phases as well as the time evolution of the order–density histograms. Additional real-space data follows from monitoring the fraction of liquid-like columns within a fixed spatial region (Supplementary Figure 11c,d). For a long time (~70 s), the columns in this region fluctuate in position but maintain 100% liquid column fraction

most of the time, suggesting the long-lasting, spatially stable existence of the liquid phase prior to the emergence of solid. In contrast, for one-step crystallisation, nucleation occurs from density fluctuations that are randomly distributed in in space[71], and therefore such systems do not exhibit a similar spatially stable intermediate.

6.7. Gibbs free energy of column crystallisation

According to a phenomenological two-barrier Gibbs free-energy model proposed for micron-sized colloids[72,73], the formation of a crystalline phase starts with the appearance of an amorphous liquid-like intermediate (Supplementary Figure 12a). The thermodynamic driving force behind this phenomenon can be qualitatively explained from classical nucleation theory by comparing the change in Gibbs free energy ΔG for the gas–liquid and gas–solid transitions versus cluster size N. At a cluster size $N = N_c$, corresponding to the characteristic critical cluster size identified experimentally (main text Figure 3d), the two ΔG curves intersect. Below N_c, the liquid "phase" has a lower free energy, favouring the formation of liquid-like columns as an intermediate; above N_c, the solid phase has a lower free energy. The existence of this crossover has been observed in other systems with two-step crystallisation process such as proteins[67,74-76] and micron-sized colloids[60,68,77-81].

In our system, the first step toward crystallisation is the emergence of liquid-like clusters from gas-like columns. For this step, we obtain the free-energy barrier from the size distribution of liquid-like clusters[60,72,82]. Since the cluster size distribution is invariant over time (Supplementary Figure 12c), we assume that it follows a Boltzmann distribution and calculate the free-energy change ΔG as a function of cluster size N (Supplementary Figure 12d) using $\Delta G(N) - \Delta G(1) = -k_B T \ln(n^L(N)/n^L(1))$, where $n^L(N)$ is the number of liquid clusters of size N. It is noteworthy that the Boltzmann distribution is a reasonable assumption even for situations where a phase transition is taking place (gas to liquid or liquid to solid) but the number of the product clusters (liquid or solid, respectively) is stable over time (Supplementary Figure 12c,e), as demonstrated in previous literature[60,72]. The line tension and chemical-potential difference for the gas–liquid transition are obtained by fitting the free-energy curve in Supplementary Figure 12d. Assuming a circular shape for the cluster, the area fraction of projected columns arranged in a hexagonal pattern is $\eta_c = 0.91$ and the perimeter of a cluster with N columns is $\eta_c^{-\frac{1}{2}}\pi N^{\frac{1}{2}}$ in units of column diameter[60]. Thus, the Gibbs free energy of formation for a 2D cluster containing N columns follows,

$$\Delta G(N) = \eta_c^{-\frac{1}{2}}\pi\Gamma N^{\frac{1}{2}} + \Delta\mu N \,, \tag{S3}$$

with Γ the line tension per column diameter and $\Delta\mu$ the chemical-potential difference between the two states[60]. By fitting the Gibbs free-energy change using Eq. S3 (red line in Supplementary Figure 12d), we estimate the line tension as $\Gamma = 1.0\pm0.1\ k_B T$ per column diameter and the chemical-potential difference as $\Delta\mu = 0.38\pm0.04\ k_B T$. This liquid–gas line tension refers to the Gibbs free-energy difference between columns inside the cluster and those at the cluster surface[71]. We note

that the "gas" phase from which the liquid phase emerges includes both the gas-like columns tracked as yellow dots in Figure 2g–i and the platelets dispersed in the solution. This line-tension calculation only concerns the probability of *liquid* cluster sizes and does not depend on the experimental accuracy of resolving the gas phase.

The same method is also applied to calculate the Gibbs free-energy difference between the solid and liquid states by counting the cluster distribution of solid nuclei inside the pre-formed liquid clusters. The distribution of solid clusters $n^S(N)$, the number of solid clusters of size N, is measured as shown in Supplementary Figure 12e. The Gibbs free-energy change is then calculated as $\Delta G(N) - \Delta G(1) = -k_B T \ln(n^S(N)/n^S(1))$ as shown in Supplementary Figure 12f. By fitting the Gibbs free-energy change using Eq. S3 (red line in Supplementary Figure 12f), we estimate the line tension as $\Gamma = 0.32 \pm 0.03\ k_B T$ per column diameter and the chemical-potential difference as $\Delta\mu = 0.10 \pm 0.02\ k_B T$. The Gibbs free-energy barrier as well as the line tension in the liquid-to-solid transition are lower compared than for the gas-to-liquid case. These measurements thus suggest that the emergence of the liquid intermediate is the rate-limiting step and that the subsequent liquid-to-solid transition occurs smoothly. Due to the absence of solid nucleating directly from gas in our system, we are not able to measure the gas-solid interfacial tension. Qualitatively we expect that due to the larger structural difference between gas and solid than between gas and liquid, the interfacial tension of the former is larger, thereby favoring the liquid intermediate and the two-step pathway.

Supplementary Note 7. Validation of our experimental platform for other nanoparticle systems

The versatility of our approach is explored for gold nanoparticles of other shapes, including concave nanocubes (Supplementary Figure 2a) and nanospheres (Supplementary Figure 2b), each representing a distinctive shape category (concave polygons or isotropic, respectively). Capped with the same charged thiols as the prisms, these nanoparticles are triggered to crystallise through the same process of screening electrostatic repulsion via an increase in ionic strength (Supplementary Videos 8 and 9), validating the robustness of our low-dose liquid-phase TEM platform to probe nanoscale crystallisation. The superlattice symmetry varies with nanoparticle shape. The gold concave nanocubes grow preferentially face-to-face into a simple cubic lattice (Supplementary Figure 13), while nanospheres rapidly pack into hexagonal layers, upon which more spheres attach vertically following the ABC positioning, resulting in a 3D face-centred cubic lattice (Supplementary Figure 14). The Fourier transforms of both superlattices demonstrate high structural order, as the nanoparticles dynamically adjust their positions to minimise defects. However, the crystallisation pathways can be different due to the inherent complexity and richness (surface curvature, ligand patchiness, etc.) associated with nanoscale interactions.

Supplementary Note 8. Coarse-grained model for pairwise interaction calculation

To describe the pairwise interaction between two triangular prisms at all possible relative positions and orientations, we construct a coarse-grained (CG) model in which each prism coated with

charged ligands is discretised as a mesh of beads, placed on stacked hexagonal layers with both intralayer spacing and hexagonal lattice spacing $\Delta_b = 0.5$ nm. We represent the triangular prism shape and surface ligands using $N_1 = 252{,}540$ beads of type 1 (dark pink beads in Supplementary Figure 15a) to model the gold atoms and $N_2 = 54{,}402$ type-2 beads (light pink beads in Supplementary Figure 15a) to model the coating of charged ligands. The type-1 beads form a 15-layer triangular prism with thickness 7.5 nm. The type-2 beads form a triangular prism-shaped monolayer representing the ligands. The resulting prism has a side length of 100 nm and a thickness of 12.5 nm (7.5 nm prism thickness plus 5.0 nm for two monolayers of ligands), matching the dimensions measured in experiment (Supplementary Figure 1)[1].

The type-1 beads have a van der Waals interaction $u_{\text{vdW}}(r_{b-b})$, and the type-2 beads interact via a screened Coulomb potential $u_{\text{el}}(r_{b-b})$ using Debye–Hückel approximation, where r_{b-b} denotes the distance between pairs of interacting beads. The van der Waals interactions between ligands and between ligands and gold atoms are negligible owing to the very small Hamaker constants for hydrocarbon/hydrocarbon and gold/hydrocarbon across water[83]. The interactions $u_{\text{vdW}}(r_{b-b})$ and $u_{\text{el}}(r_{b-b})$ are given by

$$u_{\text{vdW}}(r_{b-b}) = -\frac{H\Delta_b^6}{\pi^2 r_{b-b}^6} , \tag{S4}$$

$$u_{\text{el}}(r_{b-b}) = \frac{Z_b^2 e^2}{4\pi\epsilon_0\epsilon_r r_{b-b}} e^{-\kappa r_{b-b}} = \frac{Z_b^2 l_B}{r_{b-b}} e^{-\kappa r_{b-b}} k_B T , \tag{S5}$$

where $H = 28.9 k_B T$ is the Hamaker constant for gold in water, ϵ_0 the vacuum permittivity, ϵ_r the relative permittivity of water, κ^{-1} the Debye length which depends on the salt concentration via $\kappa^{-1} \approx 0.304/\sqrt{I(M)}$ nm for water at room temperature, $l_B = 0.7$ nm the Bjerrum length of water at 25°C and $Z_b = \sigma\Delta_b^2/e = 0.075$ the effective charge (with $e = 1.6 \times 10^{-19}$ C the unit charge) of each type-2 bead, derived from the surface charge density $\sigma = -0.048$ C/m^2 as measured in experiment (Supplementary Note 5.1 and Supplementary Figure 2). Note that the charge per bead is smaller than the unit charge because we treat the surface charge density as smeared out uniformly over the surface. We assume that the charge density of the ligands on the edges of the prism is the same as on its face.

In our CG model, for computational efficiency we assume that the electrostatic and van der Waals interactions are additive and pairwise. This is not exactly correct, especially at the nanoscale and below, where the size of the building blocks, solvent and ligand molecules are comparable[84]. However, these non-additivity effects appear to be minor in our case, as shown in Supplementary Note 11.8, which summarizes the consistency between simulations/modelling and experiments at different levels. Moreover, we assume that the Debye–Hückel approximation still holds in the ionic strength range of interest. Note that Debye–Hückel theory is only valid in the dilute regime but fails at moderate or high salt concentrations due to the neglect of ion–ion correlations, hydration forces and steric effects. Remarkably, recent experiments[85] have shown that the Debye length is a nonmonotonic function of salt concentration, so that the interaction between charged surfaces in concentrated electrolytes decays exponentially but with a decay length longer than the Debye length. This renders the electrostatic repulsion stronger and longer-ranged than predicted

by Debye–Hückel theory. On the other hand, recent simulation work[86] indicates that charged spherical nanoparticles with either low or high surface charge densities experience strong long-range depletion attractions at high monovalent salt concentrations, with ion clusters serving as the depletants. Owing to these competing effects, it is not clear to what extent in our case the interactions will deviate from the Debye–Hückel approximation (Eq. S5) at high ionic strengths. Empirically, we note that the prism spacings predicted by our CG model exhibit a fair match with experimental measurements over a wide range of ionic strengths (Supplementary Figure 15d). In Supplementary Note 11.8 we provide a more complete list of comparisons between our modelling/simulations and the experiments at different levels, showing good consistency and thus validating our assumptions here.

Based on the interactions $u_{\mathrm{vdW}}(r_{\mathrm{b-b}})$ between type-1 beads and $u_{\mathrm{el}}(r_{\mathrm{b-b}})$ between type-2 beads, the total pairwise interaction E_{tot} between two arbitrarily oriented and positioned prisms in our CG model is then computed by summing over pairwise interactions between beads on the two prisms. The discretisation spacing Δ_{b} is chosen small enough to ensure convergence of this summation. Thus, we define the total pairwise van der Waals interaction E_{vdW} between two prisms as

$$E_{\mathrm{vdW}} = \sum_{i=1}^{N_1} \sum_{j=1}^{N_1} u_{\mathrm{vdW}}(|\mathbf{r}_i - \mathbf{r}_j|) = -\sum_{i=1}^{N_1} \sum_{j=1}^{N_1} \frac{H \Delta_{\mathrm{b}}^6}{\pi^2 |\mathbf{r}_i - \mathbf{r}_j|^6} , \qquad (S6)$$

where the sums over i and j run over all type-1 beads in the first and the second prism, respectively. Here $\mathbf{r}_i$ and $\mathbf{r}_j$ denote the position vectors of the beads being considered, and N_1 is the number of type-1 beads in a prism. Likewise, the pairwise electrostatic interaction E_{el} between two prisms is

$$E_{\mathrm{el}} = \sum_{i=1}^{N_2} \sum_{j=1}^{N_2} u_{\mathrm{el}}(|\mathbf{r}_i - \mathbf{r}_j|) = \sum_{i=1}^{N_2} \sum_{j=1}^{N_2} \frac{Z_{\mathrm{b}}^2 l_B}{|\mathbf{r}_i - \mathbf{r}_j|} e^{-\kappa |\mathbf{r}_i - \mathbf{r}_j|} k_{\mathrm{B}} T , \qquad (S7)$$

where the sums over i and j run over all type-2 beads on the ligand shell of the first and the second prism, respectively, and N_2 is the number of type-2 beads in a prism.

Next, we examine how $E_{\mathrm{tot}} = E_{\mathrm{vdW}} + E_{\mathrm{el}}$ depends on the relative position and orientation of two prisms. Starting from the simplest case, where two prisms are coaxial, parallel and fully aligned ($\Delta\theta = 0$) with a vertical separation d, we compute E_{vdW}, E_{el}, and E_{tot} as a function of d at ionic strengths varying from 0.2 M to 3.0 M, using the CG model. The definitions of d and $\Delta\theta$ for the parallel and coaxial case are illustrated in Figure 2a (main text). As a typical example, Supplementary Figure 15b shows the interaction energy as a function of d at $I = 2.0$ M. The potential minimum is very deep and narrow (Supplementary Figure 15b, inset). We denote the corresponding separation and (minimum) energy of a pair of prisms as d_{min} and C, respectively (identified by the blue triangle in Supplementary Figure 15b). We will refer to C as the coupling constant. Besides this simple fully aligned case ($\Delta\theta = 0$), we compute $E_{\mathrm{tot}} - d$ at different $\Delta\theta$ values at $I = 2.0$ M. As shown in Supplementary Figure 15c, the equilibrium separation at which E_{tot} is minimal remains constant, independent of $\Delta\theta$, whereas the energy minimum becomes less deep when $\Delta\theta$ increases (up to 60°). Thus, the global energy minimum of a pair of parallel and coaxial prisms corresponds to $d = d_{\mathrm{min}}$ and $\Delta\theta = 0$. The strong coupling and the small value of

$d_{\min}$ (~$1.08t_0$ at $I = 2.0$ M, where $t_0 = 12.5$ nm denotes the total thickness of the prism defined in Supplementary Figure 15a) indicates that only minimal tilting of the prism basal planes is permitted and that the parallel two-prism configuration is a representative arrangement to study the energetics of stacked prisms inside a column. The dependence of $d_{\min}$ on ionic strength I is illustrated in Supplementary Figure 15d, where the values for $d_{\min}$ predicted by the CG model are shown to be in good agreement with experimental values, validating our model. Likewise, we compute the coupling constant C *vs.* ionic strength I (Supplementary Figure 15e). As higher salt concentration screens the electrostatic repulsion more effectively, the coupling constant increases in magnitude. The coupling constant will be used as a key parameter to connect the pairwise interaction with ionic strength in our analytical modelling below.

Supplementary Note 9. Derivation of analytical functional forms for inter-particle interaction used in Monte Carlo simulations

The CG model is accurate but computationally very costly. Therefore, we derive an analytical model for use in the Monte Carlo simulations, by approximating the pairwise interaction energy obtained from the CG model along different degrees of freedom by analytical functions that are inexpensive to evaluate. Beyond the coaxial case considered in Supplementary Note 8, we now focus on the case where the two prisms are only required to be parallel but not necessarily coaxial. Therefore, their relative position and orientation can be fully described by four parameters: the vertical separation d, the spin-angle difference $\Delta\theta$, the magnitude of the horizontal displacement x and the angle α (see schematic in Supplementary Figure 16a). The vertical separation d is defined as the distance from the centre of one prism (prism2) to the basal plane of the other prism (prism1 or central prism). The horizontal displacement vector **x** points from the centre of prism1 to the projected centre of prism2 on the basal plane of prism1. The magnitude of **x** is denoted by x and its direction is measured by the angle α ($\in [-\pi/3, \pi/3]$ owing to the threefold symmetry) between **x** and the orientation vector (defined as the vector from the prism centre through an arbitrary vertex of its triangular basal plane, shown by the red arrows in Supplementary Figure 16a) of prism1. The spin-angle difference $\Delta\theta$ ($\in [-\pi/3, \pi/3]$) is defined as the angle between the orientation vector of prism1 (red arrows) and the projection of the orientation vector of prism2 on the basal plane of prism1 (green arrow). For two parallel prisms, the assignment of prism1 and prism2 does not make a difference for the values of d, $\Delta\theta$, α or x. However, the order does make a difference when the basal planes of two prisms are not parallel, where we will have unequal $d_{i \to j}$ and $d_{j \to i}$; $x_{i \to j}$ and $x_{j \to i}$; $\Delta\theta_{i \to j}$ and $\Delta\theta_{j \to i}$; and $\alpha_{i \to j}$ and $\alpha_{j \to i}$, depending on which prism's basal plane is used for the measurement (see Supplementary Note 9.4 for details).

Due to the strong screening of the electrostatic repulsion in the range of ionic strengths considered here (0.2 to 3.0 M), the total interaction energy E_{tot} between two parallel prisms computed from the CG model consists of a short-range repulsive contribution and a relatively long-ranged attractive contribution (see Supplementary Figure 15b for an example). The left panel of Supplementary Figure 16b shows a schematic illustration of which term dominates in different regions around a central prism (prism1), according to the CG model. To simplify the analytical modelling, we approximate the repulsive part of E_{tot} by merely the volume exclusion of the prisms

22

in the analytical model (cf. right panels of Supplementary Figure 16b,c), whereas the remaining attractive part of E_{tot} at larger distances, which is more complicated, is approximated by analytical functions of d, x, $\Delta\theta$ and α derived from the fitting procedures detailed below. A direct consequence of this simplification is that unlike the repulsive region in the CG model (whose boundary shrinks or expands with ionic strength), the boundary of the excluded-volume region (orange in Supplementary Figure 16b) in the analytical model is fixed by the geometry of the prism, e.g., the minimum-energy separation d_{min} in the analytical model becomes simply the total thickness of the prism t_0 regardless of ionic strength (Supplementary Figure 16c, right panel). As shown in Supplementary Figure 16b, inside the attractive region the configuration of the two parallel prisms can be classified as either face-to-face (green region) or side-by-side (purple region); we will derive functional forms of the pairwise interaction energy (attractive part) for these two types of configurations below, see Supplementary Notes 9.1 and 9.2.

Throughout this Supplementary Note, all lengths are expressed in dimensionless units, measured in terms of the total prism thickness $t_0 = 12.5$ nm, and denoted by an asterisk.

9.1. Face-to-face configurations

9.1.1. Dependence of interaction energy on spin-angle difference $\Delta\theta$ (at $d^* = d^*_{\text{min}}$, $x^* = 0$)

The pairwise interaction energy $E_{\text{tot}}(d^* = d^*_{\text{min}}, \Delta\theta, x^* = 0)$ between two coaxial parallel prisms at the minimum-energy separation *vs.* the spin-angle difference $\Delta\theta$ is computed using the CG model at various ionic strengths ranging from 0.2 to 3.0 M. We find that the curve for $E_{\text{tot}}(d^* = d^*_{\text{min}}, \Delta\theta, x^* = 0)$ *vs.* $\Delta\theta$ can be fitted very well with a cosine function,

$$E_{\text{tot}}(d^* = d^*_{\text{min}}, \Delta\theta, x^* = 0) = C + \frac{\Delta E}{2}(1 - \cos 3\Delta\theta), \qquad (S8)$$

where $\Delta E = E_{\text{tot}}\left(d^* = d^*_{\text{min}}, \Delta\theta = \frac{\pi}{3}, x^* = 0\right) - E_{\text{tot}}(d^* = d^*_{\text{min}}, \Delta\theta = 0, x^* = 0)$ is the difference in total interaction energy between the anti-aligned and aligned cases, and C is the interaction energy minimum between two coaxial and parallel prisms $E_{\text{tot}}(d^* = d^*_{\text{min}}, \Delta\theta = 0, x^* = 0)$, as defined in Supplementary Note 8, which only depends on the ionic strength I (see Supplementary Figure 15e). As shown in Supplementary Figure 17a, the effective form Eq. S8 works well for typical ionic strengths in the range probed, $I = 0.5$, 1.0 and 2.5 M. The interaction energy difference ΔE (labelled in Supplementary Figure 17a) is directly related to the coupling constant C (or ionic strength I) as shown in Supplementary Figure 17b, following a linear dependence $\Delta E = -0.23C - 1$. Thus, in the analytical model we write the pairwise energy as a function of $\Delta\theta$ as

$$E_{\text{tot}}(d^* = d^*_{\text{min}}, \Delta\theta, x^* = 0) = C - \frac{0.23C + 1}{2}(1 - \cos 3\Delta\theta). \qquad (S9)$$

9.1.2. Dependence of interaction energy on vertical separation d^* (at $x^* = 0$)

The magnitude of the pairwise interaction E_{tot} (the attractive part) between two coaxial parallel prisms decreases as the separation d^* increases (Supplementary Figures 15b and 17c). This decay can be fitted by $E_{tot}(d^* > d^*_{min}, \Delta\theta, x^* = 0) = E_{tot}(d^* = d^*_{min}, \Delta\theta, x^* = 0) \cdot (d^*_{min}/d^*)^4$ at different ionic strengths and $\Delta\theta$ values. As an example, we plot the full range of $E_{tot}(d^*, \Delta\theta, x^* = 0)$ *vs.* d^*/d^*_{min} at ionic strength $I = 2.0$ M for two extreme $\Delta\theta$ values: $\Delta\theta = 0$ and $\Delta\theta = \pi/3$ in Supplementary Figure 17c, where the squares are the data computed from the CG model and the red solid lines represent the analytical model,

$$E_{tot}(d^* \geq d^*_{min}, \Delta\theta, x^* = 0) = \frac{E_{tot}(d^* = d^*_{min}, \Delta\theta, x^* = 0) \cdot d^{*4}_{min}}{d^{*4}}$$

$$= \frac{C}{d^{*4}} - \frac{(0.23C + 1)}{2d^{*4}}(1 - \cos 3\Delta\theta). \qquad (S10)$$

The last equality follows since $d^*_{min} = 1$ in the analytical model due to the approximation of the repulsive part of the pairwise energy by the excluded-volume interaction.

9.1.3. Dependence of interaction energy on horizontal displacement x^*

Now we turn to the off-centre case where the second prism has a horizontal displacement with respect to the first prism with magnitude x^* and direction characterised by the angle α ($-\pi/3 \leq \alpha \leq \pi/3$), as defined in Supplementary Figure 16a. To determine the dependence of the attractive part of the pairwise interaction energy E_{tot} on x^* at different values of $\Delta\theta$ and α, we consider six special cases listed in Supplementary Figure 17d, where the two prisms are perfectly aligned ($\Delta\theta = 0$) or anti-aligned ($\Delta\theta = \pi/3$) and the displacement angle α is chosen to be 0, $\pi/6$ or $\pi/3$. We observe that the qualitative dependence of E_{tot} on x^* remains similar at different ionic strengths and vertical separations d^*. As an illustration, we plot the interaction energy between two prisms at the minimum-energy separation $d^* = d^*_{min}$ as a function of x^* for the above 6 cases at ionic strength $I = 2.0$ M in Supplementary Figure 17e ($\Delta\theta = 0$ with $\alpha = 0, \pi/6, \pi/3$) and Supplementary Figure 17f ($\Delta\theta = \pi/3$ with $\alpha = 0, \pi/6, \pi/3$) obtained from the CG model. For all curves, the dependence on x^* can be described by a cosine function,

$$E_{tot}(d^* \geq d^*_{min}, \Delta\theta, x^*, \alpha) = \frac{1}{2}E_{tot}(d^* \geq d^*_{min}, \Delta\theta, x^* = 0)\left(1 + \cos\frac{\pi x^*}{x^*_c(\Delta\theta, \alpha)}\right), \qquad (S11)$$

where $E_{tot}(d^* \geq d^*_{min}, \Delta\theta, x^* = 0)$ is defined in Eq. S10. The cutoff distance x^*_c in the above expression determines the off-centre distance beyond which the interaction energy is negligible, i.e., $E_{tot}(d^* = d^*_{min}, \Delta\theta, x^* \geq x^*_c) = 0$. As shown in Supplementary Figure 17e,f, x^*_c is insensitive to α at $\Delta\theta = 0$, but increases with decreasing α at $\Delta\theta = \pi/3$. We qualitatively capture this trend by setting $x^*_c = 6.2$ independently of α when $\Delta\theta \leq \pi/6$, whereas for the more misaligned case $\Delta\theta > \pi/6$ we set $x^*_c = 8.0$ for $\alpha \leq \pi/18$, $x^*_c = 6.5$ for $\pi/18 < \alpha < \pi/6$ and $x^*_c = 5.2$ for $\pi/6 \leq \alpha \leq \pi/3$. Combining Eqs. S5–S8, the general analytical form for the attractive part of the pairwise energy, $E_{tot}(d^* \geq d^*_{min}, \Delta\theta, x^*, \alpha)$, between two parallel prisms arranged in a face-to-face fashion can be summarised as

$$E_{\text{tot}}(d^* \geq d_{\text{min}}^*, \Delta\theta, x^*, \alpha) = \left[\frac{2C - (0.23C + 1)(1 - \cos 3\Delta\theta)}{4d^{*4}}\right]\left(1 + \cos\frac{\pi x^*}{x_c^*(\Delta\theta, \alpha)}\right). \quad (S12)$$

This equation covers all the different cases discussed in Supplementary Notes 9.1.1–9.1.3. Combination of Eq. S12 with the excluded-volume repulsion $E_{\text{tot}}(d^* < d_{\text{min}}^*, \Delta\theta, x^*, \alpha) = +\infty$, yields the full pairwise interaction energy for face-to-face configurations.

9.2. Side-by-side configurations

We now consider the configurations where the centre of one prism is located in the 'side-by-side' region (purple region in Supplementary Figure 16b) of the other prism, see inset of Supplementary Figure 18a. Starting from the simplest case where the two prisms are placed on the same plane with zero vertical separation ($d^* = 0$) and oriented such that $\Delta\theta = \alpha = \pi/3$, we compute their pairwise interaction energy $E_{\text{tot}}(d^* = 0, \Delta\theta = \alpha = \pi/3, x^*)$ vs. x^* using the CG model at ionic strengths ranging from 0.2 to 3.0 M. We find that the data at different ionic strengths exhibit a common trend. As shown in Supplementary Figure 18a, the curve $E_{\text{tot}}(d^* = 0, \Delta\theta = \alpha = \pi/3, x^*)$ vs. x^* at $I = 2.0$ M has a well-defined minimum side-by-side total interaction energy C_{side} and horizontal displacement x_{min}^*. Since E_{tot} shows a rapidly increasing repulsion as x^* decreases below x_{min}^*, we use the excluded-volume interaction of the prisms to model their repulsion, similar to the analytical model for the face-to-face configurations (Supplementary Note 9.1). Therefore, the minimum-energy horizontal displacement x_{min}^* in the analytical model is the centre-to-centre distance between two fully attached side-by-side prims, x_0^* (defined in Supplementary Figure 18a, inset). In this arrangement, C_{side} (i.e., $E_{\text{tot}}(d^* = 0, \Delta\theta = \alpha = \pi/3, x^* = x_{\text{min}}^*)$), is directly related to the coupling constant C (the global interaction energy minimum for face-to-face configurations, cf. Supplementary Note 9.1), as shown in Supplementary Figure 18b, which illustrates the linear fit $C_{\text{side}} = 0.15C + 0.75$. Our general model for the attractive part of the interaction energy, $E_{\text{tot}}(x^* \geq x_{\text{min}}^*)$, is described in detail below in Supplementary Notes 9.2.1 and 9.2.2.

As a matter of simplification, we note that $|\Delta\theta| \approx |\alpha| \approx \pi/3$ holds for all side-by-side configurations (purple region in Supplementary Figure 16b) and therefore we approximate the interaction energy $E_{\text{tot}}(d^*, \Delta\theta, x^*, \alpha)$ between two side-by-side prisms by $E_{\text{tot}}(d^*, \Delta\theta = \alpha = \pi/3, x^*)$. The justification for this assumption is that the pairwise attraction for the side-by-side configurations is only substantial when the two edges are close enough (see Supplementary Figure 18a), where $|\Delta\theta|$ and $|\alpha|$ cannot deviate significantly from $\pi/3$ for two non-overlapping prisms. For example, if we choose the cutoff for the horizontal distance $x_c^* = 5.2$ (as introduced below), we have $|\Delta\theta| > 50°$ and $|\alpha| > 35°$, and our approximation introduces an error within k_BT.

9.2.1. Dependence of interaction energy on horizontal displacement x^* (at $d^* = 0$)

To examine the dependence of the pairwise interaction energy between two side-by-side prisms on the horizontal displacement x^*, we first consider zero vertical separation, $E_{\text{tot}}(d^* = 0, \Delta\theta =$

$\alpha = \pi/3, x^*$). The trend of the curves for $E_{\text{tot}}(d^* = 0, \Delta\theta = \alpha = \pi/3, x^*)$ *vs.* x^* is qualitatively similar for all ionic strengths examined, and we choose $I = 2.0$ M for illustration purposes. Supplementary Figure 18c shows E_{tot} *vs.* reduced distance $x^*/x^*_{\min}$ ($x^*_{\min} = x^*_0$ in the analytical model, as discussed above) for this case, where the squares represent the data from the CG model. The short-range repulsive part of E_{tot} at $x^* < x^*_{\min}$ is well described by the excluded-volume repulsion (vertical red line at $x^* = x^*_{\min}$). We approximate the attractive part of the total energy at $x^* \geq x^*_{\min}$ via $E_{\text{tot}}(d^* = 0, \Delta\theta = \alpha = \pi/3, x^*) = Y/x^{*4} + Z$, with Y and Z to be determined from the boundary conditions at $x^* = x^*_{\min}$ and at the cutoff $x^* = x^*_c$,

$$
\begin{cases}
E_{\text{tot}}\left(d^* = 0, \Delta\theta = \alpha = \dfrac{\pi}{3}, x^* = x^*_{\min}\right) = \dfrac{Y}{x^*_{\min}{}^4} + Z = C_{\text{side}} = 0.15C + 0.75 \\[4mm]
E_{\text{tot}}\left(d^* = 0, \Delta\theta = \alpha = \dfrac{\pi}{3}, x^* = x^*_c\right) = \dfrac{Y}{x^{*4}_c} + Z = 0 \qquad (x^*_c = 5.2)
\end{cases}
\tag{S13}
$$

For simplicity, the cutoff distance is chosen as $x^*_c = 5.2$ for all ionic strengths (the same as the face-to-face case when $\Delta\theta = \alpha = \pi/3$, see Supplementary Note 9.1.3). Equation S13 yields $Y = C_{\text{side}}x^*_{\min}{}^4 x^{*4}_c / (x^{*4}_c - x^*_{\min}{}^4)$ and $Z = -C_{\text{side}}x^*_{\min}{}^4 / (x^{*4}_c - x^*_{\min}{}^4)$. Thus, in the analytical model the attractive part of the pairwise interaction energy for the side-by-side configuration ($\Delta\theta = \alpha = \pi/3$) at $d^* = 0$ as a function of x^* is

$$
\begin{aligned}
E_{\text{tot}}\left(d^* = 0, \Delta\theta = \alpha = \dfrac{\pi}{3}, x^* \geq x^*_{\min}\right) &= \dfrac{x^*_{\min}{}^4}{x^{*4}_c - x^*_{\min}{}^4}\left(\dfrac{x^{*4}_c}{x^{*4}} - 1\right)(0.15C + 0.75) \\[3mm]
&= \dfrac{x^{*4}_0}{x^{*4}_c - x^{*4}_0}\left(\dfrac{x^{*4}_c}{x^{*4}} - 1\right)(0.15C + 0.75) \qquad (\text{with } x^*_c = 5.2).
\end{aligned}
\tag{S14}
$$

Supplementary Figure 18c shows this expression (solid red curve), with $x^*_{\min} = x^*_0$.

9.2.2. Dependence of interaction energy on vertical separation d^*

The pairwise interaction energy E_{tot} for side-by-side configuration *vs.* the vertical separation d^* is plotted in Supplementary Figure 18d for different values of the horizontal distance x^* at $I = 2.0$ M. Since the CG data (symbols) exhibit a fairly linear dependence on d^*, we approximate it as

$$
\begin{aligned}
E_{\text{tot}}\left(d^*, \Delta\theta = \alpha = \dfrac{\pi}{3}, x^*\right) & \\
= d^* E_{\text{tot}}\left(d^* = 1, \Delta\theta = \alpha = \dfrac{\pi}{3}, x^*\right) &+ (1 - d^*)E_{\text{tot}}\left(d^* = 0, \Delta\theta = \alpha = \dfrac{\pi}{3}, x^*\right),
\end{aligned}
\tag{S15}
$$

where $E_{\text{tot}}(d^* = 1, \Delta\theta = \alpha = \pi/3, x^*)$ follows from Eq. S12 in the face-to-face case and $E_{\text{tot}}(d^* = 0, \Delta\theta = \alpha = \pi/3, x^*)$ from Eq. S14. The curves for this analytical model are plotted in Supplementary Figure 18d (solid red curves), showing an overall good agreement.

Thus, we obtain the general form of the attractive part of the pairwise total energy between two side-by-side parallel prisms ($\Delta\theta = \alpha = \pi/3$) with vertical separation d^* (< 1) and horizontal distance x^* ($\geq x^*_{min}$),

$$E_{tot}\left(d^*, \Delta\theta = \alpha = \frac{\pi}{3}, x^* \geq x^*_{min}\right)$$

$$= d^* \frac{C - (0.23C + 1)}{2}\left(1 + \cos\frac{\pi x^*}{x^*_c}\right) + (1 - d^*)\frac{x_0^{*4}}{x_c^{*4} - x_0^{*4}}\left(\frac{x_c^{*4}}{x^{*4}} - 1\right)(0.15C + 0.75), \quad (S16)$$

where $x^*_c = 5.2$ and the only control parameter is the coupling constant C (or the ionic strength I).

9.3. Summary of the analytical functional forms for the pairwise interaction energy between two parallel prisms

Based on the pairwise interactions for face-to-face (Supplementary Note 9.1) and side-by-side (Supplementary Note 9.2) configurations, the pairwise total energy between two *parallel* prisms with vertical separation d^*, horizontal centre-to-centre distance x^*, spin-angle difference $\Delta\theta$ and horizontal relative direction α can be fully described by the volume exclusion of the prisms plus the analytical function $E_{tot}(d^*, \Delta\theta, \alpha, x^*)$,

$$\begin{cases} \approx E_{tot}\left(d^*, \Delta\theta = \alpha = \frac{\pi}{3}, x^*\right) = \dfrac{d^*[C - (0.23 \cdot C + 1)]\left(1 + \cos\dfrac{\pi x^*}{x_c^*\left(\frac{\pi}{3}, \frac{\pi}{3}\right)}\right)}{2} \\ \qquad + \dfrac{(1 - d^*)(0.15 \cdot C + 0.75)\left(x_c^*\left(\frac{\pi}{3}, \frac{\pi}{3}\right)^4 - x^{*4}\right)x_0^{*4}}{\left(x_c^*\left(\frac{\pi}{3}, \frac{\pi}{3}\right)^4 - x_0^{*4}\right)x^{*4}} \quad (0 \leq x^* \leq x_c^*, 0 \leq d^* < 1) \\ = \left[\dfrac{2C - (0.23 \cdot C + 1)(1 - \cos 3\Delta\theta)}{4d^{*4}}\right]\left(1 + \cos\dfrac{\pi x^*}{x_c^*(\alpha, \Delta\theta)}\right) \quad (0 \leq x^* \leq x_c^*, 1 \leq d^* \leq d_c^*) \\ = 0 \qquad\qquad\qquad\qquad\qquad\qquad\qquad\qquad\qquad (x^* > x_c^* \text{ or } d^* > d_c^*) \end{cases} \quad (S17)$$

where the coupling constant C (which is also the global energy minimum for face-to-face configurations) is the only control parameter, directly related to the ionic strength I. The cutoff distance x_c^* is assigned based on the rule introduced in Supplementary Note 9.1.3. For computational efficiency, the cutoff for the vertical separation is set to the fairly small value $d_c^* = 3.0$ (i.e., $E_{tot}(d^* > d_c^*, \Delta\theta, x^*, \alpha) = 0$). This is justified by the d^{*-4} decay of E_{tot} versus d^* and guarantees a relative error of less than 1.2%.

9.4. Generalisation of the analytical model to nonparallel pairs and the approximations being made

The analytical forms presented in the previous Supplementary Notes apply to prisms that are nearly parallel. For nonparallel prism pairs, there are additional degrees of freedom to be taken into

account. However, due to the short-range character of the interactions (e.g., the cutoff distance for the vertical separation $d_c^* = 3.0$), two prisms within the same column must be very close and almost parallel to have a nonzero pairwise interaction. In addition, the attraction between prisms and the substrate (see Supplementary Note 10) promotes the vertical growth of columns on the substrate, so that most prisms are nearly parallel with each other and with the substrate. Therefore, we impose in our analytical model that two prisms have nonzero interaction energy only if $|\hat{\mathbf{n}}_A \cdot \hat{\mathbf{n}}_B| > 0.95$, where $\hat{\mathbf{n}}_A$ and $\hat{\mathbf{n}}_B$ are the normal vectors of the two prisms, respectively. This requirement in the analytical model promotes nematic order of the system and artificially lowers the probability of certain rare nonequilibrium configurations, e.g., face-to-edge arrangements, but does not affect equilibrium configurations.

For near-parallel prisms, the interaction zone around a central prism in the analytical model is shown in Supplementary Figure 19a,b for face-to-face and side-by-side configurations, respectively. The combined interaction zone (green and purple regions) around the central prism appears as an approximately cylindrical shape due to the simplification (in the schematic only) that x_c^* is a constant. Since x_c^* varies with $\Delta\theta$ and α, the actual contour is considerably more complicated. As mentioned at the beginning of Supplementary Note 9 and shown in Supplementary Figure 16a, a pair of non-parallel prisms (i and j) has unequal interaction parameters when i and j are exchanged, i.e., the pairs $d_{i \to j}^*$ and $d_{j \to i}^*$; $\Delta\theta_{i \to j}$ and $\Delta\theta_{j \to i}$; $\alpha_{i \to j}$ and $\alpha_{i \to j}$; and $x_{i \to j}^*$ and $x_{j \to i}^*$ are not identical. To eliminate this geometric asymmetry, we employ their average as the true pairwise interaction energy,

$$E_{\text{tot}}^{ij} = \frac{1}{2} \left[E_{\text{tot}}\left(d_{i \to j}^*, x_{i \to j}^*, \Delta\theta_{i \to j}, \alpha_{i \to j}\right) + E_{\text{tot}}\left(d_{j \to i}^*, x_{j \to i}^*, \Delta\theta_{j \to i}, \alpha_{j \to i}\right) \right], \qquad \text{(S18)}$$

where $E_{\text{tot}}\left(d_{i \to j}^*, x_{i \to j}^*, \Delta\theta_{i \to j}, \alpha_{i \to j}\right)$ and $E_{\text{tot}}\left(d_{j \to i}^*, x_{j \to i}^*, \Delta\theta_{j \to i}, \alpha_{j \to i}\right)$ are defined in Eq. S17.

Lastly, we examine the validity of restricting pairwise attractions to near-parallel prisms. The requirement $|\hat{\mathbf{n}}_A \cdot \hat{\mathbf{n}}_B| > 0.95$ corresponds to tilt angles $\gamma < 18.2°$. For two coaxial cases, $\Delta\theta = 0$ and $\Delta\theta = \pi/3$ (Supplementary Figure 19c), we compute the pair potential from the CG model as a function of tilt angle at different separations $d_{1 \to 2}^*$ (Supplementary Figure 19d,e). The data from the CG model (symbols) agree fairly well with the analytical model Eq. S18 (red lines). Note that at each value for $d_{1 \to 2}^*$, beyond a certain tilt angle γ the interaction energy increases sharply due to the strong electrostatic repulsion (CG model) or the excluded-volume interactions (analytical model). In particular, at $d_{1 \to 2}^* = d_{\min}^* = 1$ no tilting is permitted in the analytical model.

Supplementary Note 10. Prism–substrate interaction employed in the Monte Carlo simulations

As reported earlier[56] and also observed in the present work, there is a short-range attraction between the substrate and the prisms. Since prisms attracted to the surface are greatly confined in their motion, the substrate–prism attraction plays an important role in templating the assembly of

the final hierarchical lattice and promoting the vertical growth of stacks of prism (see main text Figure 1d–g and Supplementary Figure 6).

We model this prism–substrate interaction via an attractive square-well potential with range t_0 from the substrate (Supplementary Figure 19f). Thus, the interaction energy E_{PS} is proportional to the overlap volume between the prism and the interaction zone (V_{in} in Supplementary Figure 19f), $E_{PS} = E_0 V_{in}/V_\Delta$, where $E_0 < 0$ is a constant and $V_\Delta = 16\sqrt{3}t_0^3$ is the total volume of the prism including the coated ligands (i.e., the volume of the prism in the analytical model). Setting the magnitude of E_0 too large will result in prisms first fully covering the entire substrate before forming columns, whereas a too small value will not lead to vertical columns, in contradiction to the experimental observations. Thus, we choose $E_0 = C/2$, where C is the minimum of the prism–prism interaction. The role of the substrate–prism interaction is discussed further in Supplementary Notes 11.4.

Supplementary Note 11. Large-scale canonical Monte Carlo simulations of hierarchical assembly

11.1. Simulation methods

Monte Carlo (MC) simulations are conducted of systems of M_{tot} triangular prisms in a rectangular simulation box in the canonical ensemble. The system is periodic in x and y directions, but finite along the z-axis to make it consistent with the experimental setup. The aspect ratio of the box is chosen to be $L_x : L_y = 2 : \sqrt{3}$, which ensures that the target crystal structure (hexagonal lattice) will not be forbidden by the periodic boundary conditions in the x–y plane[87]. All prisms have pairwise interactions described by the analytical model of Supplementary Note 9, Eqs. S17–S18. For the excluded-volume interactions, overlapping prisms are detected via the Möller–Trumbore ray–triangle interaction algorithm[88].

Each simulation runs for 10^7 MC cycles for equilibration and then another 10^7 MC cycles for production, where a cycle consists of M_{tot} MC moves. In each MC move, a prism is randomly picked for a translation, rotation or spin with respective probabilities 0.4, 0.3 and 0.3. In a rotation, the normal vector of the prism face is rotated to a trial orientation generated by adding a randomly oriented vector with magnitude α_r to the original normal vector. Thus, α_r controls the maximum range of the rotational motion. A spin refers to rotation of the prism around its normal vector within the range $[-\alpha_s, \alpha_s]$. During the equilibration process, α_r and α_s, as well as the maximum displacement of the translational move α_t, are adjusted after every cycle to maintain an acceptance rate of 20%.

The initial configuration of the system consists of $N_{col} = 64$ columns organised on a 2D square lattice in order to accelerate the assembly of individual prisms into columns. There are M prisms inside each column, where M is determined by L_z to achieve an average spacing L_z/M of $1.1 t_0$. We use $M_{tot} = N_{col} \cdot M$ to denote the total number of prisms. Note that the columns are free to disassemble or rearrange themselves during the equilibration cycles. To ensure that the equilibrium structure does not depend on the initial configuration, we also perform simulations starting from

29

more random initial configurations, where the system is composed of M layers within which prisms are randomly distributed and oriented within x–y plane. After a longer equilibration time, such systems arrive at the same final structure as those started from a square-lattice initial configuration.

Since the packing density along the z-axis is controlled by the confinement and does not influence the 2D structural order, we use the 2D packing fraction to describe the concentration of the columns. ϕ_{2D} is defined as the 2D packing faction $\phi_{2D} = N_{col} \cdot A_\Delta / (L_x L_y)$, where A_Δ is the area of the face of a prism and $N_{col} = 64$ in all simulations (ϕ_{2D} is varied from 0.29 to 0.5 which is realised by varying L_x). At each ϕ_{2D}, we vary both the height of the simulation box L_z from $10t_0$ to $25t_0$ (with M and M_{tot} being automatically determined) and the ionic strength I from 0.44 to 3.0 M (by varying C in the model). The parameters used in the large-scale simulations are listed in Supplementary Table 4, in which there are three independent variables: ionic strength I, height of the simulation box L_z and the 2D packing fraction ϕ_{2D}.

11.2. Characterisation of orientational order of a single column

To quantify the in-plane (i.e., x–y) orientational order of the M prisms within a column, we define the orientational order parameter $S_\theta = \max_{\theta_0}\{\sum_{i=1}^{M} \cos[3(\theta_i - \theta_0)]/M\}$, where θ_i denotes the in-plane spin angle (i.e., the angle between the projection of the orientation vector of the prism on the x–y plane and the x axis) of prism i and $\hat{\mathbf{n}} = (\cos\theta_0, \sin\theta_0)$ is the global director for triatic phases. S_θ follows the conventional definition of the triatic order parameter of 2D liquid-crystalline phases due to the three-fold symmetry of triangular prisms. In particular, $S_2 = \max_{\theta_0}\{\sum_{i=1}^{M} \cos[2(\theta_i - \theta_0)]/M\}$ and $S_4 = \max_{\theta_0}\{\sum_{i=1}^{M} \cos[4(\theta_i - \theta_0)]/M\}$ measure the degree of nematic and tetratic ordering of 2D systems[89]. S_θ ranges from 0, corresponding to an orientationally disordered (randomly misaligned) state, to 1, corresponding to a fully ordered (perfectly aligned) state. The calculation of S_θ can be easily converted to an eigenvalue problem by rewriting it as

$$
\begin{aligned}
S_\theta &= \max_{\theta_0} \frac{1}{M} \sum_{i=1}^{M} \left(2\cos^2\left[\frac{3}{2}(\theta_i - \theta_0)\right] - 1\right) \\
&= \max_{\theta_0} \frac{1}{M} \sum_{i=1}^{M} \left[2\left(\cos^2\frac{3\theta_i}{2}\cos^2\frac{3\theta_0}{2} + \sin^2\frac{3\theta_i}{2}\sin^2\frac{3\theta_0}{2} + 2\cos\frac{3\theta_i}{2}\cos\frac{3\theta_0}{2}\sin\frac{3\theta_i}{2}\sin\frac{3\theta_0}{2}\right) - 1\right] \\
&= \max_{\theta_0} \frac{1}{M} \sum_{i=1}^{M} \left(\cos\frac{3\theta_0}{2}, \sin\frac{3\theta_0}{2}\right) \begin{pmatrix} \cos3\theta & \sin3\theta \\ \sin3\theta & -\cos3\theta \end{pmatrix} \begin{pmatrix} \cos\frac{3\theta_0}{2} \\ \sin\frac{3\theta_0}{2} \end{pmatrix}.
\end{aligned}
\tag{S19}
$$

If $\hat{\mathbf{n}}'$ denotes the vector $\left(\cos\frac{3\theta_0}{2}, \sin\frac{3\theta_0}{2}\right)$ and $Q = \frac{1}{M}\sum_{i=1}^{M} \begin{pmatrix} \cos3\theta_i & \sin3\theta_i \\ \sin3\theta_i & -\cos3\theta_i \end{pmatrix}$ is the ordering matrix, we obtain the simplified expression $S_\theta = \max_{\hat{\mathbf{n}}'}\{\hat{\mathbf{n}}' \cdot Q \cdot \hat{\mathbf{n}}'^T\}$. Thus, S_θ is just the largest eigenvalue of the ordering matrix Q, and the director $\hat{\mathbf{n}} = (\cos\theta_0, \sin\theta_0)$ can be obtained from $(\cos(3\theta_0/2), \sin(3\theta_0/2)) = \hat{\mathbf{n}}_0$, where $\hat{\mathbf{n}}_0$ is the normalised eigenvector corresponding to S_θ.

The average columnar orientational order of the system of multiple columns is denoted by $\langle S_\theta \rangle$, where the angular brackets indicate an average over all columns.

The orientational structure of a column can also be quantified by the orientational correlation function $G_3(m) = \langle \cos[3(\theta_i - \theta_{i+m})] \rangle_i$, quantifying the average orientational correlation between prism i and its mth-nearest neighbour within the same column. Fitting $G_3(m)$ with e^{-m/l_c} yields the decay length l_c.

11.3. Characterisation of crystal structure in simulations

To describe the 2D hexagonal order of the columns we first detect and locate each column. Prisms are considered to belong to the same column if their centre-to-centre distance in the x–y plane lies within a certain cutoff. We find that a cutoff of $50/\sqrt{3}$ nm maximises the accuracy. The center position of the column in the x–y plane is calculated by averaging the x–y centre position of each constituent prism. The local hexagonal order of the columns is quantified by the squared modulus of the six-fold bond-orientation order parameter $\left|\psi_{6j}\right|^2$ (see Supplementary Note 6.4 for definition). The cutoff distance used to determine the bonded neighbours is the position of the first minimum after the first peak of the radial distribution function $g(r)$ of the columns, consistent with Supplementary Note 6.4. The global bond-orientation order parameter Ψ_6^{AV} is given by

$$\Psi_6^{\text{AV}} = \langle \frac{1}{N_{\text{col}}} \sum_{j=1}^{N_{\text{col}}} \psi_{6j} \rangle , \tag{S20}$$

where the angular brackets indicate the time average. The square of the absolute value of the bond-orientation order parameter $\left| \Psi_6^{\text{AV}} \right|^2$ is used to characterise the 2D global structural order of the system[87].

The 3D translational order of the prisms is characterised by the diffraction patterns in Figure 1c and Figure 4d (main text), which were generated by computing the structure factor,

$$S(\mathbf{q}) = \frac{1}{M_{\text{tot}}} \langle \sum_{j=1}^{M_{\text{tot}}} \sum_{k=1}^{M_{\text{tot}}} e^{-i\mathbf{q}\cdot(\mathbf{R}_j - \mathbf{R}_k)} \rangle , \tag{S21}$$

where $\mathbf{R}_j$ is the position vector of the center of prism j and the angular brackets denote the temporal average.

The translational order of the prisms along the z axis is characterised by (i) the structure factor $S(q_z) = \langle \sum_{j=1}^{M_{\text{tot}}} \sum_{k=1}^{M_{\text{tot}}} e^{-iq_z(z_j - z_k)} \rangle / M_{\text{tot}}$, where z_j denotes the z coordinate of the centre of prism j, and (ii) the volume fraction profile along the z axis. The latter is defined as the ratio between the volume fraction of prisms whose centres lie in a horizontal slab of volume $L_x L_y \Delta z$ between z and $z + \Delta z$ and the overall volume fraction. This ratio can be written as $\phi(z)/\phi = \langle M(z)V_\Delta/(L_x L_y \Delta z) \rangle / \phi = \langle M(z)L_z/(M_{\text{tot}}\Delta z) \rangle$, where $M(z)$ represents the number of prisms whose centres are located between z and $z + \Delta z$ and V_Δ is the volume per prism. We choose $\Delta z = 0.2 t_0$.

11.4. Role of the confinement along the z axis and the prism–substrate interaction

The combination of top and bottom substrates is not essential to the nanoprism superlattice formation. Previous experiments and simulations (Refs. 90–92 and main text Refs. 24, 25) show that the column formation is independent of the top and bottom substrates. To demonstrate whether confinement affects the further building process, we perform simulations without boundaries, but instead 3D periodic boundary conditions. As shown in Supplementary Figure 20a, under conditions that are otherwise the same as in the confined system, we again obtain the hexagonal lattice from columns stacked with misaligned prisms. Given that both the column configuration and the inter-column interaction are unaffected by the confinement, we conclude that the two-step crystallisation can be retained in the absence of the sandwich geometry.

Nevertheless, to fully reflect experimental conditions in our simulation, we introduce the sandwiching geometry. There are two minor effects brought about by the confinement. First, the positional ordering along the z axis (z coordination of stacking in different columns) disappears in the absence of confinement, as illustrated in Supplementary Figure 20b, which shows the volume fraction profiles $\phi(z)/\phi$ under different boundary conditions. The reason is straightforward: the existence of the bottom substrate and the substrate attraction aligns the bottom-layer prisms on the same lateral plane, and the z-ordering then propagates, because the spacing between prisms within the same column is stable[1]. Second, whereas the 3D periodic systems exhibit no preferential orientation for the columns, the confined systems prefer columns to grow parallel to the substrate due to the reduced symmetry. This was shown in previous experiments[92] and also confirmed by our supplementary simulations in the absence of the prism–substrate attraction (Supplementary Figure 20c), where columns lie down on the surface. However, in our experiments the prism–substrate attraction favors the stacking of prisms on top of the substrate and therefore promotes the columns to grow vertically (i.e., along the z axis) prior to crystallisation. To reflect this aspect of our experimental setup, the substrate–prism attraction (for the bottom substrate only) is employed in the simulations as well.

11.5. Analysis of single-prism rotational motion from the large-scale simulations

As shown in the main text (Figure 4d,e), the final assembled lattice is orientationally disordered. Supplementary Figure 21a shows a histogram of the in-plane angle θ of all prisms in the equilibrated hierarchical lattice, consistent with our observation of orientational randomness. The minor variation (peaks) in the histogram originate from the spatial symmetry of the hexagonal lattice, which makes certain orientations ($\pm\pi/6$) slightly more favourable in a rectangular simulation cell with periodic boundary conditions. The temporal decay of orientational order can be derived from the orientational autocorrelation function $g_{\mathrm{r}}(t) = \langle \frac{1}{M_{\mathrm{tot}}} \sum_{i=1}^{M_{\mathrm{tot}}} \hat{u}_i(t_0) \cdot \hat{u}_i(t_0 + t) \rangle_{t_0}$, where $\hat{u}_i(t)$ is the unit vector that defines the in-plane orientation of prism i at the instance t and the angular brackets denote the ensemble average. Supplementary Figure 21b illustrates that $g_{\mathrm{r}}(t)$ decays more slowly at higher ionic strength, due to the strong orientational correlation between prisms within the same column.

32

11.6. Dependence of 2D hexagonal order on 2D packing fraction ϕ_{2D}

Within the range of packing fractions examined ($0.362 \leq \phi_{2D} \leq 0.433$), the correlation between the global hexagonal order parameter $\left|\Psi_6^{AV}\right|^2$ and the average columnar orientational order $\langle S_\theta \rangle$ is described by a master curve (Figure 4g in main text). In Supplementary Figure 22a,b we illustrate that 2D packing fractions outside this range will suppress the hexagonal order, regardless of $\langle S_\theta \rangle$. In both regimes, $\left|\Psi_6^{AV}\right|^2$ is consistently smaller than 0.5, even at small $\langle S_\theta \rangle$. At lower packing fractions, no crystallisation takes place, whereas higher packing fractions can only be attained for columns consisting of aligned prisms, which then can only crystallise into a honeycomb lattice (if ϕ_{2D} is sufficiently high). The effects of packing fraction on the columnar orientational order $\langle S_\theta \rangle$ are discussed in Supplementary Note 13.5 below.

11.7 Simulation of a 2D nanoprism system

It is noteworthy that the 3D structural details matter critically to the hexagonal lattice of the prism system and our system is far more complicated than a purely 2D system. To demonstrate this point, we conduct simulations of a true 2D system with triangular nanoprisms that are only allowed to move in the *x–y* plane, i.e., just a single layer of prisms. Under the same conditions where the 3D system crystallises into a hexagonal superlattice, this 2D system shows a completely disordered phase (Supplementary Figure 23), reinforcing the essential role of the 3D structure of the columns. Prisms must to be embedded in a 3D liquid volume to make it possible for several layers to stack, thereby accumulating the misalignment between adjacent prisms that results in an isotropic column–column interaction potential, which in turn constitutes the driving force for the crystallisation.

11.8. Consistency between modelling/simulations and experiments

The MC simulations presented are consistent with the liquid-phase TEM experiments on the following levels. First, the pairwise interaction modelled in the simulation correctly predicts the equilibrium inter-prism spacing in the columns measured in experiments at different ionic strengths (Supplementary Figure 15d). Second, on the column level, the prism misalignment in columns given as the equilibrium structure by MC (Supplementary Video 5) matches the TEM images (main text Figure 1e). Third, the computed inter-column interaction strength in the simulations matches the line tension obtained from the cluster analysis in the experiments. Last, the equilibrium (hexagonal) crystal phase observed in the large-scale simulations matches our experimental imaging (main text Figure 1b,c).

Supplementary Note 12. Large-scale Monte Carlo simulations at fixed pressure to study the prism entering process

12.1. Simulation methods

To determine the dependence of osmotic pressure on the 3D volume fraction $\phi = M_{\text{tot}}V_\Delta/(L_xL_yL_z)$ and the ionic strength, isothermal–isobaric (NPT ensemble) Monte Carlo simulations are carried out as well. We simulate a system of $M_{\text{tot}} = 648$ prisms in a simulation box that is periodic in the x and y directions but finite along the z axis, with $L_z = 20t_0$. The system is equilibrated at fixed osmotic pressure using both prism moves (including 40% translation, 30% rotation and 30% spin) and anisotropic volume moves. In each MC cycle, there are on average M_{tot} prism moves and 1 volume move. The volume move is applied only in the x and y directions and maintains the aspect ratio L_x/L_y at $2/\sqrt{3}$. In each volume move, $\Delta L_x/L_x$ and $\Delta L_y/L_y$ range from –0.005 to 0.005. The dimensionless osmotic pressure P^* is defined as $P^* = Pt_0^3/k_BT$. We study the system at three pressures ($P^* = 0.01, 0.02, 0.05$) and vary the ionic strength I from 0.1 to 2.25 M to obtain the relationship between the equilibrium packing fraction ϕ and the ionic strength I at different values of pressure P^*.

12.2. Equation of state

Supplementary Figure 24 shows the equilibrium 3D volume faction of prisms ϕ as a function of ionic strength I at different pressures P^*. At each pressure, ϕ initially increases with increasing ionic strength and then saturates. Conversely, at the same equilibrium volume fraction, the larger pressure value corresponds to smaller ionic strength, meaning that the gradient of I will cause the pressure gradient that concentrates the prisms. This explains why the prisms enter the electron-beam region where the ionic strength is higher than elsewhere at the beginning of the experiment. $P^* = 0.02$ (squares in Supplementary Figure 24) is closest to the crystallisation pressure condition, where $\phi \approx 0.38$ at $I = 0.5$ M.

Supplementary Note 13. Single-column Monte Carlo simulations

13.1. Simulation method

To understand the energetics driving column formation, we examine the dependence of the orientational structure of a single column on the ionic strength I and the number of constituent prisms M. Thus, we perform single-column simulations (see Supplementary Video 5 for an example), where the centre positions of the prisms are fixed and only spin motion around the z axis is allowed, i.e., $\alpha_t = \alpha_r = 0$ and $\alpha_s = 1$. For simplicity, we simulate the most common case where the prisms are coaxial, equally spaced and parallel to the x–y plane. For consistency with the large-scale simulations, we vary the confinement L_z along the z direction from $10t_0$ to $25t_0$, choosing M to set the spacing L_z/M to $1.1t_0$. We set L_x and L_y large enough to avoid interactions between periodic images.

13.2. Helmholtz free-energy calculation in single-column simulations

We calculate the Helmholtz free energy F, scaled entropy TS and interaction energy E of a single column as a function of the orientational order parameter S_θ. The free energy $F(S_\theta)$ is obtained from the distribution $P(S_\theta)$ of S_θ, since $P(S_\theta) \propto e^{-F(S_\theta)/k_B T}$, i.e., $F(S_\theta) = -k_B T \ln(P(S_\theta)) +$ const. The additive constant is only related to the choice of the reference state. Computation of the interaction energy $E(S_\theta)$ then yields the entropic contribution $TS(S_\theta) = E(S_\theta) - F(S_\theta)$. Although this does not provide the absolute entropy, it permits calculation of free-energy barriers.

We apply this approach to two cases: a short column at high ionic strength (Supplementary Figure 25a) and a tall column at low ionic strength (Supplementary Figure 25b). Due to competition between the entropy favouring low S_θ and the interaction energy which is minimised when the prisms are perfectly aligned, the free-energy minimum is located at very different values of S_θ for these two cases, confirming that the orientational order of the column is controlled by both ionic strength and the number constituent prisms.

Owing to the small size of either column, the free-energy well is rather shallow and broad, resulting in large fluctuations in S_θ. Moreover, it is important to note that the orientational order of the columns in the large-scale (many-column) system is also affected by the intercolumn interaction and column packing fraction ϕ_{2D} (see Supplementary Note 13.5 for a comparison of single-column and large-scale simulations). In particular, for the large-scale system at the same condition as in Supplementary Figure 25a, the columns are more aligned and fluctuate less (cf. Figure 4b in main text and Supplementary Video 7) than in the single-column simulations due to strong lateral attractions between columns.

A noteworthy point is that the maximum of the entropy curve in Supplementary Figure 25 is not located at $S_\theta = 0$, the orientationally isotropic state. The reason is that the eigenvalues of the ordering matrix Q (cf. Eq. S19) are dependent on the number of constituting prisms M. As reported previously[93], for an orientationally isotropic system, the largest eigenvalue of Q, which we define as S_θ, decays to zero as $1/\sqrt{M}$. Therefore, for the small systems considered here with number of prisms between 9 and 23, the computed S_θ is nonzero even for a perfectly isotropic column, leading to the entropy maximum at a nonzero value. Therefore, S_θ can give a better estimation of the orientational order when the column is in a more ordered phase or the number of prisms is large.

13.3. Dependence of columnar orientational order on ionic strength

The ionic strength I determines the pairwise interaction profile *vs.* $\Delta\theta$ between two coaxial parallel prisms (Supplementary Figure 26a), and thus affects the relative rotational range quantified by $\Delta\theta_c$ (defined in main text). At low ionic strength, the two prisms have more relative rotational freedom (larger $\Delta\theta_c$). This dependence on ionic strength propagates along the column once prisms are stacked into a column, and thus affects the orientational order of the column. Supplementary Figure 26b confirms that the orientational correlation function $G_3(m)$ of an individual column decays faster at lower ionic strength, indicating a more disordered column as a result of larger $\Delta\theta_c$.

35

13.4. Dependence of column orientational order on the number of constituent prisms

From single column simulations, a random-walk model has been presented to illustrate the dependence of the orientational order on the number of prisms inside the column as shown in Supplementary Figure 27.

## 13.5. Connection between large-scale simulations and single-column simulations

For single-column simulations, the columnar orientational order S_θ depends on ionic strength I and cell height L_z. Supplementary Figure 28a summarises the trends found in Supplementary Notes 13.3 and 13.4, namely that orientational order is promoted by high ionic strength and by small cell height. However, in systems where columns interact with each other, the columnar orientational order is also affected by this interaction and thus also by the column packing fraction ϕ_{2D}. Figure 4f (main text) shows a 2D map of the column-averaged orientational order $\langle S_\theta \rangle$ obtained in large-scale simulations at a representative packing fraction $\phi_{2D} = 0.386$. This map is qualitatively consistent with the single-column results of Supplementary Figure 28a, except for a shift toward larger values.

Supplementary Figure 28b quantifies this correlation via a scatter plot of $\langle S_\theta \rangle$ at various I, L_z and ϕ_{2D} (as listed in Supplementary Table 4) determined in large-scale simulations *vs.* the order parameter S_θ obtained from single-column simulations. For low packing fractions, the data points closely follow $\langle S_\theta \rangle = S_\theta$ (red line), i.e., the single-column simulations provide a good estimation of the columnar orientational order in the large-scale system. $\langle S_\theta \rangle$ is systematically larger than S_θ at large S_θ, due to the additional intercolumn attraction, which is particularly strong at high ionic strength. At higher packing fractions ϕ_{2D}, the shift of $\langle S_\theta \rangle$ toward larger value becomes more apparent due to the decrease of free space for each column, along with the increased intercolumn attraction. In particular, when ϕ_{2D} is large enough (> 0.440), $\langle S_\theta \rangle$ never reaches low values, no matter how small S_θ is, owing to crowding. Within our ϕ_{2D} range of interest ($0.362 \leq \phi_{2D} \leq 0.433$), the single-column order parameter S_θ serves as a good estimator for $\langle S_\theta \rangle$ in the multi-column systems.
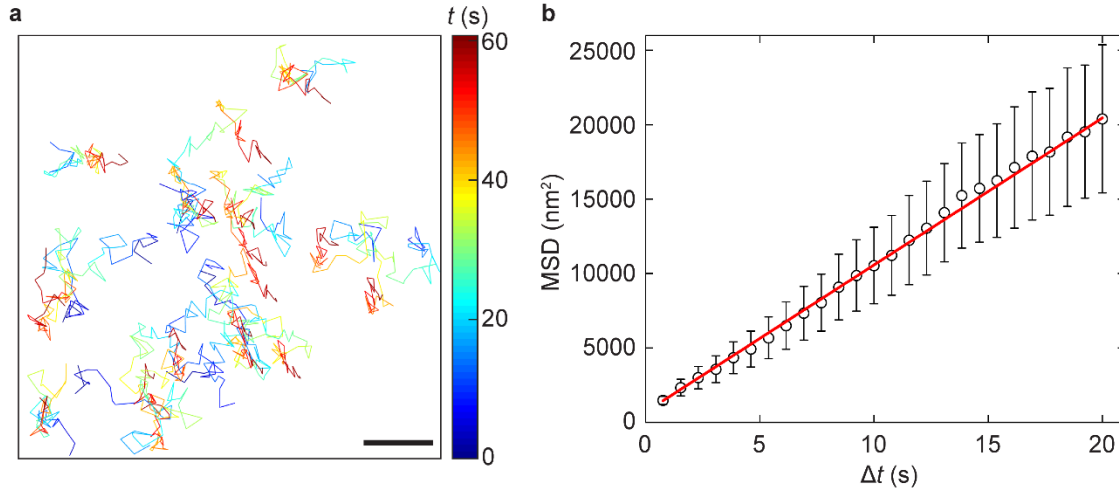
Supplementary Figures
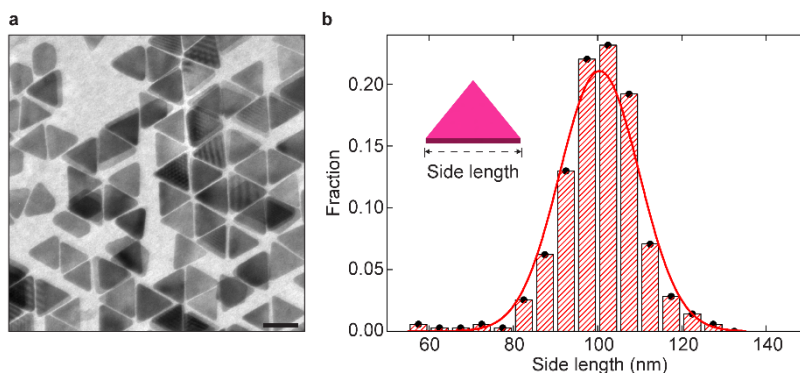
Supplementary Figure 1. Characterisation of gold triangular nanoprisms. (a) TEM image of the gold triangular nanoprism sample after purification. (b) Prism side length distribution of nanoprisms measured from 118 triangular prisms with 354 side lengths in total. The red line shows a Gaussian fit of the distribution with an average of 100.5 nm and a standard deviation of 9.5 nm. Scale bar: 100 nm.
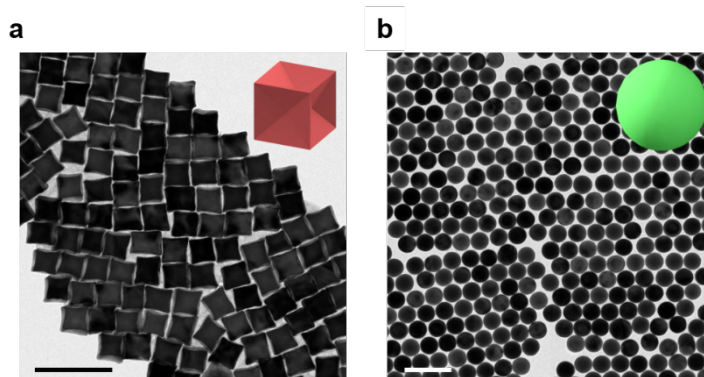
Supplementary Figure 2. Characterisation of gold concave nanocubes and gold nanospheres. Schematics and TEM images of the as-synthesised gold concave nanocubes with an edge length of 62.0 ± 4.6 nm (a) and gold nanospheres with diameter of 76.0 ± 2.2 nm (b). Scale bars: 200 nm.

Supplementary Figure 3. Trajectories and MSD of columns in our liquid-phase TEM work.
(a) Trajectories of liquid-like columns tracked from the first 80 frames of Supplementary Video 4 with the colour denoting elapsed time. Tracking is performed by first identifying the column positions (Supplementary Note 6.2) and then utilizing the Matlab code (imageTrack.m in Ref. 13) to link the column positions in different frames into a continuous single-column trajectory. Scale bar: 200 nm. (b) MSD versus time curve calculated from the trajectories in (a) (mean ± s.d. from trajectories of 33 columns). The red line is the linear fit and the diffusivity ($D_{measure}$) is measured from the slope of the red line following $D_{measure} = MSD/4\Delta t$.
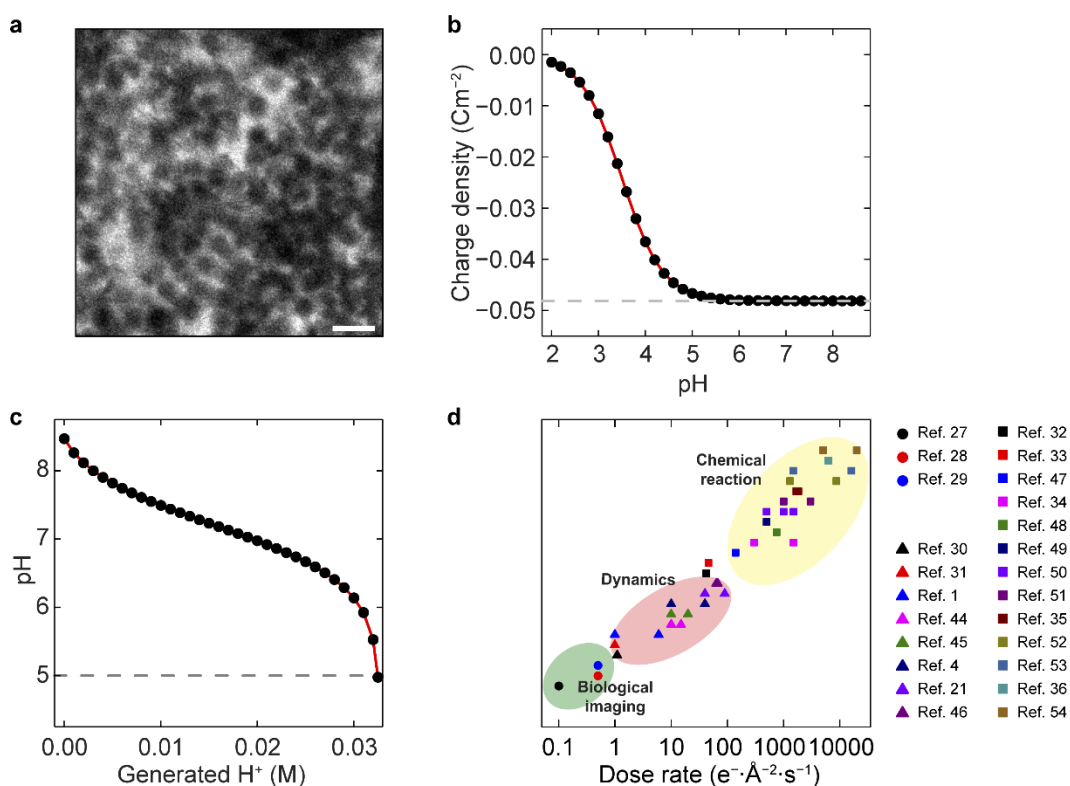
Supplementary Figure 4. Discussion of electron-beam effects. (a) Liquid-phase TEM image of the obtained kinetically trapped aggregate when the liquid-phase TEM imaging is performed for the sample that forms a large-scale superlattice (main text Figure 1b) but at a dose rate of $14.8 \ e^- \cdot \text{Å}^{-2} \cdot s^{-1}$. At this dose rate, the ligands are expected to remain stable, but the ionic strength increase is high enough to screen electrostatic repulsion to the extent that irreversible irregular aggregation occurs[1]. Scale bar: 200 nm. (b) Surface charge density of the nanoprisms as a function of the solution pH. Grey dotted line denotes the charge density at which the carboxylate groups are completely deprotonated. (c) Calculated pH of PBS buffer (initial concentration: 0.0345 M, pH = 8) as a function of additional H^+ ion concentration generated during the TEM imaging. Red line is a guide to the eye. Grey dotted line corresponds to the case pH = 5, which requires about 0.0325 M H^+. (d) Scatter plot of electron beam dose rates used in previous liquid-phase TEM literature and the corresponding electron beam effects. (Adapted with permission from Ref. 1. Copyright 2016 American Chemical Society.) Dose rate values for each reference are listed in Supplementary Table 2.
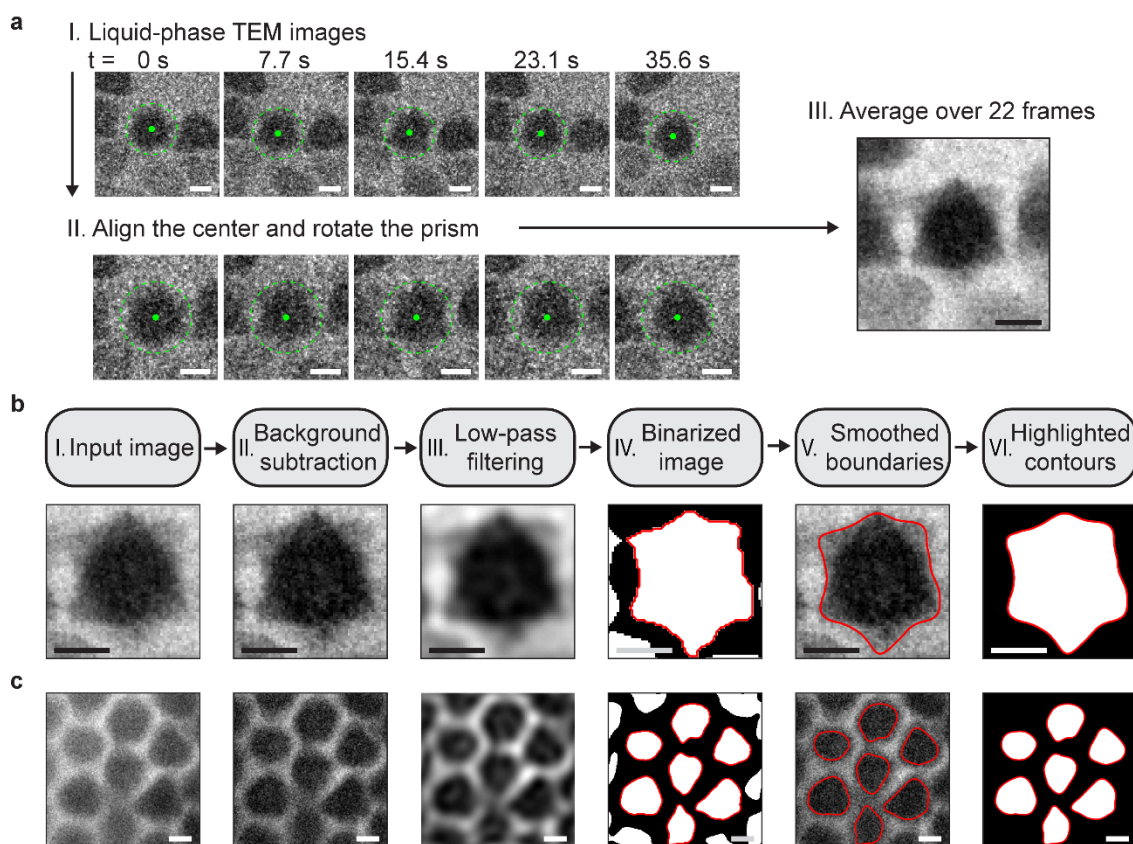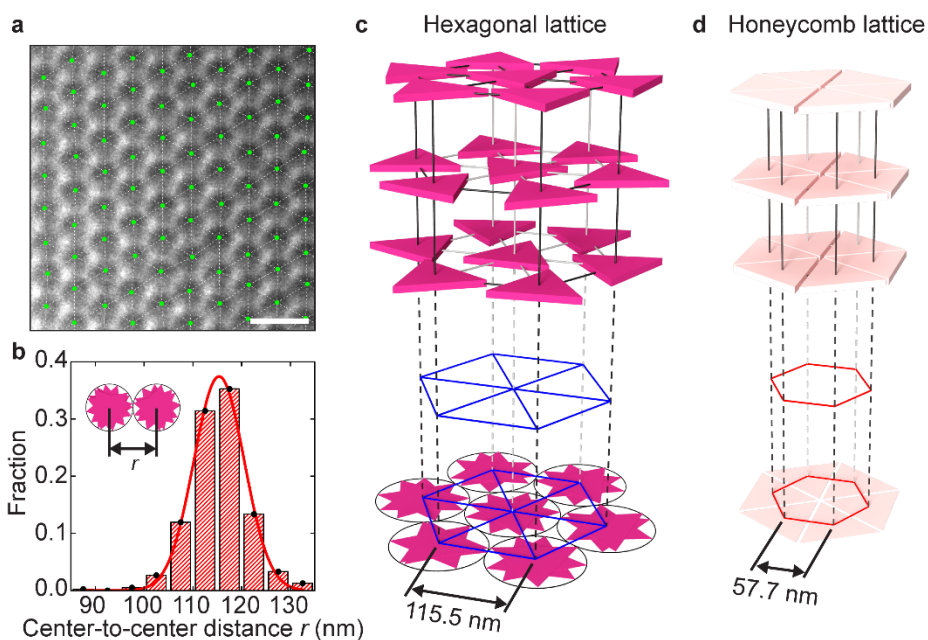
Supplementary Figure 5. Image-processing procedure for contour finding and labelling from TEM images. (a) Image contrast enhancement procedure for the image of two stacked prisms. I. Five liquid-phase TEM images (out of a total of 22 frames chosen from Supplementary Video 2) are shown as examples, with centre positions (green dots) measured from the circumscribed circles (green circles) of each prism pair. II. The prisms are repositioned and rotated to centre and align the prisms in each image. III. Final high-contrast image acquired by averaging over 22 frames after repositioning and reorientation. (b) Contour-finding and labelling process for two stacked prisms. Top: Work flowchart from input TEM images to output contours of stacked prisms. Bottom: starting from the contrast-enhanced images (I), a series of built-in Matlab functions are applied to subtract the background (II) and filter noise to further enhance the contrast (III). The image is then binarised with the contour identified (raw contour shown as red line in IV). The contour is smoothed and overlaid onto the TEM images with background subtracted (V). To highlight the shapes of the structure, the contour of interest is selected and plotted on a black background (VI). (c) Contour finding and labelling of the short columns with rugged projections. The same process is followed as in (b), with modifications of the parameters (details in Supplementary Table 3). Scale bars in all panels: 50 nm.
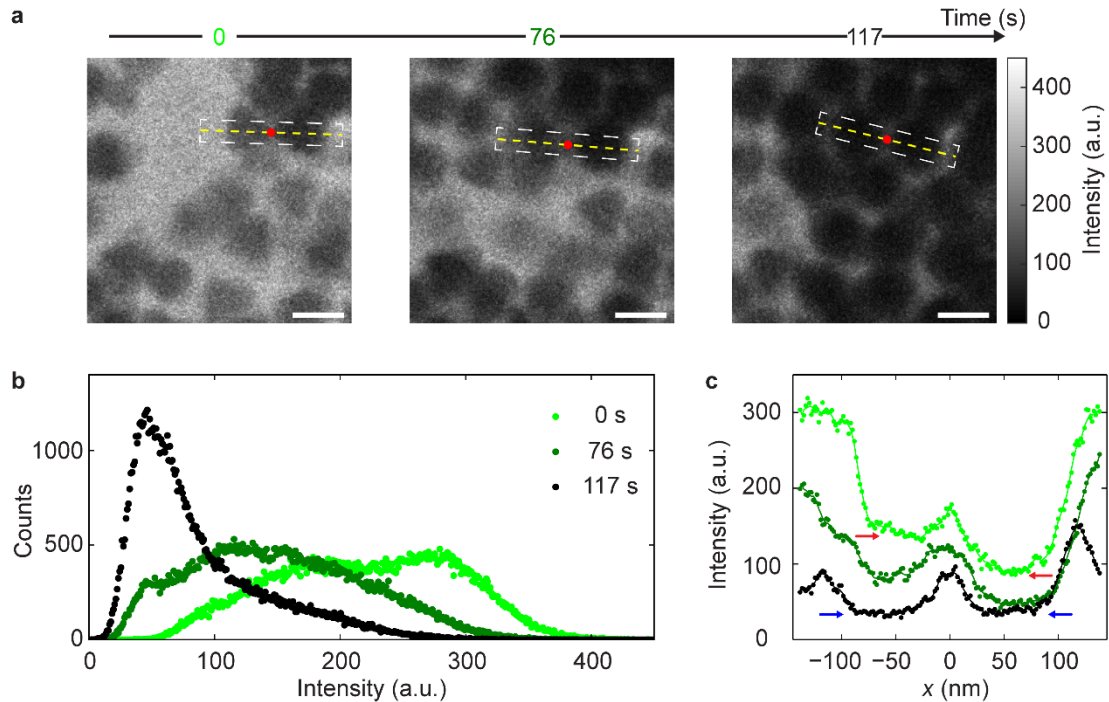
Supplementary Figure 6. Vertical growth of columns from prism stacking. (a) Time-lapse TEM images showing the gradual building process of columns acquired at 0 s (light green), 76 s (green) and 117 s (black). The projections of the columns change from triangular to circular shapes as time goes by. Scale bars: 100 nm. (b) Distribution of intensity values of the TEM images in (a). The peak position of the intensity distribution shifts to lower values and the distribution narrows to a sharp peak as time goes by, indicating the formation of thicker columns. (c) Intensity profile along the yellow dashed line, with the red dot in (a) denoting $x = 0$. The intensity is averaged over the boxed region in (a) and reflects the gradual stacking of prisms onto existing columns. The three intensity profiles across the same two columns show the data from the beginning to the fully grown columns. The initially different intensity plateaus (red arrows) reflect different numbers of prisms in the columns, whereas the two columns have the same intensities (blue arrows) after 117 s.
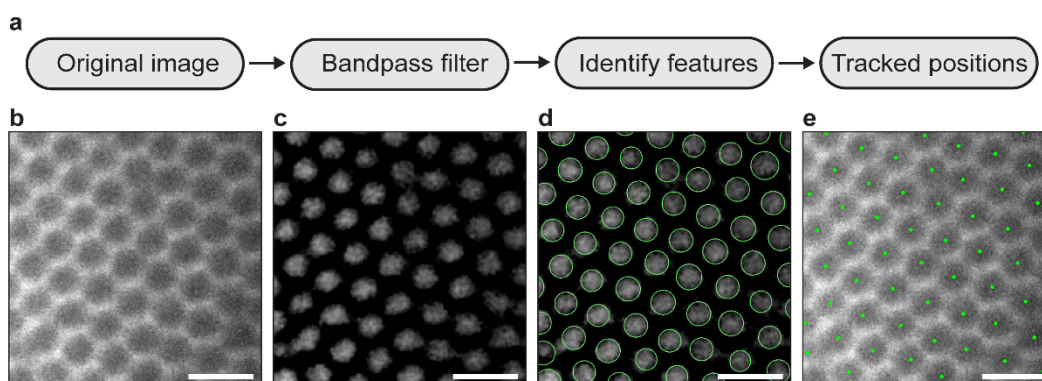
Supplementary Figure 7. Tracking of single columns in liquid-phase TEM movies. (a) Column-tracking workflow from the original TEM image to the final image with overlaid tracked positions. (b) Typical raw TEM image of Supplementary Video 4, showing an ordered lattice composed of circular column projections. (c) The same image with inverted intensity (to render the columns bright for tracking) and enhanced contrast after bandpass filtering. Compared with the raw image in (b), the background of the image is more uniform and the column shapes are more distinguishable from the background. (d) Automatic detection of column contours by positioning fitted circles. (e) The same raw TEM image as in (b) overlaid with the centres (green dots) of the circles identified in (d). The column position information was used for further structural and phase characterisation in Supplementary Notes 6.3–6.6. Scale bars: 200 nm.

a

b Fraction vs Center-to-center distance r (nm)

c Hexagonal lattice — 115.5 nm

d Honeycomb lattice — 57.7 nm

Supplementary Figure 8. Measurement of centre-to-centre distance r of two nearest-neighbour columns and comparison with perfect hexagonal and honeycomb lattices. (a) Typical TEM snapshot of an ordered hexagonal lattice formed by columns. Green dots and white dotted lines highlight the central positions of columns and the bond network, respectively. Scale bar: 200 nm. (b) Histogram of the centre-to-centre distance between pairs of neighbouring columns measured from (a). The red line is a Gaussian fit of the histogram and the inset is a schematic showing the definition of the centre-to-centre distance r for neighbouring columns. (c) Schematic of the hexagonal lattice composed of columns stacked from randomly oriented prisms. (d) Schematic of the possible honeycomb lattice from columns of aligned prisms.

44
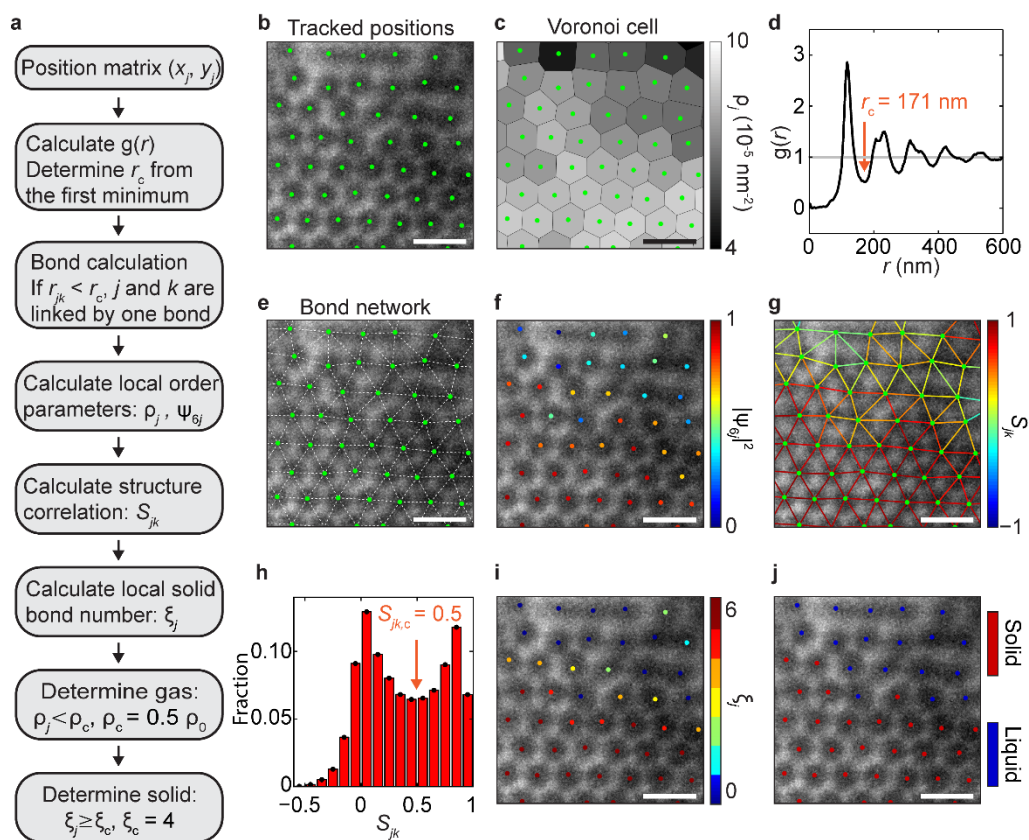
Supplementary Figure 9. Illustration of the image processing and analysis procedure of a typical TEM image of Supplementary Video 6 to classify columns into different states. (a) Analysis workflow from tracked column positions to column state determination. (b) Column positions (green dots) from particle tracking (method detailed in Supplementary Note 6.2) overlaid on the original TEM image. (c) Voronoi cells calculated from the particle positions. Each cell is shaded according to the local density ρ_j. (d) Radial distribution function $g(r)$ calculated from the column positions in Supplementary Video 6 over the full crystallisation process. A cutoff value r_c = 171 nm was determined from the first minimum after the first peak position (orange arrow). This cutoff value is used to decide if two columns are nearest neighbours. (e) Bond network rendered based on panels (b) and (d). (f) TEM image overlaid with dots at the column centres coloured according to the values of local order parameter $|\psi_{6j}|^2$. (g) TEM image overlaid with bond network coloured by the value of S_{ij}, which characterises structural similarity between neighbouring columns. (h) Distribution of S_{ij} for columns during crystallisation (Supplementary Video 6). Based upon the double-peaked distribution, a cutoff value $S_{ij,c}$ = 0.5 is chosen for the calculation of the solid bond number. (i) TEM image overlaid with dots coloured by solid bond number ξ_j. (j) TEM image identifying solid-like (red) and liquid-like columns (blue). Scale bars: 200 nm.
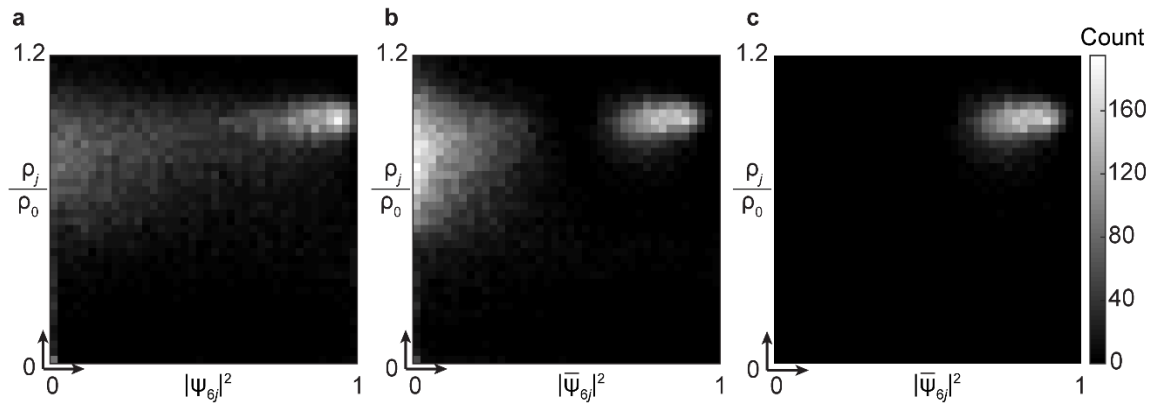
Supplementary Figure 10. 2D histograms of local density and local structural order highlighting the existence of liquid-like and solid-like domains. (a, b) 2D histogram with (a) $|\psi_{6j}|^2$ and (b) coarse-grained order parameter $|\overline{\psi}_{6j}|^2$ to characterise the structural order. The two domains in the 2D histogram are more concentrated for $(|\overline{\psi}_{6j}|^2, \rho_j)$ than for $(|\psi_{6j}|^2, \rho_j)$. (c) 2D histogram based on statistics only from solid-like columns identified based upon the solid bond number, confirming that the identified solid-like columns indeed correspond to the domain with high structural order. All panels employ the same greyscale.
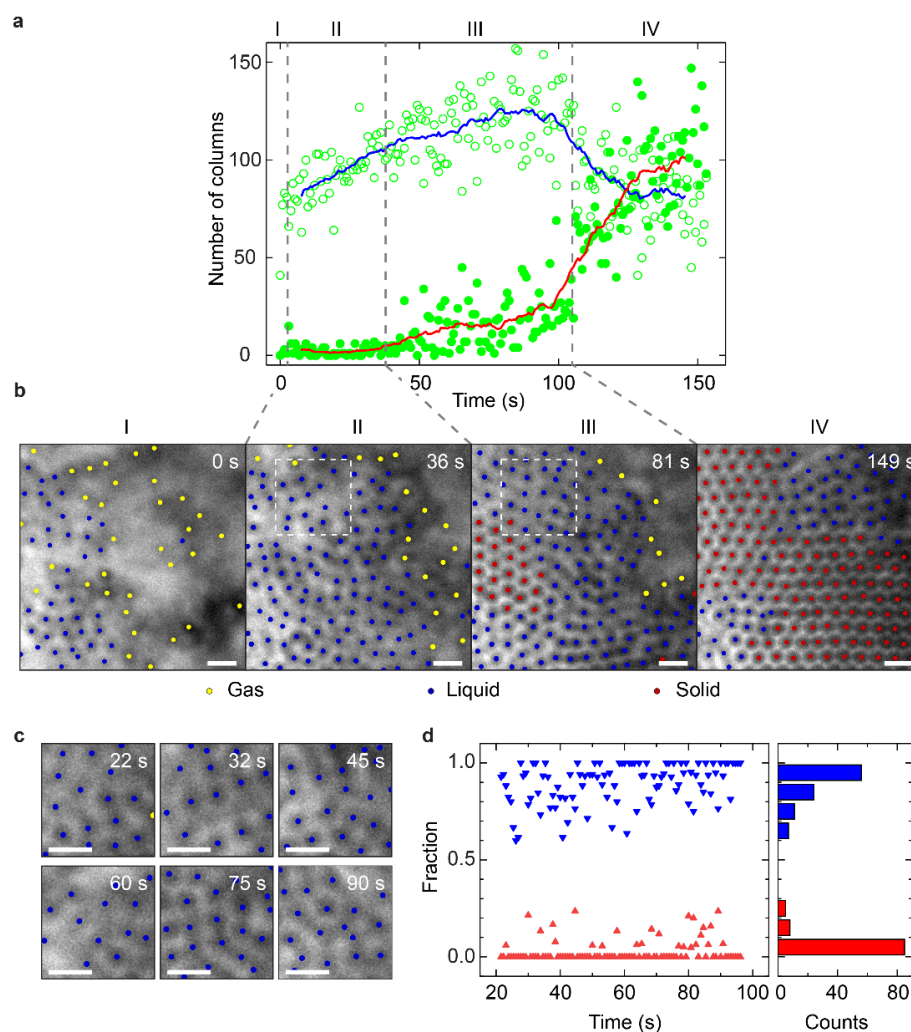
Supplementary Figure 11. Temporal evolution of liquid-like and solid-like columns using Supplementary Video 6 as an example. (a) Number of liquid-like (N_{liquid}, open green circles) and solid-like columns (N_{solid}, solid green circles) as a function of time. Solid lines show the numbers of liquid-like (blue) and solid-like (red) columns averaged over 21 neighbouring frames. (b) Time-lapse TEM images showing different stages of the crystallisation process. The tracked columns are overlaid with dots that are coloured based on their states: gas-like (yellow), liquid-like (blue) and solid-like (red). Initially (pre-nucleation, stage I), most columns are gas-like. At the induction stage (II), a large liquid-like domain begins to form without any solid-like columns. At the conversion stage (III), rapidly fluctuating domains of solid-like columns appear inside the liquid-like domains. Lastly (stage IV), solid-like columns form domains that grow rapidly and convert most of the view into the crystalline structure. (c) Zoomed-in time-lapse TEM images for the white boxed region in (b) with dots coloured based on their states. (d) Temporal evolution of the fraction of liquid (blue) and solid (red) columns inside the boxed region in (b) before a stable solid nucleus emerges. Right panel: accumulated distribution over time. Scale bars in panels (b) and (c): 200 nm.

47
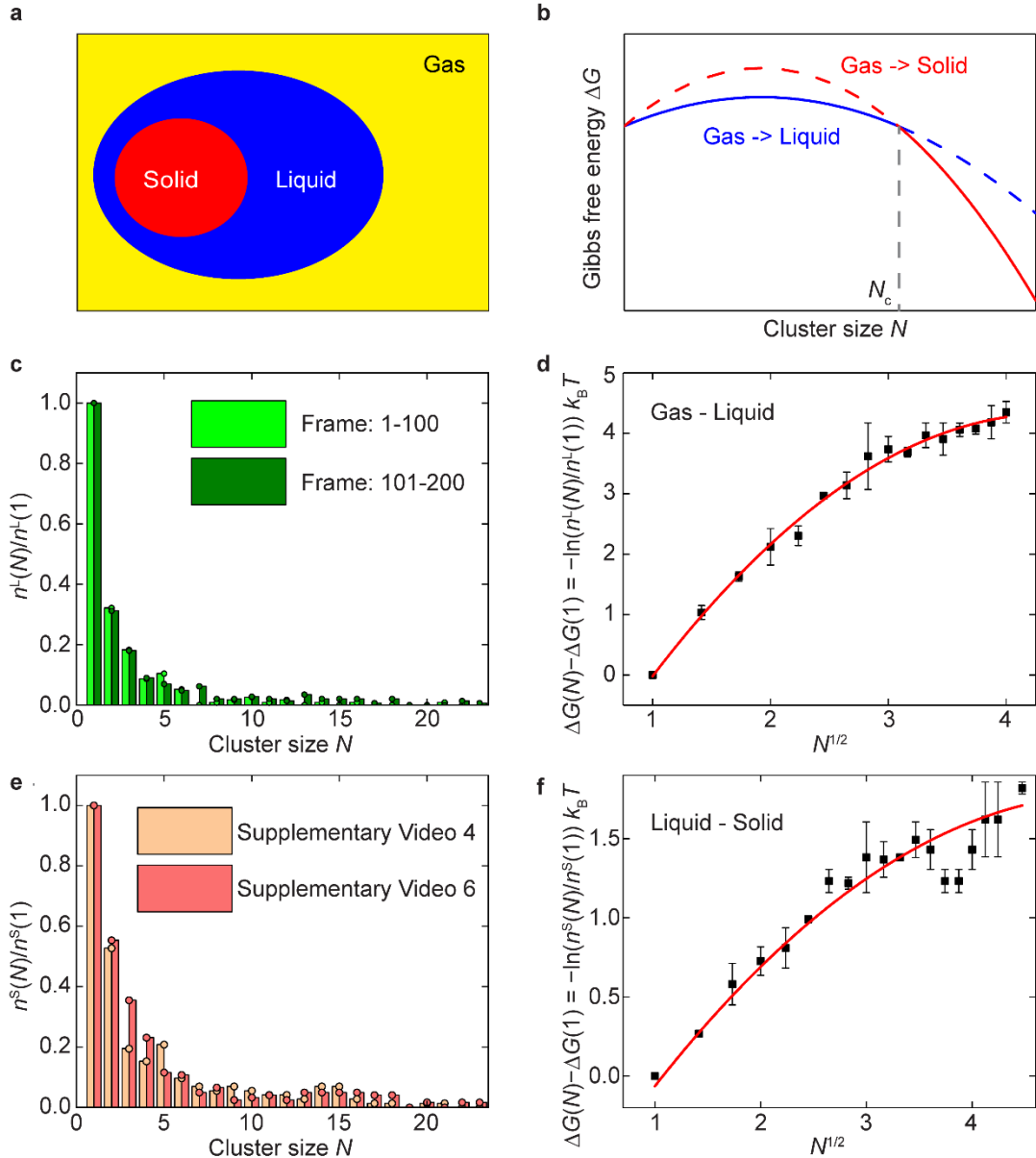
Supplementary Figure 12. Two-barrier Gibbs free-energy model to explain two-step crystallisation. Measurement of line tension between the gas–liquid and liquid–solid column interfaces. (a) Schematic illustrating that the amorphous, liquid intermediate state emerges between the gas and the solid states as an effective a wetting layer, cf. TEM images in Figures 2g–i and Figure 3d (main text). (b) Schematic plot of the free-energy change ΔG for the gas–solid and gas–liquid transitions, as a function of cluster size N. The crossover between the two curves, at a critical cluster size N_c, occurs as the gas–solid interface has a higher line tension than the gas–liquid interface owing to the larger structural difference, whereas the chemical potential of the solid state is lower than that of liquid state at the experimental conditions that favours crystallisation. (c) Distribution of the liquid cluster sizes N (measured in number of columns),

48

obtained from Supplementary Video 6. The vertical axis is the number of liquid clusters with N columns, $n^{\mathrm{L}}(N)$, normalised by the number of liquid clusters with only one column $n^{\mathrm{L}}(1)$. (d) Free-energy difference for the gas–liquid transition ΔG is measured based on the distribution of liquid-like cluster sizes by accumulating all the clusters in Supplementary Videos 4 and 6. The red line is a parabolic fit of the-free energy difference, from which the line tension and chemical potential difference of the liquid-gas formation process are acquired. (e) Distribution of the solid cluster sizes N (measured in number of columns) inside a liquid cluster, obtained from the crystallisation process of Supplementary Videos 4 and 6. The vertical axis is the number of solid clusters with N columns, $n^{\mathrm{S}}(N)$, normalised by the number of solid cluster with only one column $n^{\mathrm{S}}(1)$. (f) Free-energy difference for the liquid-solid transition ΔG is measured from the distribution of solid-like cluster sizes by accumulating all clusters in Supplementary Videos 4 and 6. The red line is a parabolic fit of the-free energy difference. The uncertainties in (d) and (f) are estimated as the standard errors from two different experiments.
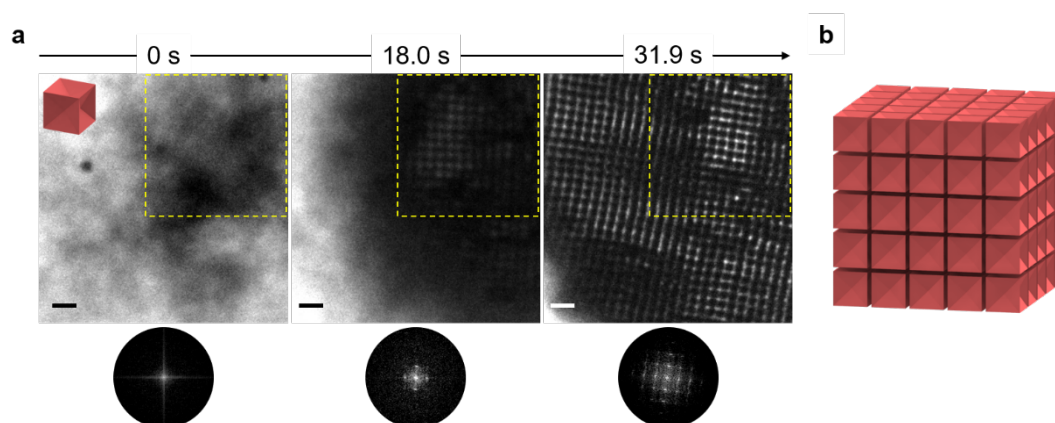
Supplementary Figure 13. Superlattice formation of gold concave nanocubes. (a) Time-lapse liquid-phase TEM images showing the crystallisation of fast-moving individual concave nanocubes (dark "clouds") into ordered 3D simple cubic superlattices at 27.1 e$^-$·Å^{-2}·s^{-1}. The bottom images are the corresponding Fourier transforms of the boxed region in (a). (b) Schematic of the simple cubic superlattice of concave nanocubes. Scale bars: 200 nm.
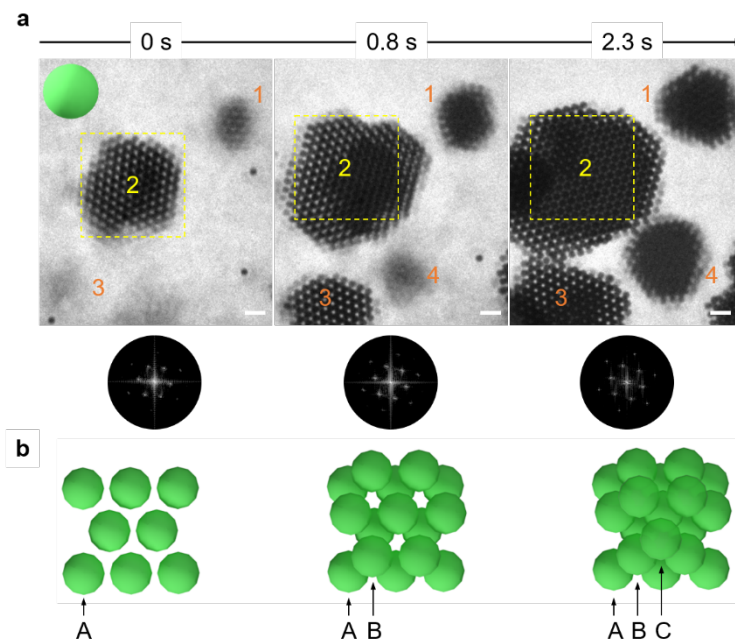
Supplementary Figure 14. Superlattice formation of gold nanospheres. (a) Time-lapse liquid-phase TEM images showing the real-time nanosphere crystallisation process observed at $11.9\ \mathrm{e^-\cdot Å^{-2}\cdot s^{-1}}$, with 1, 2, 3 and 4 labelling four superlattice domains. The bottom images are the corresponding Fourier transforms of the boxed region in (a). (b) Schematics of the ABC layered face-centred cubic lattice (top view) from nanospheres. Scale bars: 200 nm.
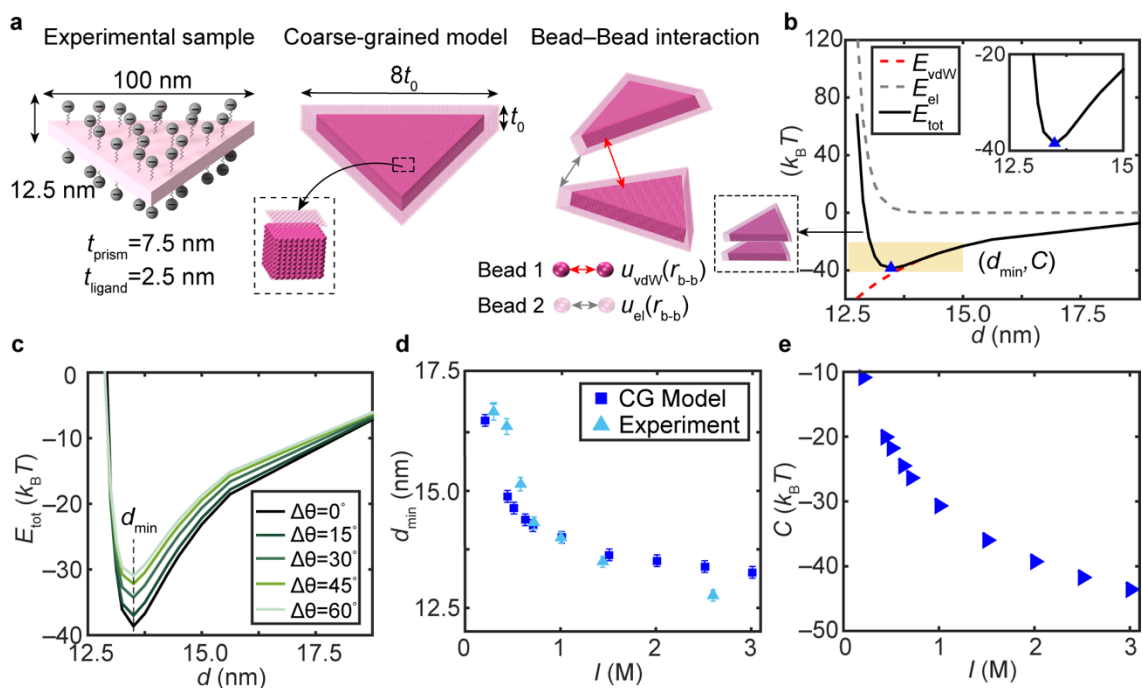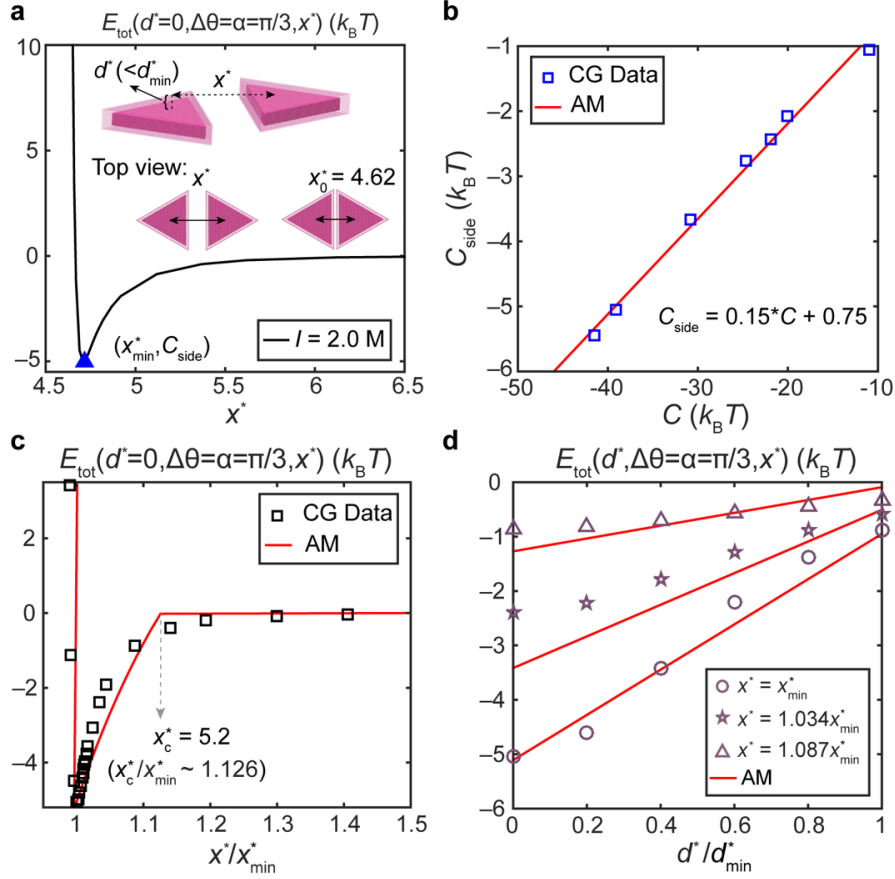
Supplementary Figure 15. CG model for prism–prism pairwise interactions and model validation. (a) Schematic depiction of the CG model consisting of 252,540 type-1 beads (dark pink beads) to model the gold triangular prism and 54,402 type-2 beads (light pink beads) forming the ligand monolayer shell to model the charged ligands. Type-1 bead have a van der Waals interaction $u_{vdW}(r_{b-b})$ and type-2 beads have a screened Coulomb interaction $u_{el}(r_{b-b})$ (see Eqs. S1 and S2 for expressions for $u_{vdW}(r_{b-b})$ and $u_{el}(r_{b-b})$). The pairwise interaction between two prisms is computed as a summation over all bead–bead interactions. The total thickness of the CG prism including two monolayers of ligands is denoted as t_0. (b) Van der Waals interaction E_{vdW} (Eq. S6, dashed red line), electrostatic interaction E_{el} (Eq. S7, dashed grey line) and the total pairwise energy E_{tot} (solid black line) between two coaxial parallel and aligned ($\Delta\theta = 0$) prisms (as shown in the lower left schematic) versus the prism–prism separation d at ionic strength $I = 2.0$ M, computed in the CG model. The minimum total interaction energy C (at corresponding separation d_{min}) is marked with a blue triangle. The inset shows a magnified view of the shaded part of the $E_{tot}-d$ curve to highlight the deep and narrow potential well. The definitions of d and $\Delta\theta$ are shown in Figure 2a in the main text. (c) Total pairwise interaction energy E_{tot} for two coaxial parallel prisms as a function of vertical separation d at different values of relative spin angle $\Delta\theta$. The minimum-energy separation d_{min} is independent of $\Delta\theta$. (d) Minimum-energy separation d_{min} versus ionic strength I computed in the CG model (dark blue squares) and prism spacings measured in our previous experiments[1] (light blue triangles), validating the CG model. (e) Minimum energy C between two coaxial parallel prisms as a function of ionic strength I computed in the CG model.
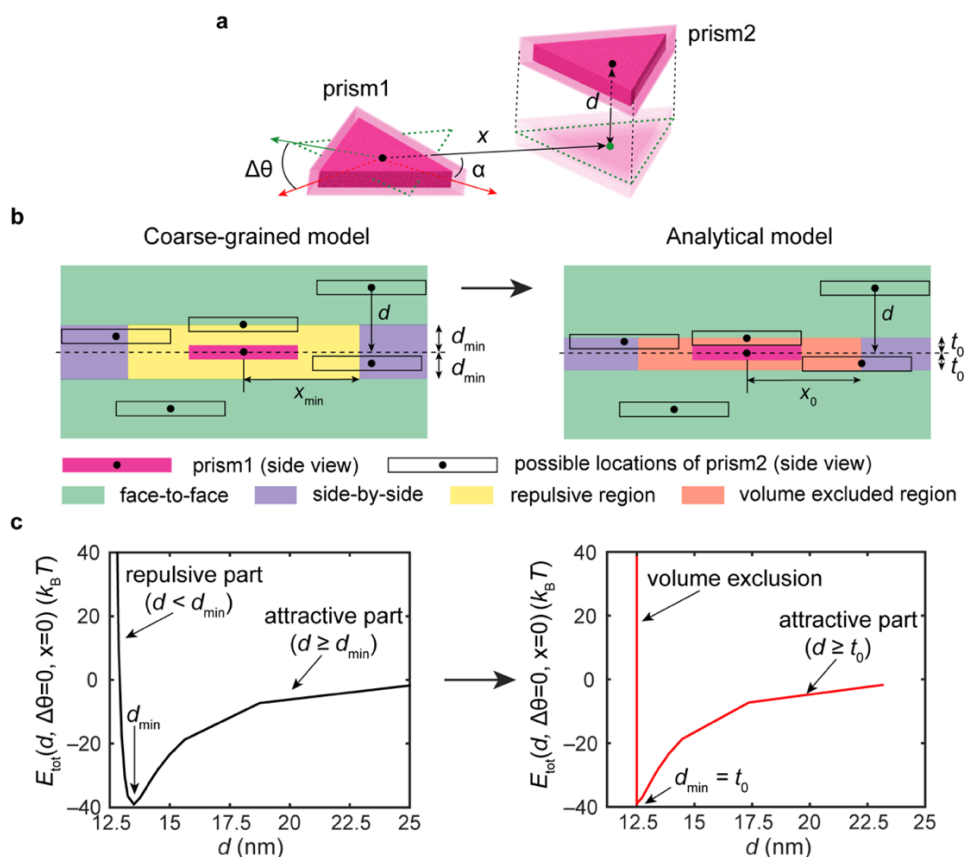
Supplementary Figure 16. Connection between the CG model and the analytical model; classification of configurations. (a) Schematic showing the definition of the four degrees of freedom for a pair of parallel prisms (prism1, which is the central prism, and prism2) employed in the analytical model: the vertical separation d, spin-angle difference $\Delta\theta$, horizontal displacement magnitude x and direction angle α. The black dots stand for the geometric centres of prism1 and prism2, while the green dot denotes the projected centre of prism2 on the basal plane of prism1. (b) Side-view schematic showing different interaction regions (repulsive, face-to-face attractive, side-by-side attractive and excluded-volume regions) around the central prism (prism1) in the CG model (left) and the analytical model (right). Due to its short-range character, we choose to replace the repulsive part of the prism–prism interaction in the CG model (yellow region) by the excluded-volume repulsion of the prisms in the analytical model (orange region), whereas the attractive part of the interaction (green plus purple regions in left panel) in the CG model is fitted by analytical functions in the analytical model. The configuration of two parallel prisms (prism1 and prism2) is classified as face-to-face (side-by-side) if the centre of prism2 is located in the green (purple) region. (c) Total interaction energy E_{tot} between two parallel, coaxial ($x = 0$) and fully aligned ($\Delta\theta = 0$) prisms *vs.* their vertical separation d at $I = 2.0$ M in the CG model (left) and the analytical model (right). Note that the minimum-energy separation d_{min} in the analytical model becomes exactly t_0 regardless of the ionic strength.
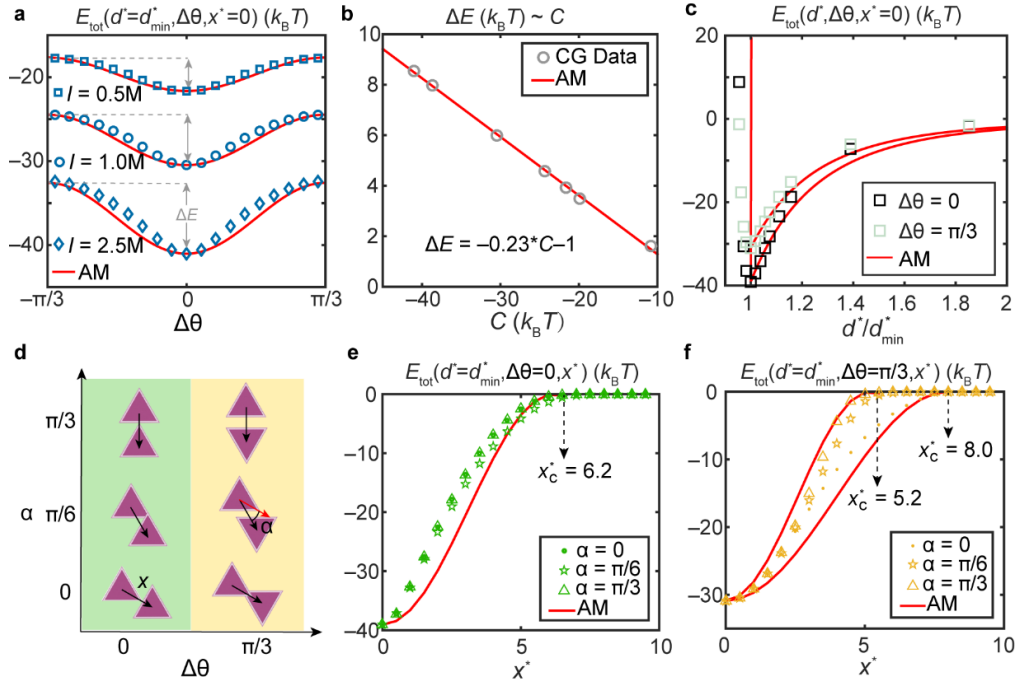
Supplementary Figure 17. Derivation of analytical form of the attractive part of the total interaction energy E_{tot} for a pair of face-to-face parallel prisms (cf. Supplementary Figure 16b for the definition of face-to-face configuration). (a) Pairwise interaction energy E_{tot} between two coaxial ($x = 0$) parallel prisms at the minimum-energy separation $d^* = d^*_{min}$ as a function of the spin-angle difference $\Delta\theta$ at three different ionic strengths ($I = 0.5, 1.0, 2.5$ M). Blue symbols are the data computed using the CG model, fitted by the analytical model $E_{tot}(d^* = d^*_{min}, \Delta\theta, x^* = 0) = C + (1 - \cos 3\Delta\theta)\Delta E/2$ (solid red lines, labelled AM). The energy difference ΔE between the anti-aligned ($\Delta\theta = \pi/3$) and aligned ($\Delta\theta = 0$) cases is labelled in the plot. (b) ΔE *vs.* coupling constant C determined from the CG model (grey circles) and fitted by a linear function in the analytical model (solid red line). (c) Pairwise interaction energy E_{tot} between two coaxial parallel prisms as a function of d^*/d^*_{min} for $\Delta\theta = 0$ (black squares) and $\Delta\theta = \pi/3$ (light green squares). The data from the CG model (squares) are well fitted by the analytical model $E_{tot}(d^*, \Delta\theta, x^* = 0) = E_{tot}(d^* = d^*_{min}, \Delta\theta, x^* = 0) \cdot (d^*_{min}/d^*)^4$ for $d^* \geq d^*_{min}$, accounting for the attractive part, combined with excluded-volume repulsion $E_{tot}(d^* < d^*_{min}) = +\infty$ (solid red lines). (d) Schematic showing the six combinations of $(\alpha, \Delta\theta)$ considered for fitting the dependence of the interaction energy on horizontal displacement, with either $\Delta\theta = 0$ (green column, fits shown in panel e) or $\Delta\theta = \pi/3$ (yellow column, fits shown in panel f). For both cases, we examine $\alpha = 0, \pi/6$ and $\pi/3$. (e, f) Pairwise interaction energy E_{tot} between two parallel prisms at the minimum-energy separation $d^* = d^*_{min}$ as a function of x^* for $\alpha = 0$ (dot), $\alpha = \pi/6$ (star) and $\alpha = \pi/3$ (triangle) at (e) $\Delta\theta = 0$ and (f) $\Delta\theta = \pi/3$, at ionic strength $I = 2.0$ M. The data computed using the CG model (symbols) are well fitted by $E_{tot}(d^*, \Delta\theta, x^*) = E_{tot}(d^*, \Delta\theta, x^* = 0)(1 + \cos(\pi x^*/x^*_c))/2$ for $x^* < x^*_c$ used in the analytical model (solid red lines), where x^*_c (which depends on $\Delta\theta$ and α) is the cutoff distance beyond which $E_{tot}(d^*, \Delta\theta, x^* > x^*_c) = 0$.

Supplementary Figure 18. Attractive part of pairwise interaction energy E_{tot} in the analytical model for a pair of parallel prisms in side-by-side configuration (cf. Supplementary Figure 16b). (a) Pairwise interaction energy E_{tot} between two parallel prisms arranged in side-by-side fashion ($\Delta\theta = \alpha = \pi/3$) with zero vertical separation ($d^* = 0$), as a function of horizontal displacement magnitude x^* computed using the CG model at ionic strength $I = 2.0$ M. The equilibrium distance x^*_{min} and side-by-side interaction energy minimum C_{side} are identified in the plot. Inset: Schematic of a typical side-by-side configuration of two parallel prisms and definition of x^*_0 denoting the centre-to-centre distance between two fully attached side-by-side prisms. (b) Relationship between the side-by-side energy minimum C_{side} and the coupling constant C measured from the CG model (blue squares), described by a linear fit that we employ in the analytical model (solid red line). (c) Pairwise energy E_{tot} between two side-by-side ($\Delta\theta = \alpha = \pi/3$) parallel prisms with zero vertical separation ($d^* = 0$) as a function of the reduced horizontal displacement x^*/x^*_{min} at $I = 2.0$ M. Black squares are the data from the CG model and the red line is the fit function Eq. S14 combined with the excluded-volume repulsion $E_{\text{tot}}(d^* = 0, \Delta\theta = \alpha = \pi/3, x^* < x^*_{\text{min}}) = +\infty$. (d) Pairwise energy between two side-by-side ($\Delta\theta = \alpha = \pi/3$) parallel prisms as a function of the reduced vertical separation d^*/d^*_{min} at three different values of x^* (x^*_{min}: circle; $1.034x^*_{\text{min}}$: star; $1.087x^*_{\text{min}}$: triangle) at $I = 2.0$ M. Symbols represent the CG model, fitted by the linear function of d^*, Eq. S16 (solid red lines).
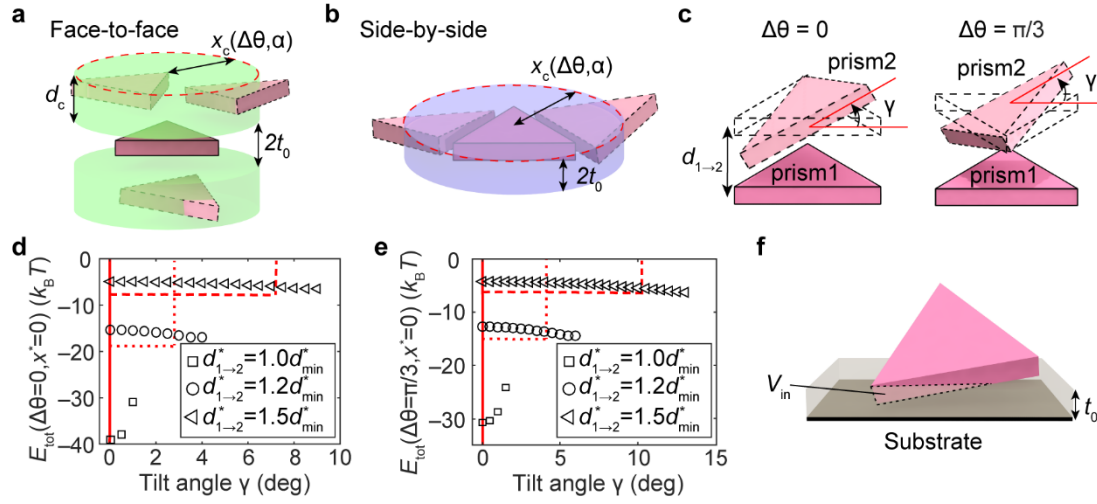
Supplementary Figure 19. Schematic summarising the interaction zone of two interacting prisms and the dependence of interaction energy on tilt angle γ. (a–b) Schematics showing the interaction zone of face-to-face (a) and side-by-side (b) configurations, outside which the pairwise interaction is zero in our analytical model. Here the central prism (prism1, with solid border) interacts with all "almost parallel" (as defined in the text) prisms (prism2, with dashed border) whose centres are located inside the (a) green or (b) purple regions. d_c denotes the cutoff distance for the vertical separation, which we set to $d_c = 3t_0$ for computational efficiency (see more details in Supplementary Note 9.3). Note that the cutoff for the horizontal displacement x_c varies with the angles $\Delta\theta$ and α (see Supplementary Note 9.1.3 for details) and is plotted here as a constant just for visual clarity. (c) Configurations used to examine the effect of tilt angle γ in panels d and e: $\Delta\theta = 0$ (left) and $\Delta\theta = \pi/3$ (right). (d–e) Dependence of pairwise interaction energy E_{tot} on tilt angle γ between two coaxial prisms with spin-angle difference (d) $\Delta\theta = 0$ and (e) $\Delta\theta = \pi/3$ at $I = 2.0$ M. Black symbols are calculated from the CG model and red lines represent the analytical model Eq. S18. Three different vertical separations with respect to prism1 are investigated, $d^*_{1\to2} = d^*_{min}$ (open square, solid line), $d^*_{1\to2} = 1.2d^*_{min}$ (open circle, dotted line) and $d^*_{1\to2} = 1.5d^*_{min}$ (open triangle, dashed line). (f) Schematics of the prism–substrate interaction, showing the overlap volume V_{in} between a prism and the substrate interaction zone.
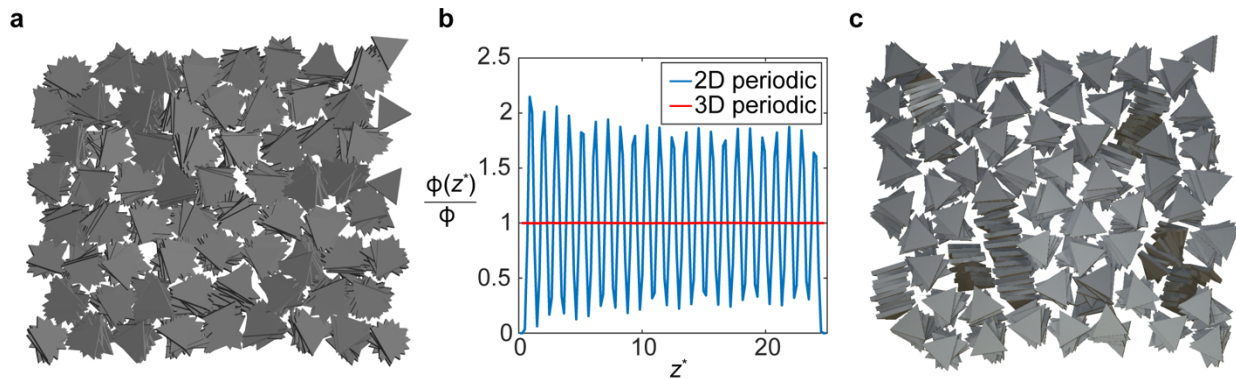
Supplementary Figure 20. The role of confinement along the z axis and the prism–substrate interaction. (a) Snapshot showing the hexagonal columnar phase (with $\left| \Psi_6^{AV} \right|^2 = 0.73$) formed in a 3D periodic system. (b) Volume fraction profile along the z direction, $\phi(z^*)/\phi$, at $I = 0.5$ M, $L_z = 25t_0$ for the 3D periodic system of panel (a) (red line) and for the 2D periodic system (i.e., confined along the z axis by top and bottom surfaces) with $\phi_{2D} = 0.386$. This illustrates how the confinement induces z coordination of prisms in different columns. (c) Snapshot showing a typical configuration in a simulation with confinement along the z axis but in the absence of prism–substrate interaction. The simulation is conducted at $I = 0.5$ M, $L_z = 10t_0$, and $\phi_{2D} = 0.386$. The system starts with 64 columns standing on the substrate, but as time elapses the columns reorient and lie parallel to the substrate.
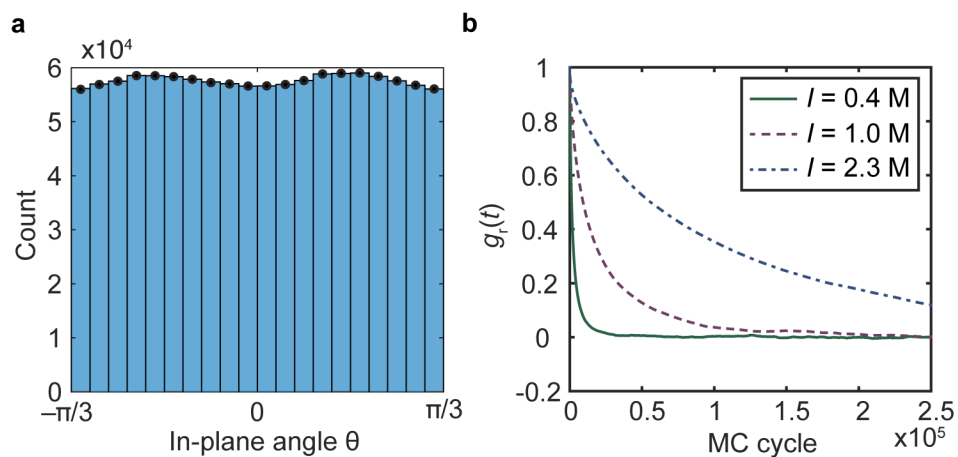
Supplementary Figure 21. In-plane angle distribution and rotational dynamics of the system after reaching equilibrium. (a) Histogram of the in-plane angle θ of each prism measured over the production runs (1000 samples of 1152 prisms). (b) Orientational autocorrelation function $g_r(t)$ at different ionic strengths.
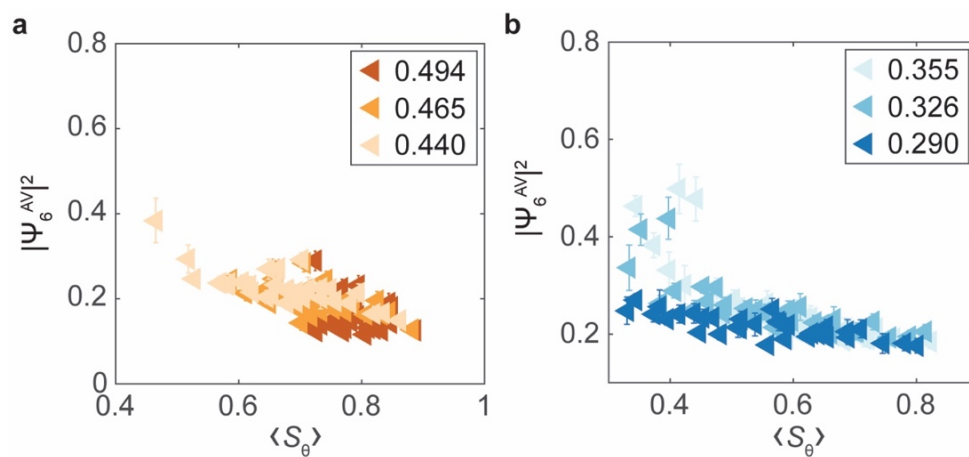
Supplementary Figure 22. Dependence of global 2D hexagonal order on column packing fraction. Correlation between the average global hexagonal order characterised by $\left|\Psi_6^{AV}\right|^2$ and the average columnar orientational order $\langle S_\theta \rangle$ at (a) high and (b) low 2D packing fraction ϕ_{2D}.
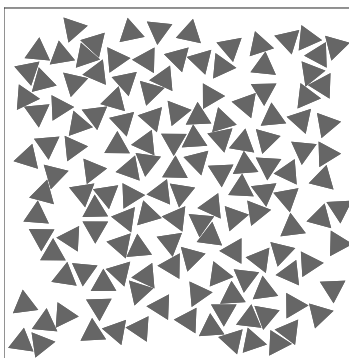
Supplementary Figure 23. Simulation snapshot of a purely 2D nanoprisms system. The system consists of 140 prisms at ionic strength $I = 0.5$ M and 2D packing fraction $\phi_{2D} = 0.386$ and remains in a disordered phase without exhibiting crystallisation.
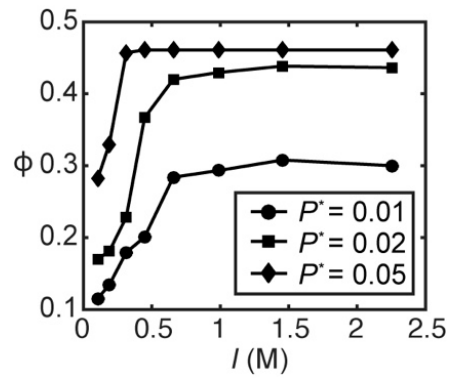
Supplementary Figure 24. Equilibrium prism concentration induced by ionic strength gradient. Equilibrium volume fraction ϕ measured from the *NPT* simulations as a function of the ionic strength I at three different values of the dimensionless pressure P^*. The uncertainties are smaller than the symbol size.
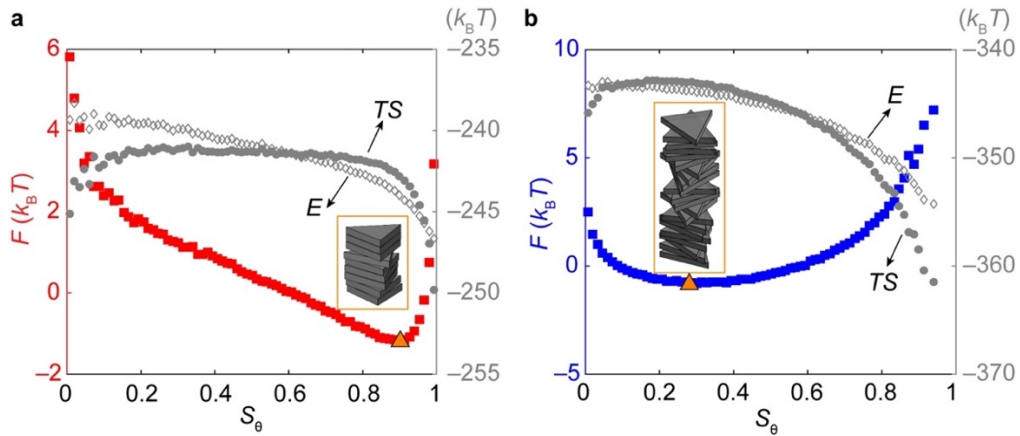
Supplementary Figure 25. Free-energy curve of a single column at the two different conditions discussed in Figure 4b–f (main text). Free energy F (left axis), entropic contribution TS (right axis), and total interaction energy E (right axis) computed from single-column simulations as a function of the column orientational order parameter S_θ at (a) $M = 9$, $L_z^* = 10$, and $I = 3.0$ M, and (b) $M = 23$, $L_z^* = 25$, and $I = 0.5$ M. (Insets) Snapshots of typical configurations at the thermodynamic equilibrium state (orange triangle).
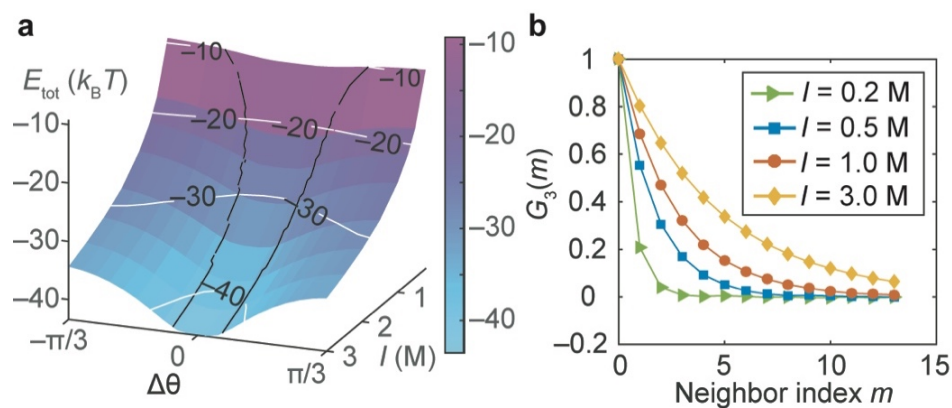
Supplementary Figure 26. Dependence of orientational structure on ionic strength. (a) Total pairwise energy E_{tot} between two parallel and coaxial prisms with minimum-energy separation $d_{\min}$, computed in the CG model and plotted *vs.* $(\Delta\theta, I)$. Black lines mark the $[-\Delta\theta_c, \Delta\theta_c]$ interval upon variation of ionic strength I. (b) Orientational correlation function $G_3(m)$ of an individual column with $M = 27$ and $L_z^* = 30$ at four different ionic strengths.
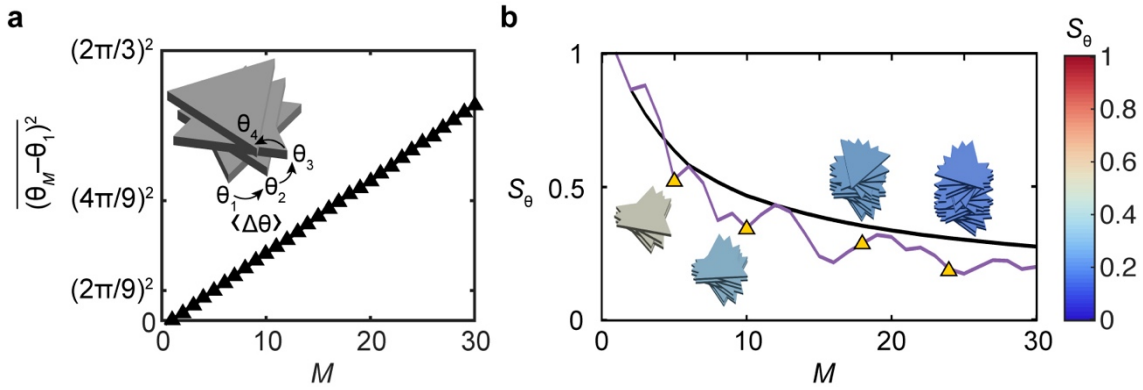
Supplementary Figure 27. Random-walk model illustrating the dependence of orientational order on the number of prisms inside the column M. (a) (Inset) Schematic of the 1D random-walk model in which successive rotations proceed clockwise or counter-clockwise with equal probability. The step size is the pairwise relative orientation $\langle \Delta\theta \rangle$, and the number of steps is the number of prisms M within the column. (Main) Mean squared angular displacement relative to the first prism, $\overline{(\theta_M - \theta_1)^2}$, as a function of M calculated from 1,000,000 random paths, confirming the expected linear relationship. (b) Columnar orientational order S_θ vs. number of constituent prisms M for a representative random walk path (purple line) and the average over 1000,000 random paths (black line). (Inset) Snapshots showing the configurations of the column at $M = 5$, 10, 18 and 24 for the representative path (marked by the yellow triangles). The colour of the four snapshots reflects their orientational order S_θ (cf. colour bar).
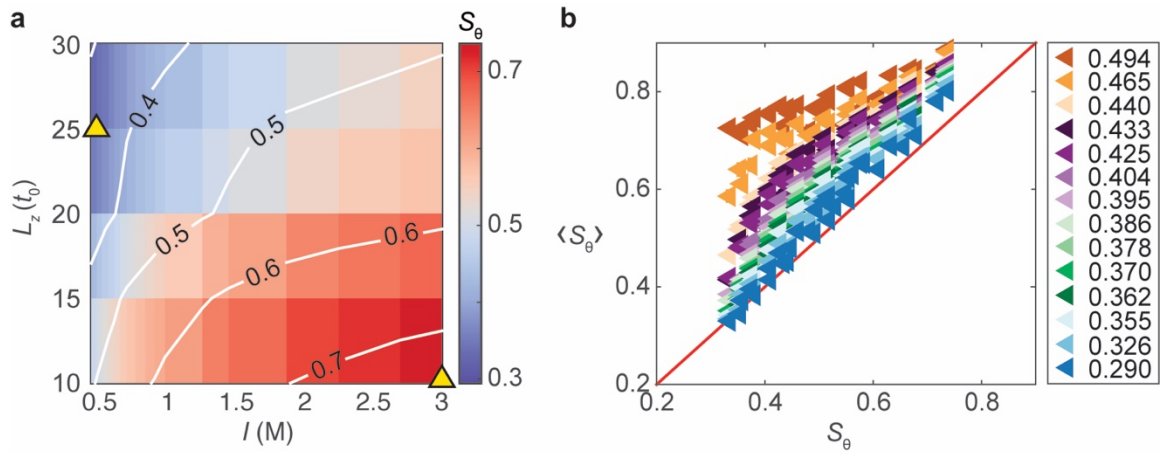
Supplementary Figure 28. Effects of 2D packing fraction and intercolumn interaction on columnar orientational order. (a) Orientational order parameter S_θ from single-column simulations as a function of ionic strength I and cell height L_z (in units of prism thickness t_0). Yellow triangles mark the two conditions used in Figure 4b,d (main text). (b) Scatter plot of average columnar orientational order $\langle S_\theta \rangle$ measured from large-scale simulations *vs.* predicted S_θ in single-column simulations at the same ionic strength and cell height. Symbol colours specify the 2D packing fractions ϕ_{2D} used in the large-scale simulations and each data point corresponds to an (I, L_z) condition listed in Supplementary Table 2.

Supplementary Tables

Supplementary Table 1. Literature Summary on sluggish nanoparticle motions.

Liquid	Liquid chamber	Nanoparticle with radius r noted	Measured particle diffusivity $D_{measure}$ (nm^2/s)	Predicted particle diffusivity* $D_{predict}$ (nm^2/s)	$D_{predict} / D_{measure}$	Ref.
Aqueous buffer	Graphene	2.5 nm Au spheres	1.7	9.8×10^7	5.8×10^7	14
Water-glycerol mixture, 15% glycerol (volume ratio)	Si$_3$N$_4$	2.5 nm Au spheres	0.165	6.0×10^7	3.7×10^8	15
		5 nm Au spheres	0.172	3.0×10^7	1.8×10^8	
		7.5 nm Au spheres	0.268	2.0×10^7	7.5×10^7	
o-dichlorobenzene-oleylamine mixture	Graphene	0.27 nm Pt nanocrystal	1.1	2.0×10^8	1.8×10^8	16
		0.43 nm Pt nanocrystal	0.2	1.2×10^8	6.2×10^8	
		0.55 nm Pt nanocrystal	0.1	9.7×10^7	9.7×10^8	
HAuCl$_4$ aqueous solution	Si$_3$N$_4$	2 nm Au spheres	0.05	1.2×10^8	2.5×10^9	17
Pentadecane, oleylamine, oleic acid mixture	Si$_3$N$_4$	2 nm PtFe$_3$ spheres	0.11	1.74×10^7	1.6×10^8	18
CTAB aqueous solution	Si$_3$N$_4$	18 nm Au octahedron	46-110	1.4×10^7	$1.2\text{-}3.0\times10^5$	19
o-dichlorobenzene-pentadecane mixture	Si$_3$N$_4$	3.7 nm Pt spheres	~40	1.4×10^7	3.6×10^5	20
Water	Si$_3$N$_4$	6 nm Au spheres	15	4.1×10^7	2.7×10^6	21
Aqueous buffer	**Si$_3$N$_4$**	**Columns stacked from Au triangular nanoprisms**	**~2470**	**1.7×10^6**	**6.9×10^2**	**This liquid-phase TEM work****

*The predicted diffusivity is calculated from $D_{predict} = \frac{k_B T}{6\pi\eta r}$, where T is the temperature and η is the viscosity of the liquid.

**The predicted diffusivity is calculated using the column height estimated from simulation (23 prisms inside one column).

Supplementary Table 2. Literature survey on dose rate dependent electron beam effects in SiN_x chambered liquid-phase TEM.

Sample	Observation	Dose rate ($e^- \cdot Å^{-2} \cdot s^{-1}$)	Ref.
Rotavirus particle	In situ imaging of virus	< 0.1	27
Glioblastoma cell, Au nanorod	Visualisation of cell and interaction with Au nanorod	< 0.5	28
Cupriavidus metallidurans cells	Visualisation of cells	0.5	29
DNA-Au nanoparticle	Nanoparticle assembly *via* DNA base paring	~1.1	30
Pt electrode	Redox potential shift in cyclic voltammogram	1	31[a]
Au triangular nanoprisms	Assembly of Au triangular nanoprisms	1–6 (assembly) 3400 (nanoparticle fusion)	1
Au nanorods	Assembly of Au nanorods	10–15	44
CTAB-Au nanospheres, nanocubes, nanorods and nanobipyramids	Assembly of Au nanoparticles	10–20	45
Au triangular nanoprisms	Assembly of Au triangular nanoprisms	10–40	4
Au nanoparticles	Aggregation and dynamics of Au nanoparticles	40 (motion) 90 (motion)	21
Au nanosphere	Assembly of Au nanospheres	63.5–67.3	46[b]
$HAuCl_4$	Growth of Au nanocrystals	< 30 (no growth) 42 (growth)	32
Au nanoparticles	Growth of amorphous Au structures onto Au nanoparticles	46	33
$AgNO_3$	Growth of Ag nanoparticles	140	47
$HAuCl_4$, Pt nanoparticle	Growth of Au shell on Pt nanoparticle	< 30 (no growth) 300 (growth) 1500 (dendritic growth)	34
citrate-Au nanoparticle	Fusion of Au nanoparticles	370 (no fusion) 750 (fusion)	48
Bismuth neodecanoate	Growth and coalescence of Bi nanoparticle	500 (growth)	49[b]
$Pb(acac)_2$, $Fe(acac)_2$	Growth of lead-iron hydroxide core-shell nanoparticle	500 (growth) 1000 (bubble formation) 1500 (nanoparticle deformation)	50[b]
K_2PtCl_4, EDTA	Growth and assembly of Pt nanoparticles	1000–3000	51
$HAuCl_4$	Growth and coalescence of Au nanocrystals	1675–1836	35
$Pt(acac)_2$	Pt nanocrystal growth	1300–8700	52[b]
$HAuCl_4$, CTAB	Dynamics and aggregation of Au nanoparticles	1480–16000 (fusion)	53
$HAuCl_4$, citrate acid	Growth of Au nanospheres	6250	36
$HAuCl_4$, CTAB	Fusion between Au nanoparticles	5000–20000	54

Acetylacetonate is abbreviated as acac.
[a]An electrochemical setup was used. [b]Organic solvents were used.

Supplementary Table 3. Parameters used in image processing and contour finding in Supplementary Figure 5.

Parameters	Image size* (pixels)	Background subtraction	Low-pass filter threshold	Intensity threshold	Smoothing factor
For Supplementary Figure 3b: 1 pixel is 2.1 nm	67×67	Shape: disk Size: 50 pixels	0.12 pixel^{-1}	15900	9
For Supplementary Figure 3c: 1 pixel is 1.4 nm	247×247	Shape: disk Size: 30 pixels	0.04 pixel^{-1}	11000	15

* The original image used for identifying the contour in Supplementary Figure 5b is the output image in Supplementary Figure 5a (101×101 pixels).

Supplementary Table 4. Parameters used in the large-scale Monte Carlo simulations.

Parameter 1	I (M)	0.44	0.52	0.65	0.76	0.98	1.44	2.25	3.00
	C ($k_\mathrm{B}T$)	−20	−22	−25	−27	−30	−35	−40	−43

Parameter 2	L_z (t_0)	10		15		20		25	
	M	9		14		18		23	
	M_tot	576		896		1152		1472	

Parameter 3	L_x (t_0)	64.4	66.4	68.2	68.8	69.4	71.2	72.0
		72.8	73.6	74.4	75.2	76.0	79.2	84.0
	Φ_2D	0.494	0.465	0.440	0.433	0.425	0.404	0.395
		0.386	0.378	0.370	0.362	0.355	0.327	0.290

Supplementary References

1. Kim, J., Jones, M. R., Ou, Z. & Chen, Q. In situ electron microscopy imaging and quantitative structural modulation of nanoparticle superlattices. *ACS Nano* **10**, 9801–9808 (2016).

2. Jones, M. R. & Mirkin, C. A. Bypassing the limitations of classical chemical purification with DNA-programmable nanoparticle recrystallization. *Angew. Chem. Int. Ed.* **52**, 2886–2891 (2013).

3. O'Brien, M. N., Jones, M. R., Kohlstedt, K. L., Schatz, G. C. & Mirkin, C. A. Uniform circular disks with synthetically tailorable diameters: two-dimensional nanoparticles for plasmonics. *Nano Lett.* **15**, 1012–1017 (2015).

4. Kim, J., Ou, Z., Jones, M. R., Song, X. & Chen, Q. Imaging the polymerization of multivalent nanoparticles in solution. *Nat. Commun.* **8**, 761 (2017).

5. Millstone, J. E., Park, S., Shuford, K. L., Qin, L., Schatz, G. C. & Mirkin, C. A. Observation of a quadrupole plasmon mode for a colloidal solution of gold nanoprisms. *J. Am. Chem. Soc.* **127**, 5312–5313 (2005).

6. O'Brien, M. N., Jones, M. R., Brown, K. A. & Mirkin, C. A. Universal noble metal nanoparticle seeds realized through iterative reductive growth and oxidative dissolution reactions. *J. Am. Chem. Soc.* **136**, 7603–7606 (2014).

7. Nikoobakht, B. & El-Sayed, M. A. Preparation and growth mechanism of gold nanorods (NRs) using seed-mediated growth method. *Chem. Mater.* **15**, 1957–1962 (2003).

8. Jones, M. R., Macfarlane, R. J., Prigodich, A. E., Patel, P. C. & Mirkin, C. A. Nanoparticle shape anisotropy dictates the collective behavior of surface-bound ligands. *J. Am. Chem. Soc.* **133**, 18865–18869 (2011).

9. Chen, Q., Cho, H., Manthiram, K., Yoshida, M., Ye, X. & Alivisatos, A. P. Interaction potentials of anisotropic nanocrystals from the trajectory sampling of particle motion using in situ liquid phase transmission electron microscopy. *ACS Cent. Sci.* **1**, 33–39 (2015).

10. Ross, F. M. Opportunities and challenges in liquid cell electron microscopy. *Science* **350**, aaa9886 (2015).

11. Thorneywork, A. L., Aarts, D. G., Horbach, J. & Dullens, R. P. Self-diffusion in two-dimensional binary colloidal hard-sphere fluids. *Phys. Rev. E* **95**, 012614 (2017).

12. Verberg, R., de Schepper, I. M. & Cohen, E. G. D. Viscosity of colloidal suspensions. *Phys. Rev. E* **55**, 3143–3158 (1997).

13. Crocker, J. C. & Grier, D. G. Methods of digital video microscopy for colloidal studies. *J. Colloid Interface Sci.* **179**, 298–310 (1996).

14. Chen, Q., Smith, J. M., Park, J., Kim, K., Ho, D., Rasool, H. I., Zettl, A. & Alivisatos, A. P. 3D motion of DNA-Au nanoconjugates in graphene liquid cell electron microscopy. *Nano Lett.* **13**, 4556–4561 (2013).

15. Zheng, H., Claridge, S. A., Minor, A. M., Alivisatos, A. P. & Dahmen, U. Nanocrystal diffusion in a liquid thin film observed by in situ transmission electron microscopy. *Nano Lett.* **9**, 2460–2465 (2009).

16. Yuk, J. M., Park, J., Ercius, P., Kim, K., Hellebusch, D. J., Crommie, M. F., Lee, J. Y., Zettl, A. & Alivisatos, A. P. High-Resolution EM of Colloidal Nanocrystal Growth Using Graphene Liquid Cells. *Science* **336**, 61–64 (2012).

17.	Lu, J., Aabdin, Z., Loh, N. D., Bhattacharya, D. & Mirsaidov, U. Nanoparticle dynamics in a nanodroplet. *Nano Lett.* **14**, 2111–2115 (2014).

18.	Powers, A. S., Liao, H.-G., Raja, S. N., Bronstein, N. D., Alivisatos, A. P. & Zheng, H. Tracking nanoparticle diffusion and interaction during self-assembly in a liquid cell. *Nano Lett.* **17**, 15–20 (2017).

19.	Li, C., Chen, X., Liu, H., Fang, J. & Zhou, X. In-situ liquid-cell TEM study of radial flow-guided motion of octahedral Au nanoparticles and nanoparticle clusters. *Nano Res.* **11**, 4697–4707 (2018).

20.	Lee, W. C., Kim, B. H., Choi, S., Takeuchi, S. & Park, J. Liquid cell electron microscopy of nanoparticle self-assembly driven by solvent drying. *J. Phys. Chem. Lett.* **8**, 647–654 (2017).

21.	Tian, X., Zheng, H. & Mirsaidov, U. Aggregation dynamics of nanoparticles at solid–liquid interfaces. *Nanoscale* **9**, 10044–10050 (2017).

22.	Walker, D. A., Browne, K. P., Kowalczyk, B. & Grzybowski, B. A. Self-assembly of nanotriangle superlattices facilitated by repulsive electrostatic interactions. *Angew. Chem. Int. Ed.* **49**, 6760–6763 (2010).

23.	Schneider, N. M., Norton, M. M., Mendel, B. J., Grogan, J. M., Ross, F. M. & Bau, H. H. Electron–water interactions and implications for liquid cell electron microscopy. *J. Phys. Chem. C* **118**, 22373–22382 (2014).

24.	Woehl, T. J., Jungjohann, K. L., Evans, J. E., Arslan, I., Ristenpart, W. D. & Browning, N. D. Experimental procedures to mitigate electron beam induced artifacts during in situ fluid imaging of nanomaterials. *Ultramicroscopy* **127**, 53–63 (2013).

25.	Abellan, P., Woehl, T. J., Parent, L. R., Browning, N. D., Evans, J. E. & Arslan, I. Factors influencing quantitative liquid (scanning) transmission electron microscopy. *Chem. Commun.* **50**, 4873–4880 (2014).

26.	Park, J., Park, H., Ercius, P., Pegoraro, A. F., Xu, C., Kim, J. W., Han, S. H. & Weitz, D. A. Direct observation of wet biological samples by graphene liquid cell transmission electron microscopy. *Nano Lett.* **15**, 4737–4744 (2015).

27.	Cameron Varano, A., Rahimi, A., Dukes, M. J., Poelzing, S., M. McDonald, S. & Kelly, D. F. Visualizing virus particle mobility in liquid at the nanoscale. *Chem. Commun.* **51**, 16176–16179 (2015).

28.	Pohlmann, E. S., Patel, K., Guo, S., Dukes, M. J., Sheng, Z. & Kelly, D. F. Real-time visualization of nanoparticles interacting with glioblastoma stem cells. *Nano Lett.* **15**, 2329–2335 (2015).

29.	Moser, T. H., Mehta, H., Park, C., Kelly, R. T., Shokuhfar, T. & Evans, J. E. The role of electron irradiation history in liquid cell transmission electron microscopy. *Sci. Adv.* **4**, eaaq1202 (2018).

30.	Keskin, S., Besztejan, S., Kassier, G., Manz, S., Bücker, R., Riekeberg, S., Trieu, H. K., Rentmeister, A. & Miller, R. J. D. Visualization of multimerization and self-assembly of DNA-functionalized gold nanoparticles using in-liquid transmission electron microscopy. *J. Phys. Chem. Lett.* **6**, 4487–4492 (2015).

31. Brintlinger, T., Love, C. & Baturina, O. Beam effects during in situ potential cycling and imaging of sulfuric acid and platinum electrodes. *Microsc. Microanal.* **21**, 1935–1936 (2015).

32. Park, J. H., Schneider, N. M., Grogan, J. M., Reuter, M. C., Bau, H. H., Kodambaka, S. & Ross, F. M. Control of electron beam-induced Au nanocrystal growth kinetics through solution chemistry. *Nano Lett.* **15**, 5314–5320 (2015).

33. Robertson, A. W., Zhu, G., Mehdi, B. L., Jacobs, R. M. J., De Yoreo, J. & Browning, N. D. Nanoparticle immobilization for controllable experiments in liquid-cell transmission electron microscopy. *ACS Appl. Mater. Interfaces* **10**, 22801–22808 (2018).

34. Wu, J., Gao, W., Wen, J., Miller, D. J., Lu, P., Zuo, J.-M. & Yang, H. Growth of Au on Pt icosahedral nanoparticles revealed by low-dose in situ TEM. *Nano Lett.* **15**, 2711–2715 (2015).

35. Jin, B., Sushko, M. L., Liu, Z., Jin, C. & Tang, R. In situ liquid cell TEM reveals bridge-induced contact and fusion of Au nanocrystals in aqueous solution. *Nano Lett.* **18**, 6551–6556 (2018).

36. Chen, Y.-C., Chen, J.-Y. & Wu, W.-W. In situ observation of Au nanostructure evolution in liquid cell TEM. *J. Phys. Chem. C* **121**, 26069–26075 (2017).

37. Anand, U., Lu, J., Loh, D., Aabdin, Z. & Mirsaidov, U. Hydration layer-mediated pairwise interaction of nanoparticles. *Nano Lett.* **16**, 786–790 (2016).

38. Batson, P. E., Reyes-Coronado, A., Barrera, R. G., Rivacoba, A., Echenique, P. M. & Aizpurua, J. Plasmonic nanobilliards: controlling nanoparticle movement using forces induced by swift electrons. *Nano Lett.* **11**, 3388–3393 (2011).

39. Batson, P. E., Reyes-Coronado, A., Barrera, R. G., Rivacoba, A., Echenique, P. M. & Aizpurua, J. Nanoparticle movement: Plasmonic forces and physical constraints. *Ultramicroscopy* **123**, 50–58 (2012).

40. Niu, Y., Schlexer, P., Sebok, B., Chorkendorff, I., Pacchioni, G. & Palmer, R. E. Reduced sintering of mass-selected Au clusters on SiO2 by alloying with Ti: an aberration-corrected STEM and computational study. *Nanoscale* **10**, 2363–2370 (2018).

41. Zheng, H., Mirsaidov, U. M., Wang, L.-W. & Matsudaira, P. Electron beam manipulation of nanoparticles. *Nano Lett.* **12**, 5644–5648 (2012).

42. Jiang, Y., Wang, Y., Zhang, Y. Y., Zhang, Z., Yuan, W., Sun, C., Wei, X., Brodsky, C. N., Tsung, C.-K., Li, J., Zhang, X., Mao, S. X., Zhang, S. & Zhang, Z. Direct observation of Pt nanocrystal coalescence induced by electron-excitation-enhanced van der Waals interactions. *Nano Res.* **7**, 308–314 (2014).

43. Kelly, D. J., Zhou, M., Clark, N., Hamer, M. J., Lewis, E. A., Rakowski, A. M., Haigh, S. J. & Gorbachev, R. V. Nanometer resolution elemental mapping in graphene-based TEM liquid cells. *Nano Lett.* **18**, 1168–1174 (2018).

44. Tan, S. F., Anand, U. & Mirsaidov, U. Interactions and attachment pathways between functionalized gold nanorods. *ACS Nano* **11**, 1633–1640 (2017).

45. Tan, S. F., Raj, S., Bisht, G., Annadata, H. V., Nijhuis, C. A., Král, P. & Mirsaidov, U. Nanoparticle interactions guided by shape-dependent hydrophobic forces. *Adv. Mater.* **30**, 1707077 (2018).

46. Lee, J., Nakouzi, E., Song, M., Wang, B., Chun, J. & Li, D. Mechanistic understanding of the growth kinetics and dynamics of nanoparticle superlattices by coupling interparticle forces from real-time measurements. *ACS Nano* **12**, 12778–12787 (2018).

47. Ahn, T.-Y., Hong, S.-P., Kim, S.-I. & Kim, Y.-W. In situ liquid-cell transmission electron microscopy for direct observation of concentration-dependent growth and dissolution of silver nanoparticles. *RSC Adv.* **5**, 82342–82345 (2015).

48. Lin, G., Chee, S. W., Raj, S., Král, P. & Mirsaidov, U. Linker-mediated self-assembly dynamics of charged nanoparticles. *ACS Nano* **10**, 7443–7450 (2016).

49. Niu, K.-Y., Liao, H.-G. & Zheng, H. Visualization of the coalescence of bismuth nanoparticles. *Microsc. Microanal.* **20**, 416–424 (2014).

50. Niu, K., Frolov, T., Xin, H. L., Wang, J., Asta, M. & Zheng, H. Bubble nucleation and migration in a lead–iron hydr(oxide) core–shell nanoparticle. *Proc. Natl. Acad. Sci. U.S.A.* **112**, 12928–12932 (2015).

51. Lin, G., Zhu, X., Anand, U., Liu, Q., Lu, J., Aabdin, Z., Su, H. & Mirsaidov, U. Nanodroplet-mediated assembly of platinum nanoparticle rings in solution. *Nano Lett.* **16**, 1092–1096 (2016).

52. Zheng, H., Smith, R. K., Jun, Y.-w., Kisielowski, C., Dahmen, U. & Alivisatos, A. P. Observation of single colloidal platinum nanocrystal growth trajectories. *Science* **324**, 1309–1312 (2009).

53. Lu, J., Aabdin, Z., Anand, U. & Mirsaidov, U. Effect of electron beam on nanoparticle dynamics in solution during in situ TEM observation. *Microsc. Microanal.* **21**, 257–258 (2015).

54. Aabdin, Z., Lu, J., Zhu, X., Anand, U., Loh, N. D., Su, H. & Mirsaidov, U. Bonding pathways of gold nanocrystals in solution. *Nano Lett.* **14**, 6639–6643 (2014).

55. Cueva, P., Hovden, R., Mundy, J. A., Xin, H. L. & Muller, D. A. Data processing for atomic resolution electron energy loss spectroscopy. *Microsc. Microanal.* **18**, 667–675 (2012).

56. Chee, S. W., Baraissov, Z., Loh, N. D., Matsudaira, P. T. & Mirsaidov, U. Desorption-mediated motion of nanoparticles at the liquid–solid interface. *J. Phys. Chem. C* **120**, 20462–20470 (2016).

57. Zhang, H.-R., Egerton, R. F. & Malac, M. Local thickness measurement through scattering contrast and electron energy-loss spectroscopy. *Micron* **43**, 8–15 (2012).

58. Frenkel, D. & Smit, B. *Understanding Molecular Simulation: from Algorithms to Applications* (Academic press, 2001).

59. Savage, J. R., Blair, D. W., Levine, A. J., Guyer, R. A. & Dinsmore, A. D. Imaging the sublimation dynamics of colloidal crystallites. *Science* **314**, 795–798 (2006).

60. Savage, J. R. & Dinsmore, A. D. Experimental evidence for two-step nucleation in colloidal crystallization. *Phys. Rev. Lett.* **102**, 198302 (2009).

61. ten Wolde, P. R., Ruiz-Montero, M. J. & Frenkel, D. Numerical calculation of the rate of crystal nucleation in a Lennard-Jones system at moderate undercooling. *J. Chem. Phys.* **104**, 9932–9947 (1996).

62. ten Wolde, P. R., Ruiz-Montero, M. J. & Frenkel, D. Simulation of homogeneous crystal nucleation close to coexistence. *Faraday Discuss.* **104**, 93–110 (1996).

63. Tan, P., Xu, N. & Xu, L. Visualizing kinetic pathways of homogeneous nucleation in colloidal crystallization. *Nat. Phys.* **10**, 73–79 (2013).

64. Tang, X., Rupp, B., Yang, Y., Edwards, T. D., Grover, M. A. & Bevan, M. A. Optimal feedback controlled assembly of perfect crystals. *ACS Nano* **10**, 6791–6798 (2016).

65. Lechner, W. & Dellago, C. Accurate determination of crystal structures based on averaged local bond order parameters. *J. Chem. Phys.* **129**, 114707 (2008).

66. Kawasaki, T. & Tanaka, H. Formation of a crystal nucleus from liquid. *Proc. Natl. Acad. Sci. U.S.A.* **107**, 14036–14041 (2010).

67. Ten Wolde, P. R. & Frenkel, D. Enhancement of protein crystal nucleation by critical density fluctuations. *Science* **277**, 1975–1978 (1997).

68. Zhang, T. H. & Liu, X. Y. How does a transient amorphous precursor template crystallization. *J. Am. Chem. Soc.* **129**, 13520–13526 (2007).

69. Erdemir, D., Lee, A. Y. & Myerson, A. S. Nucleation of crystals from solution: classical and two-step models. *Acc. Chem. Res.* **42**, 621–629 (2009).

70. Sauter, A., Roosen-Runge, F., Zhang, F., Lotze, G., Feoktystov, A., Jacobs, R. M. J. & Schreiber, F. On the question of two-step nucleation in protein crystallization. *Faraday Discuss.* **179**, 41–58 (2015).

71. Kashchiev, D. *Nucleation* (Butterworth-Heinemann, 2000).

72. Peng, Y., Wang, F., Wang, Z., Alsayed, A. M., Zhang, Z., Yodh, A. G. & Han, Y. Two-step nucleation mechanism in solid-solid phase transitions. *Nat. Mater.* **14**, 101–108 (2015).

73. Lutsko, J. F. & Nicolis, G. Theoretical evidence for a dense fluid precursor to crystallization. *Phys. Rev. Lett.* **96**, 046102 (2006).

74. Pan, W., Kolomeisky, A. B. & Vekilov, P. G. Nucleation of ordered solid phases of proteins via a disordered high-density state: phenomenological approach. *J. Chem. Phys.* **122**, 174905 (2005).

75. Chung, S., Shin, S.-H., Bertozzi, C. R. & De Yoreo, J. J. Self-catalyzed growth of S layers via an amorphous-to-crystalline transition limited by folding kinetics. *Proc. Natl. Acad. Sci. U.S.A.* **107**, 16536–16541 (2010).

76. Vivares, D., Kaler, E. W. & Lenhoff, A. M. Quantitative imaging by confocal scanning fluorescence microscopy of protein crystallization via liquid-liquid phase separation. *Acta Crystallogr.* **61**, 819–825 (2005).

77. Poon, W. C. K., Renth, F., Evans, R. M. L., Fairhurst, D. J., Cates, M. E. & Pusey, P. N. Colloid-polymer mixtures at triple coexistence: kinetic maps from free-energy landscapes. *Phys. Rev. Lett.* **83**, 1239–1242 (1999).

78. Schope, H. J., Bryant, G. & van Megen, W. Two-step crystallization kinetics in colloidal hard-sphere systems. *Phys. Rev. Lett.* **96**, 175701 (2006).

79. Schilling, T., Schope, H. J., Oettel, M., Opletal, G. & Snook, I. Precursor-mediated crystallization process in suspensions of hard spheres. *Phys. Rev. Lett.* **105**, 025701 (2010).

80. Toth, G. I., Pusztai, T., Tegze, G., Toth, G. & Granasy, L. Amorphous nucleation precursor in highly nonequilibrium fluids. *Phys. Rev. Lett.* **107**, 175702 (2011).

81. Anderson, V. J. & Lekkerkerker, H. N. W. Insights into phase transition kinetics from colloid science. *Nature* **416**, 811–815 (2002).

82. Auer, S. & Frenkel, D. Prediction of absolute crystal-nucleation rate in hard-sphere colloids. *Nature* **409**, 1020–1023 (2001).
83. Parsegian, V. A. *Van der Waals Forces: a Handbook for Biologists, Chemists, Engineers, and Physicists* (Cambridge University Press, 2005).
84. Batista, C. A., Larson, R. G. & Kotov, N. A. Nonadditivity of nanoparticle interactions. *Science* **350**, 1242477 (2015).
85. Lee, A. A., Perez-Martinez, C. S., Smith, A. M. & Perkin, S. Scaling analysis of the screening length in concentrated electrolytes. *Phys. Rev. Lett.* **119**, 026002 (2017).
86. Li, Y., Girard, M., Shen, M., Millan, J. A. & Olvera de la Cruz, M. Strong attractions and repulsions mediated by monovalent salts. *Proc. Natl. Acad. Sci. U.S.A.* **114**, 11838–11843 (2017).
87. Mbamala, E. C. & von Grünberg, H. H. Charged colloids and proteins at an air-water interface: The effect of dielectric substrates on interaction and phase behavior. *Phys. Rev. E* **67**, 031608 (2003).
88. Möller, T. & Trumbore, B. Fast, minimum storage ray-triangle intersection. *J. Graphics Tools* **2**, 21–28 (1997).
89. Donev, A., Burton, J., Stillinger, F. H. & Torquato, S. Tetratic order in the phase behavior of a hard-rectangle system. *Phys. Rev. B* **73**, 054109 (2006).
90. Agarwal, U. & Escobedo, F. A. Mesophase behaviour of polyhedral particles. *Nat. Mater.* **10**, 230–235 (2011).
91. Damasceno, P. F., Engel, M. & Glotzer, S. C. Predictive self-assembly of polyhedra into complex structures. *Science* **337**, 453–457 (2012).
92. Young, K. L., Jones, M. R., Zhang, J., Macfarlane, R. J., Esquivel-Sirvent, R., Nap, R. J., Wu, J., Schatz, G. C., Lee, B. & Mirkin, C. A. Assembly of reconfigurable one-dimensional colloidal superlattices due to a synergy of fundamental nanoscale forces. *Proc. Natl. Acad. Sci. U.S.A.* **109**, 2240–2245 (2012).
93. Eppenga, R. & Frenkel, D. Monte Carlo study of the isotropic and nematic phases of infinitely thin hard platelets. *Mol. Phys.* **52**, 1303–1334 (1984).